



Master Thesis in  
Mechatronic Engineering  
Department of Automation and Informatics  
Polytechnic of Turin  
05/26/2024

## **Monte Carlo sensitivity analysis of the neutron spectrum on the magnets of a compact fusion reactor**

by

Matteo Di Giacomo



**MIT Supervisor:**  
Michael P. Short

**PSFC Supervisor:**  
Zachary Hartwig

**Polytechnic of Turin Supervisors:**  
Francesco Laviano, Massimo Zucchetti

## Abstract

As humanity embarks on a quest for sustainable energy solutions, nuclear fusion is gaining momentum, emerging as a beacon of hope and offering transformative solutions to pressing environmental challenges and concerns. This work provides an overview of the fundamentals of nuclear fusion, its historical development, and the current state of research. Furthermore, it focuses on one of the critical aspects of fusion energy development: material selection. The success of fusion as a viable energy source hinges on the development of materials capable of withstanding the extreme conditions within a fusion reactor, including high temperatures, intense radiation, corrosive environments and mechanical loads. Particular attention has been devoted to one of the most critical and expensive components of the reactor, namely the superconducting magnets. More precisely this work delves on the toroidal field shield optimization. Variation of the Tritium breeding ratio (TBR) when different materials are used as shielding of the Toroidal Field Coil (TFC) in an ARC like fusion reactor has been confirmed resulting in a reduction of the TBR when neutron flux increases on the high temperature superconductors (HTS).  $TiH_2$ , for some reactor design configurations, and tungsten carbide exhibit superior shielding properties compared to the actual baseline material  $ZrH_2$ . Furthermore FLiPb has been investigated as coolant and blanket materials leading to a significant reduction of the capital cost of the reactor compared to FLiBe. Finally activation analysis on different vacuum vessel materials (V4Cr4Ti, F82H, and SiC) have been performed, including shutdown dose rate (SDR) based on the Rigorous 2-Step (R2S) approach for the chromium vanadium alloy. To this purpose have been evaluated integral fluxes, neutron and PKA spectra, dpa, specific activities, dose rates and TBR for different ARC design reactor configurations.

# Contents

<b>Introduction</b>	<b>3</b>
Fusion and world energy . . . . .	3
Key aspects of nuclear fusion . . . . .	3
Neutron capture and tritium breeding . . . . .	5
Superconducting magnets and shielding optimization . . . . .	6
Engineering facing plasma components . . . . .	7
Materials activation and shutdown dose rate . . . . .	7
<b>Method</b>	<b>8</b>
Design reactor parameter . . . . .	8
Monte Carlo simulation . . . . .	11
Split or Russian roulette . . . . .	12
Shutdown . . . . .	13
<b>Results</b>	<b>15</b>
TBR . . . . .	15
Integral neutron flux . . . . .	19
Neutron spectra . . . . .	25
PKA spectra & DPA . . . . .	30
Activity and dose rate . . . . .	33
<b>Conclusion</b>	<b>43</b>
<b>Appendix A</b>	<b>48</b>
ICRP74 conversion coefficient . . . . .	48
<b>Appendix B</b>	<b>49</b>
W 0.5 - V4Cr4Ti 5 - FLiBe90 2 - Be 1 - V4Cr4Ti 5 . . . . .	49
W 0.5 - V4Cr4Ti 5 - FLiBe 2 - Be 1 - V4Cr4Ti 5 . . . . .	56
W 0.5 - V4Cr4Ti 2 - FLiBe90 2 - Be 1 - V4Cr4Ti 2 . . . . .	63
W 0.5 - V4Cr4Ti 2 - FLiBe 2 - Be 1 - V4Cr4Ti 2 . . . . .	70

# Introduction

## Fusion and world energy

The global energy portfolio is a complex and dynamic system, reflecting the diverse array of technologies and resources available to meet the world's energy demands. As we navigate through the 21st century, the energy landscape is characterized by a dominant reliance on fossil fuels, a growing contribution from renewable energy sources, and the potential of nuclear power, including the promise of nuclear fusion, to play a significant role in the transition to a more sustainable energy future.

Fossil fuels, comprising coal, oil, and natural gas, have historically been the cornerstone of global energy supply, powering industries, transportation, and households. Despite the increasing awareness of climate change and environmental degradation, fossil fuels are projected to remain a major source of energy until the end of the century, with natural gas expected to grow in importance as oil resources deplete [48]. However, the environmental impact of large-scale fossil fuel production cannot be overlooked, as it poses significant challenges to the planet's heat balance and ecosystem integrity [48].

Renewable energy sources, primarily hydro, wind, and solar, are rapidly expanding their share in the global energy mix. In 2020, renewables accounted for 12.6% of total energy consumption, with nuclear energy contributing 6.3% [25]. The transition from fossil fuels to renewables is a monumental task that requires a multifaceted approach, including the development of renewable energy technologies, improvements in energy efficiency, and the implementation of policies such as carbon taxes and cap and trade systems [25]. Achieving a zero fossil fuel scenario by 2050 may be possible but demands aggressive application of these strategies, alongside significant lifestyle changes, particularly in developed countries [25]. Nuclear energy, both through fission and the potential of fusion, is seen as a sustainable option that can deliver large quantities of energy required by modern societies. Nuclear fission is already a developed technology capable of reducing greenhouse gas emissions significantly when replacing fossil fuel-based electricity generation [9]. Nuclear fusion represents a process with the potential to significantly alter the global energy landscape, offering a cleaner and abundant source of power. The integration of nuclear with renewable sources can create combined-energy systems that offer solutions to intermittency and enhance the sustainability of the energy supply [54].

## Key aspects of nuclear fusion

Nuclear fusion is a nuclear reaction which aims to overcome the repulsive electrostatic force that keeps two nuclei separated from each other to form one or more new nuclei and subatomic particles. The necessity of relate to light elements rise because the object is to produce energy, which is released only up to  $^{56}\text{Fe}$  and  $^{62}\text{Ni}$  [40]. Between different fusion reactions the easiest to initiate is the D-T reaction. Moreover it release a significant amount of energy as it can be seen from Eq. (1).

$$D + T \rightarrow_2^4 \text{He} + n \quad (17.6 \text{ MeV}) \quad (1)$$

Several configurations of reactors have been explored to generate the plasma and initiate such reactions. The first ignited plasma ever achieved was reported by the National Ignition Facility [5]. This is an inertial confinement fusion (ICF) configuration. ICF is a method of achieving nuclear fusion by using the inertia of a fuel mass to confine it long enough for fusion to occur. The process involves compressing a fuel capsule, typically a spherical shell containing a mixture of deuterium and tritium, to extremely high densities and temperatures. This compression is achieved through an implosion, which can be driven by either direct or indirect means.

In the direct-drive approach, laser or charged particle beams are aimed directly at the target capsule. The energy from these beams is absorbed by the capsule's outer layers, causing it to heat up and implode. The primary absorption mechanism for the laser energy is inverse bremsstrahlung, where the laser energy is transferred to the electrons in the plasma [36].

Another approach is the Z-pinch method, which utilizes the principle of magnetic compression, where an axial current induces a magnetic field that compresses a plasma to conditions suitable for fusion [22] [18] [46]. The Z-pinch has been considered for various applications, including in the context of inertial confinement fusion, with designs aiming to achieve high yields and symmetric capsule implosions [29] [21].

Other possible configuration is the stellarator, which rely on a complex arrangement of magnetic coils to confine the hot plasma without the need for a large plasma current, which can introduce stability issues

## Fusion Reaction

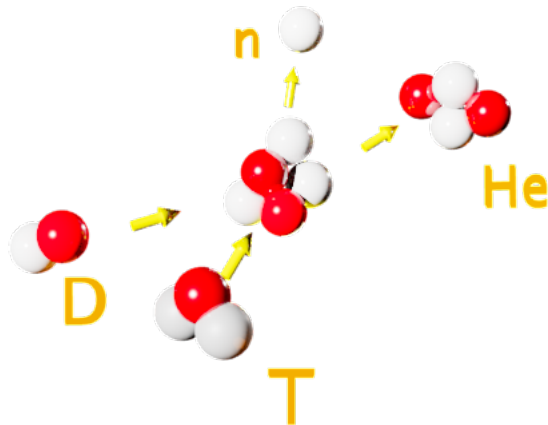


Figure 1: D-T fusion reaction; energy released 17.6MeV

and complicate sustained operation [1]. The optimization of stellarator configurations has been a key focus, with the development of advanced stellarators that feature optimized coil systems and improved plasma equilibrium [16]. Furthermore, the stellarator concept has been explored for its potential in hybrid systems [47].

While ICF, stellarators, and other configurations such as pinches and mirrors have their own set of challenges, they are not directly comparable to tokamaks in terms of maturity of the technology. The tokamak's journey began in the late 1960s when it first gained recognition as a promising approach to achieve controlled thermonuclear fusion [7]. These devices have been designed to confine hot plasma using magnetic fields in a toroidal shape, with the ultimate goal of achieving conditions necessary for fusion reactions to occur [4]. The development of tokamaks has been marked by significant advancements in understanding the physics of plasma confinement. Research has delved into the operational domain of current, density, and pressure, as well as the phenomena associated with plasma activity and relaxation [4]. Between different kind of tokamaks, it is worth mentioning the International Thermonuclear Experimental Reactor (ITER) and the Affordable, Robust, Compact (ARC) reactor. Both aim to achieve controlled nuclear fusion, but they differ in design, size, and technological approaches. In particular the ARC reactor is designed to be more compact and it utilizes high-field, high-temperature superconducting magnets to achieve an on-axis magnetic field higher than ITER's magnetic field [8]. ITER is a public project, and it pursuit the larger goal of advancing the frontiers of human knowledge and supporting education in addition to solving the specific challenges of fusion power [6]. The research performed in the public sector over the past 70 years has brought fusion energy science and technology to the point where near-term commercialization is possible [6]. This explains the rise in number of fusion companies deployment over the preceding decades; as a consequence of the inherent benefits of fusion energy, combined with the continual progression of scientific discoveries and technological breakthroughs [50]. Indeed, one of the primary obstacles in integrating tokamaks into the power grid as commercially viable devices was the effective magnetic confinement of plasma. Leveraging HTS facilitates the attainment of elevated magnetic field strengths. Given that power output scales proportionally to the fourth power of the magnetic field strength, this advancement enables the scaling of fusion devices into more compact configurations, thereby enhancing cost-effectiveness. After MIT proposal and demonstration of HTS applicability, superconducting magnets have been recently tested, experimentally demonstrating a large-scale high-field rare earth barium copper oxide (REBCO) magnet, achieving 20.1 T peak field-on-conductor with 40.5 kA of terminal current, 815 kN/m of Lorentz loading on the REBCO stacks, and

almost 1 GPa of mechanical stress accommodated by the structural case [50]. Nevertheless the pursuit of fusion energy is encumbered by a multitude of formidable technological challenges. These challenges, excluding magnetohydrodynamics (MHD), delineates a specific framework, which can be summarized as follow:

- Neutron capture and tritium generation
- Magnet protection
- Engineering facing plasma component
- Shutdown dose and activation related issues

As already mentioned the main focus during the introduction section will be devoted to the material selections for fusion reactor application. A brief explanation of the critical aspect is then required. Figure 2 shows the limits on the use of elements inside a fusion reactor. Despite the abundance of possible combinations to form many different compounds, stringent requirement must be fulfill as it is better explained in the following subsections.

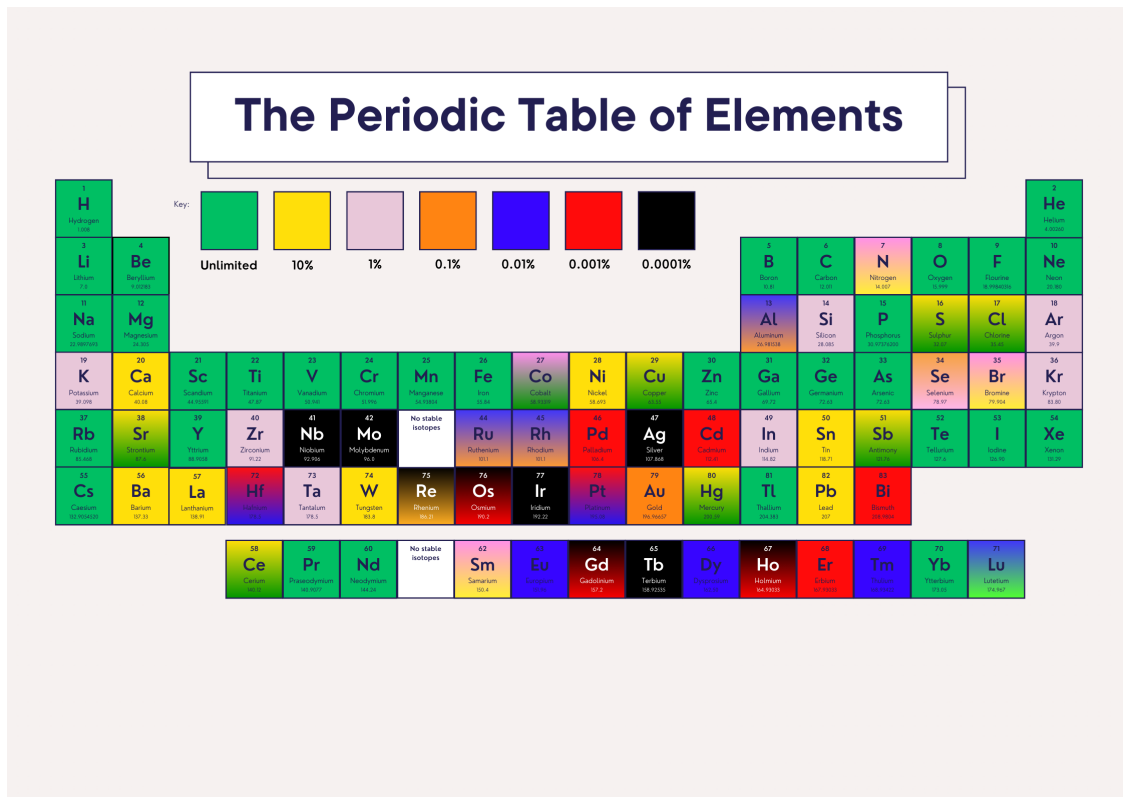


Figure 2: Periodic table showing the limits on the use of elements for near-surface burial after US methodology [15].

## Neutron capture and tritium breeding

Tritium, a radioactive isotope of hydrogen, plays a pivotal role in the field of nuclear fusion, particularly as a fuel for future fusion power plants. In those reactors, tritium is bred in a blanket module that surrounds the fusion plasma, due to the presence of lithium. The design of these breeder blankets is crucial, as it must facilitate the production and recovery of tritium while ensuring safety and environmental protection.

Research in tritium handling and containment is extensive, addressing the radiochemical characteristics of tritium and its behavior in various reactor components. This includes the development of technologies for tritium fueling, recycling, breeding, recovery, and storage, as well as systems to prevent hazards such as hydrogen explosions and corrosion due to tritiated water [38] [41] [37]. Tritium's beta radiation

and gaseous state pose unique challenges, as it can easily leak and contaminate surroundings, necessitating stringent containment and control measures [13] [38]. The integration of these technologies into a closed tritium cycle is essential for the operational success and environmental safety of fusion reactors. Another important parameter is the Tritium Breeding Ratio (TBR). In a fusion reactor the TBR is a critical parameter that measures the efficiency of a tritium breeding blanket in producing tritium. The TBR indicates whether a breeding blanket can generate enough tritium to sustain the reactor's operation, aiming for tritium self-sufficiency, which is achieved when the TBR is greater than 1 [43]. Tritium is not naturally abundant and must be bred within the reactor itself from lithium through neutron capture processes. The TBR is defined as the ratio of the number of tritium atoms produced to the number of tritium atoms consumed in the fusion reactions. A TBR greater than 1 means that the reactor produces more tritium than it consumes, which is essential for continuous operation without the need for external tritium sources [49]. The importance of TBR lies in its impact on the reactor's viability and sustainability. A higher TBR can lead to improved reactor autonomy and reduced reliance on external tritium supplies, which are expensive and limited. Moreover, achieving a high TBR is necessary to compensate for tritium losses in the fuel cycle and to ensure a sufficient supply for continuous reactor operation [49]. Research has shown that the TBR is influenced by various factors, including the materials used in the breeding blanket, the geometry of the reactor, and the accuracy of neutronic calculations [24]. Carefully designing materials and sizing of the reactor components is crucial to achieve a sufficient TBR for self-sustainability of fusion reactor power plant.

Inside the blanket those issues involves the safety of the power plant in terms of toxicity, reactivity and radioactivity of the materials. Furthermore the materials must be classified as low activation, which means that they must satisfy characteristics such as waste management, accident safety, maintenance and routine effluents [15].

## Superconducting magnets and shielding optimization

Superconductivity, the phenomenon where a material exhibits zero electrical resistance and expels magnetic fields, was first discovered by Heike Kamerlingh Onnes in 1911 during its experiments which had led, among the other thing, to the preparation of liquid helium. This remarkable state of matter has since captivated scientists due to its potential applications and the fundamental questions it raises about the nature of materials.

"As has been said, the experiment left no doubt that, as far as accuracy of measurement went, the resistance disappeared. At the same time, however, something unexpected occurred. The disappearance did not take place gradually but abruptly. From 1/500 the resistance at 4.2 K drops to a millionth part. At the lowest temperature, 1.5 K, it could be established that the resistance had become less than a thousand-millionth part of that at normal temperature.

Thus the mercury at 4.2 K has entered a new state, which, owing to its particular electrical properties, can be called the state of superconductivity... There is also the question as to whether the absence of Joule heat makes feasible the production of strong magnetic fields using coils without iron [61]"

- Heike Kamerlingh Onnes, Nobel Lecture 11 December 1913

It was clear to Onnes that superconductivity has an intrinsically enormous potential on magnet applications, due to its physical properties. Nevertheless a deeper understanding of the physics of this phenomenon was required as well as the discoveries of materials which present favorable properties for practical applications. The foundational theory of superconductivity was developed by Bardeen, Cooper, and Schrieffer in 1957, known as the BCS theory. This microscopic theory explains that superconductivity arises from the formation of Cooper pairs, where electrons pair up via an attractive interaction mediated by lattice vibrations or phonons [52]. This interaction leads to a phase transition at a critical temperature below which the material becomes superconducting. Another important influential theoretical frameworks for understanding superconductivity is the Ginzburg-Landau (GL) theory, developed by Vitaly Ginzburg and Lev Landau in 1950. The GL theory provides a macroscopic description of superconductivity, focusing on the behavior of the superconducting order parameter, which describes the density of the Cooper pairs. The Ginzburg-Landau theory is phenomenological, meaning it is based on empirical observations rather than derived from first principles. It introduces a complex order parameter whose magnitude represents the density of superconducting pairs, and whose phase is related to the quantum mechanical wave function of these pairs. The theory is encapsulated in the Ginzburg-Landau free energy functional, which describes the free energy of a superconductor

as a function of the order parameter and the magnetic field. This functional can be minimized to derive the Ginzburg-Landau equations, which govern the spatial variation of the order parameter and the magnetic field in a superconductor. The study of superconductivity is not limited to understanding its fundamental mechanisms. It also encompasses the exploration of its magnetic and thermal properties. For instance, the Meissner effect, where a superconductor expels magnetic fields, is a critical characteristic that distinguishes it from a perfect conductor [59]. The GL theory has been particularly successful in describing type II superconductors, which allow magnetic fields to partially penetrate through quantized vortices. These vortices form a lattice structure and are a key feature distinguishing type II from type I superconductors, which completely expel magnetic fields (the Meissner effect). The theory also provides insights into the thermodynamic properties of superconductors and the nature of the phase transition between the normal and superconducting states. Moreover, the Ginzburg-Landau theory has been extended to include time-dependent phenomena, leading to the time-dependent Ginzburg-Landau (TDGL) equations. These equations are crucial for understanding dynamic processes in superconductors, such as the response to time-varying magnetic fields and the behavior of superconducting vortices under non-equilibrium conditions [58].

The journey of superconducting materials began with elemental superconductors, but significant advancements were made with the discovery of Type II superconductors, which can withstand high magnetic fields. Among these, niobium-based alloys such as Nb-Ti ( $T_c = 9$  K) and Nb<sub>3</sub>Sn ( $T_c = 18$  K) have been the cornerstone for superconducting magnets used in particle accelerators, magnetic resonance imaging (MRI), and nuclear magnetic resonance (NMR) systems [62]. Nevertheless, the discovery of high-temperature superconductors marked a pivotal moment in the history of these materials, signifying their status as some of the most intriguing and actively researched substances in contemporary materials science. For instance the 1987 March Meeting of the American Physical Society (APS), held in New York City, is legendary in the field of physics due to the presentation of breakthrough discoveries in high-temperature superconductivity, specifically the presentation of research on yttrium barium copper oxide (YBCO), a material that became a significant milestone in superconductivity research. Prior to this conference, in 1986, Alex Müller and Georg Bednorz discovered a new class of superconducting materials known as cuprates, which exhibited superconductivity at temperatures higher than previously thought possible, around 30 Kelvin [60]. During the conference, the most significant and eagerly anticipated presentations were about YBCO, a compound that displayed superconductivity at around 92 Kelvin, which can be achieved using liquid nitrogen (boiling point 77 K), a much more practical and less expensive coolant than liquid helium. This congress is remembered as the "Woodstock of Physics", coined because the enthusiasm and the number of people drawn to the event were reminiscent of the famous 1969 Woodstock music festival [57].

## **Engineering facing plasma components**

### **Materials activation and shutdown dose rate**

## Method

### Design reactor parameter

In order to compute the TBR Monte Carlo (MC) simulations have been performed on a section of 20 degrees of the reactors with reflective boundary conditions imposed on the sides of the slice. This reduced computational time while keeping a full unit representative 3D CAD geometry. Figure 3 shows the geometry made in Solidworks and meshed with Altair Simlab before the importation on the Particle and Heavy Ions Transport code System (PHITS), software used in this work for the Monte Carlo simulations.

The provided study outlines, as a starting point, two distinct geometries (called A and B), both with 36 different domains. Each HTS TF coil was subdivided in 4 different regions in order to evaluate the radiation damage in the most critical one. The main characteristics of the components are listed in Table 1. The two configurations of the geometries differ on the thickness of the Vacuum Vessel resulting in

Main geometry features		
Parameters	CAD A	CAD B
Shielding thickness for outboard superconducting PF coils	25 cm	25 cm
Outboard superconducting PF coil casing thickness	1 cm	1 cm
Size of gap between outboard PF shielding and blanket tank	1 cm	1 cm
Inboard superconducting PF coil casing thickness	1 cm	1 cm
Shielding thickness for outboard superconducting PF coils	25 cm	25 cm
Size of gap between inboard PF shielding and blanket tank	1 cm	1 cm
TF shield to tank gap	3 cm	3 cm
Thickness of inboard TF shielding	51 cm	51 cm
TF shield TF to gap	1 cm	1 cm
Outer vacuum vessel thickness	5 cm	2 cm
Beryllium layer thickness	1 cm	1 cm
FLiBe channel thickness	2 cm	2 cm
Inner vacuum vessel thickness	5 cm	2 cm
First wall (FW) armature	0.5 cm	0.5 cm

Table 1: Increasing the vacuum vessel thickness results in a reduction of the Blanket size

a reduction of the volume of the Blanket from  $17.656 \text{ m}^3$  to  $18.873 \text{ m}^3$  for CAD A and B, respectively. Particular attention in this work is on the material choice of the TFC shield. For this reason the materials have been kept fixed, with the exception of the TF shielding material. Furthermore for the thicker vacuum vessel case (CAD A) FLiPb was also used as salt coolant channel and blanket for some of the TF shielding configurations. FLiPb chemical composition is made of 40% LiF and 60% PbF<sub>2</sub>. Different solutions have been analyzed as illustrated in Table 2 taking into account the state of the art [42].

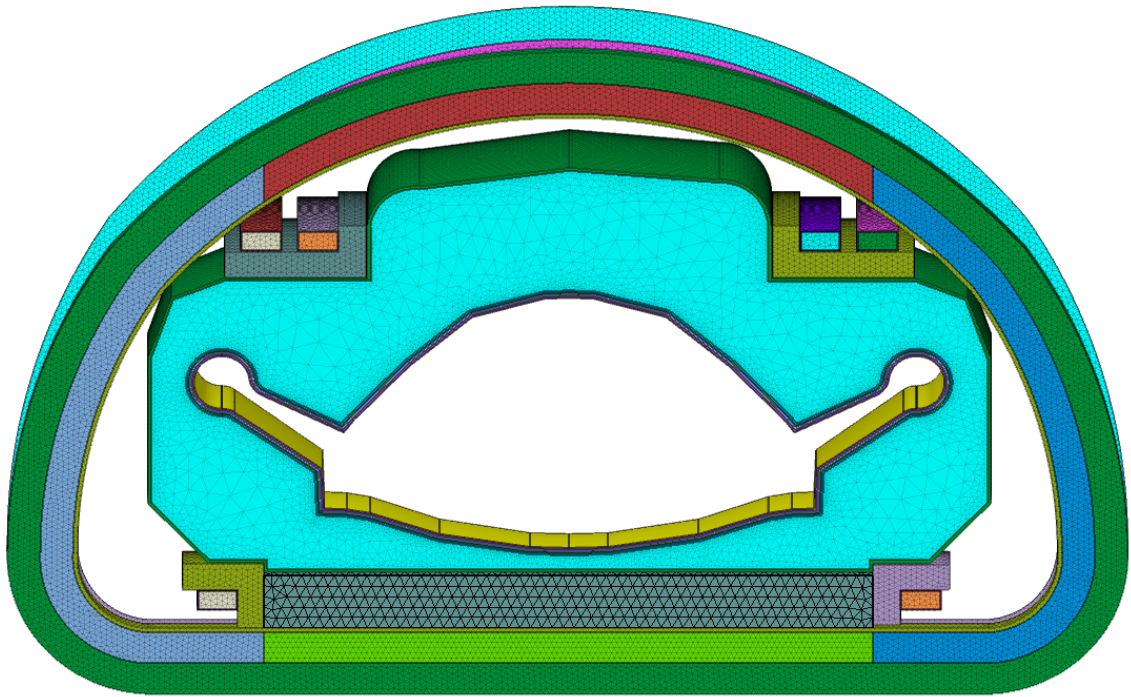


Figure 3: Geometry CAD B meshed through Altair Simlab.

TF Shields		
Material	Density [ $\frac{g}{cm^3}$ ]	Reference
TiH <sub>2</sub>	3.75	[53]
ZrH <sub>2</sub>	5.6	[53]
GdH <sub>2</sub>	7.08	[17]
GdH <sub>3</sub>	6.57	[17]
HfH <sub>2</sub>	11.4	[56]
HfV <sub>2</sub>	9.51	[28]
VB	5.54	[65]
WB	15.3	[64]
WB4	8.23	[10]
B4C	2.51	[10]
WC	15.32	[10]
SS316L	8	[53]
void	0	-

Table 2: TF shielding materials and densities

ARC reactor materials and densities			
Component	Material	Density [ $\frac{g}{cm^3}$ ]	Reference
First wall	W	19.3	[53]
Inner vacuum vessel	V4Cr4Ti	6.05	[20]
Salt coolant channel	FLiBe/FLiPb*	1.94/3.5	[44]/[35]
Neutron multiplier	Be	1.848	[53]
Outer vacuum vessel	V4Cr4Ti	6.05	[20]
Blanket	FLiBe/FLiPb*	1.94/3.5	[44]/[35]
Blanket tank	V4Cr4Ti	6.05	[20]
PF shield	ZrH <sub>2</sub>	5.6	[53]
PF casing	SS316L	8	[53]
PF	YBCO	6.4	[3]
TF casing	SS316L	8	[53]
TF	YBCO	6.4	[3]

Table 3: \*The enrichment of <sup>6</sup>Li in FLiBe (density 1.94 g/cc) has been investigated in its natural composition (7.5%) and for high enrichment configurations (90%). In the case of FLiPb (density 3.5 g/cc) has been set 90% enrichment of <sup>6</sup>Li [35].

Although it is well known that Gd and Hf have large cross sections for thermal neutron capture, hydrogen in these hydrides moderates fast neutrons to thermal neutrons so that the heavier elements can absorb neutrons efficiently [30]. Similar consideration can be drawn for Ti and Zr. Other evaluations have to be made for WB and VB since boron have high cross section for neutron absorption at lower energy [10]. Tungsten should be considered for applications on high temperature environment. In fact tungsten has high density, fast neutron removal and absorption cross sections. The primary restrictions on the use of tungsten are high cost, difficulty in fabrication and the limitation of availability in large size [31]. Tungsten Carbide is of particular interest since the presence of carbon nuclei contributes to the moderation of fast neutron flux, reducing the contribution to the total dose rate [31]. Contrarily, SS316L, and naturally, the scenario wherein the shielding region is void-filled, do not exhibit comparable shielding capabilities and together with HfV<sub>2</sub> are utilized for comparison purposes.

Table 3 summarize the additional materials utilized in the remaining components of the reactor. The design reactor parameters and materials have been chosen accordingly with the results and study made on other works [23] [27] [24]. Materials densities and chemical compositions have been selected according with the Compendium of Material Composition Data for Radiation Transport Modeling [53]. Materials not cataloged in the mentioned database can be find in references. In particular for the evaluation of activation of the structural components the chemical compositions of the vacuum vessel materials have been taken from [24] for F82H and for SiC fiber Sylaric<sup>TM</sup> has been choose [32].

## Monte Carlo simulation

Monte Carlo software is a computational tool used to perform Monte Carlo simulations, which are a class of algorithms that rely on repeated random sampling to obtain numerical results. The primary purpose of these simulations is to model complex systems and processes that are analytically intractable. Monte Carlo methods are widely used in various fields such as physics, finance, engineering, and radiation transport. Monte Carlo simulations have become an indispensable tool in the field of nuclear applications due to their ability to model complex physical processes with high accuracy. These simulations rely on statistical methods to solve physical and mathematical problems by simulating the random behavior of particles.

The versatility and precision of Monte Carlo methods make them particularly valuable in various nuclear applications, including nuclear medicine, reactor physics, and radiation protection. In nuclear medicine, Monte Carlo simulations are extensively used to enhance imaging techniques such as Single Photon Emission Computed Tomography (SPECT) and Positron Emission Tomography (PET). These simulations help in the design and optimization of imaging systems, improving image quality, and developing new correction techniques for scatter and attenuation [55] [67]. For instance, Monte Carlo methods have been applied to simulate the behavior of gamma cameras and to study the effects of different physical parameters on image quality [55]. In fact the ability to model complex interactions of photons and electrons with matter allows for the development of more accurate and efficient imaging protocols [67].

In the realm of nuclear reactor physics, Monte Carlo simulations are used to perform high-fidelity calculations of neutron transport and reactor kinetics. These simulations provide detailed insights into the behavior of neutrons within a reactor, which is crucial for safety assessments and reactor design.

The Dynamic Monte Carlo method, for example, solves coupled Boltzmann and kinetic equations with exact geometry and continuous energy, offering a more precise analysis of transient phenomena in reactors [63]. This method addresses the limitations of traditional deterministic approaches by reducing approximations and providing more accurate results [63].

Monte Carlo methods are also employed in radiation protection and dosimetry to evaluate the exposure and dose distribution in various scenarios. These simulations help in designing protective measures and optimizing radiation therapy treatments. The ability to simulate complex geometries and interactions makes Monte Carlo methods ideal for assessing radiation exposure in medical and industrial settings [51]. Furthermore, advancements in computational power and the development of sophisticated Monte Carlo codes have expanded the applicability of these simulations. Programs such as SuperMC have been developed to integrate Monte Carlo methods with other computational techniques, enhancing their capability to simulate multi-physical phenomena in nuclear systems [66]. These tools are continuously evolving, incorporating new data and improving their accuracy and efficiency [66].

In summary, Monte Carlo simulations play a critical role in advancing nuclear applications by providing detailed and accurate models of particle interactions. Their use in nuclear medicine, reactor physics, and radiation protection highlights their versatility and importance in the field. As computational technologies continue to evolve, the scope and precision of Monte Carlo simulations are expected to further expand, driving innovations and improvements in nuclear science and engineering.

As already explained Monte Carlo method involves generating random numbers to simulate the behavior of particles or other entities within a system. These random samples are used to estimate the properties of the system, such as particle flux, energy deposition, or radiative transfer through the tallies. A tally is a mechanism to record the occurrences of specific events or the accumulation of certain quantities during the simulation. Different types of tallies are used depending on the goal of the simulation. For instance a flux tally measures the particle flux within a specified region or cell. In this tally, the track length is evaluated whenever particles pass through a specified region, and the sum of the track lengths in units of [cm] is scored. Based on this, taking as example the software PHITS, a particle fluence in units of [ $\text{cm}^{-2}\text{source}^{-1}$ ] is determined by dividing the scored track lengths by the volume of the region and the number of source particles. In this work the number of source particles (or emissivity) has been computed as in [23]:

$$\dot{F} = \frac{\text{Power}}{E_{D-T}} \quad (2)$$

In this case the power of the reactor is 525 MW, but since only 20 degrees are simulated it must be scaled by a factor of 20/360.  $E_{D-T}$  is the energy released by the deuterium tritium reaction. For those reasons, in this case the number of neutrons emitted per seconds is:

$$\dot{F} = \frac{525[\text{MW}] \cdot \frac{20}{360}}{17.59[\text{MeV}] \cdot 1.60218 \cdot 10^{-19}[\text{MJ/MeV}]} = 1.0349 \cdot 10^{19} \text{neutron} \cdot \text{s}^{-1} \quad (3)$$

The number of particles simulated within the simulation instead may vary depending on the tally. To evaluate the Tritium Breeding Ratio (TBR), simulations involving 4.75E+07 particles were conducted. This particle count ensures low relative errors and provides sufficient statistical significance for accurately simulating the TBR within both the salt coolant channel and blanket regions. However, a distinct approach is necessary for simulations including a more complex geometry. The presence of shielding and the greater distance from the source necessitate simulations with an higher number of particles. Due to the computational time scaling with the number of particles (N) and standard errors scaling inversely with the square root of N, computational demands become substantial. Consequently, Variance Reduction (VR) techniques are employed to compute the neutron fluxes to mitigate computational time while maintaining accuracy. While a comprehensive explanation of VR techniques is beyond the scope of this work, a brief review is included here.

## Split or Russian roulette

In Monte Carlo simulations VR are widely used in case of complex geometry especially in the presence of shielding. Different approaches exist to implement it and in particular the method used in this work is called "*weight window*". Basically the weight represent the importance of each particle that is always equal to 1 in normal Monte Carlo simulations. Whereas thanks to the weight window method it is possible to assign allowed weight range (window) to each cell and to each energy group. E.g. in the case of track length tally:

$$\frac{\sum_{i=1}^N L_i W_i}{n_0} \quad (4)$$

where

- $L_i$ : track length of i-th particle
- $W_i$ : weight of i-th particle
- $n_0$ : total history number

Changing opportunely the weight of the particle it is possible to artificially increase the probability of rare event occurrences allowing particles to focus on the desired energies in the regions of interest. Particles between the fixed energy range will not undergo any splitting or Russian roulette. On the contrary particles over the maximum allowed energy will split while below the minimum desired energy will face a Russian roulette based on the weight imposed in that specific region. [45]

## Shutdown

The SDR was computed due to the recent development of Phits. In fact a new function was implemented which enable the activation analysis coupling PHITS with DCHAIN. The automatization is described as follow:

- Through a Monte Carlo simulation the neutron energy spectra below 20 MeV with a 1968 energy group structure is evaluated.
- Within the same simulation nuclear production yields by protons, heavy-ions, mesons, and neutrons with energies above 20 MeV are computed. The neutron energy spectra are multiplied by the activation cross section contained in the DCHAIN data library.
- The total activations are then estimated by adding these results and those directly calculated by PHITS.
- Subsequently, DCHAIN evaluates radioactivity, nuclide, decay heat, and the gamma energy spectrum at irradiation and cooling time.

One of the main feature regards the data libraries; hybrid data libraries have been implemented composed in the order selected by the user. Moreover DCHAIN compute the gamma dose rate for each nuclide as:

$$\text{Dose rate } [\mu\text{Sv m}^6/\text{hr}] = \text{radioactivity } [\text{MBq/cm}^3] \cdot \text{dose conversion coefficient } \left[ \frac{\mu\text{Sv m}^2}{\text{MBq hr}} \right] \quad (5)$$

However, these conversion coefficient are designed to be multiplied by a flux like value (*unit 1/m<sup>2</sup>*). So if you have a gamma emission rate R from a point source at a distance L away from it, then gamma flux at that point would be calculated as:

$$\Phi = R/4\pi L^2 \quad (6)$$

The dose rate value calculate by DCHAIN has this emission rate included but not the geometric component. Therefore, to get an ambient dose equivalent/effective dose rate E at a location at distance L from a point source, given the DCHAIN calculated dose rate D, it follows that:

$$E = D/4\pi L^2 \quad (7)$$

There are 3 main issues that must be taken into account when computing the dose rate as just explained above.

1. If the source is not well-approximated as a point source, the geometric component must be changed accordingly.
2. Since DCHAIN is not spatially aware of the problem geometry it cannot take into account for self-shielding.
3. These dose rate calculated through DCHAIN only consider the decay photon emission.

If doses coming from beta or other emissions are not negligible or the complexity of the geometry leads to self-shielding effect, but also if surrounding materials may be a concerns, a rigorous 2 step approach is required through another iteration with PHITS [19]. This means that the gamma spectra evaluated by DCHAIN is going to be used as photon source in PHITS. Different approach are available in terms of discretization of the source: by region, or mapped either by a bounding box or by the tetrahedrons that composed the imported mesh. The former represent the fastest solution, but may lead to results that are not physically accurate if the geometry does not represent properly the real shape of the component. Contrarily a mapped mesh will increase significantly computational times but result in a more rigorous shutdown dose rate evaluation.

The gamma source is obtained multiplying the gamma energy spectra by the emissivity. The emissivity is automatically computed by DCHAIN multiplying the total gamma-ray flux by the volume of the region of interest. Finally to obtain the effective dose equivalent the flux computed by PHITS (in unit of

$\#/cm^2$ ) will be multiplied by the conversion coefficient ICRP74 (or H(10) for the ambient dose equivalent)<sup>1</sup>. For the sake of completeness dimensional analysis is here provided of the last step of the R2S approach.

$$\frac{\gamma}{s \cdot cm^3} \cdot cm^3 \cdot \frac{1}{cm^2} \cdot \frac{pSv \cdot cm^2}{\gamma} = pSv/sec \quad (8)$$

which can be easily scaled to Sv/hr multiplying by a factor  $k = 3600/10^{12}$ .

---

<sup>1</sup>H(10) conversion coefficients have been taken from EXPACS (<https://phits.jaea.go.jp/expacs/>, ICRP74 can be found in Appendix A

## Results

### TBR

As it was expected the evaluation of Tritium Breeding Ratio (TBR) reveals that CAD A presents lower values with respect to CAD B, with differences higher than 10% and less than 2% for natural and high  ${}^6\text{Li}$  enrichment in FLiBe, respectively. One interesting observation is that the enrichment of  ${}^6\text{Li}$  do not influence the TBR inside the blanket region as much as in the salt coolant channel. Directing attention towards the influence of materials, it becomes evident that variations in tritium breeding ratio are notable. Taking as example CAD B with natural enrichment (similar considerations can be drawn for other configuration with different numerical values) the TBR measurements fluctuate from a minimum of 1.1439 to a maximum of 1.1754, observed in  $\text{GdH}_3$  and SS316L, respectively. The errors associated with these measurements remain consistently low, all approximately on the order of 1E-04. Table 4 illustrates the TBR outcomes for the examined materials.

TBR natural composition ${}^6\text{Li}$ in FLiBe molten salt		
TF shielding material	CAD A	CAD B
$\text{GdH}_3$	1.015	1.144
$\text{GdH}_2$	1.015	1.144
$\text{HfH}_2$	1.016	1.145
VB	1.019	1.145
$\text{TiH}_2$	1.023	1.150
WB	1.021	1.151
$\text{WB}_4$	1.017	1.1473
$\text{B}_4\text{C}$	1.0159	1.1458
WC	1.0294	1.1597
$\text{ZrH}_2$	1.027	1.154
$\text{HfV}_2$	1.027	1.158
void	1.044	1.172
SS316L	1.047	1.175

Table 4: TBR differences between CAD A and CAD B

TBR 90% enrichment of ${}^6\text{Li}$ in FLiBe molten salt		
TF shielding material	CAD A	CAD B
$\text{GdH}_3$	1.2109	1.2265
$\text{GdH}_2$	1.2115	1.2271
$\text{HfH}_2$	1.2122	1.2277
VB	1.2192	1.2347
$\text{TiH}_2$	1.2147	1.2292
WB	1.2206	1.2360
$\text{WB}_4$	1.2170	1.2326
$\text{B}_4\text{C}$	1.2154	1.2311
WC	1.227	1.2413
$\text{ZrH}_2$	1.2171	1.2315
$\text{HfV}_2$	1.2272	1.2419
void	1.2337	1.2469
SS316L	1.2349	1.2473

Table 5: TBR differences between CAD A and CAD B

Notably, hafnium hydride and gadolinium hydrides exhibit comparable performance, with hafnium hydride displaying a slightly elevated TBR of 1.1452 in comparison to  $\text{GdH}_x$ . Conversely,  $\text{TiH}_2$ ,  $\text{ZrH}_2$ , WB and  $\text{HfV}_2$  demonstrate higher TBRs relative to VB and Gadolinium and Hafnium hydrides. Specifically,

$\text{ZrH}_2$  and  $\text{HfV}_2$  showcase elevated TBR values compared to  $\text{TiH}_2$ , with differences exceeding 1.2% for the case of  $\text{HfV}_2$  when compared to Gadolinium and Hafnium hydrides. Vanadium Boride manifests TBR values similar to  $\text{HfH}_2$  in CAD B, while shows intermediate results among the analyzed materials in CAD A due to the reduced Blanket size.

The results shown that the variations primarily concentrate on the Blanket region area, whereas the Salt coolant channel exhibit similar values across the different TF shield material choices. Precisely, the salt coolant channel is more influenced by the geometry thickness and  ${}^6\text{Li}$  enrichment. The deployment of FLiPb instead of FLiBe leads to a reduction of the TBR, Figure 8. Figures 4, 5, 6 and 7 show the variation on the Blanket region for analyzed configurations in this work.

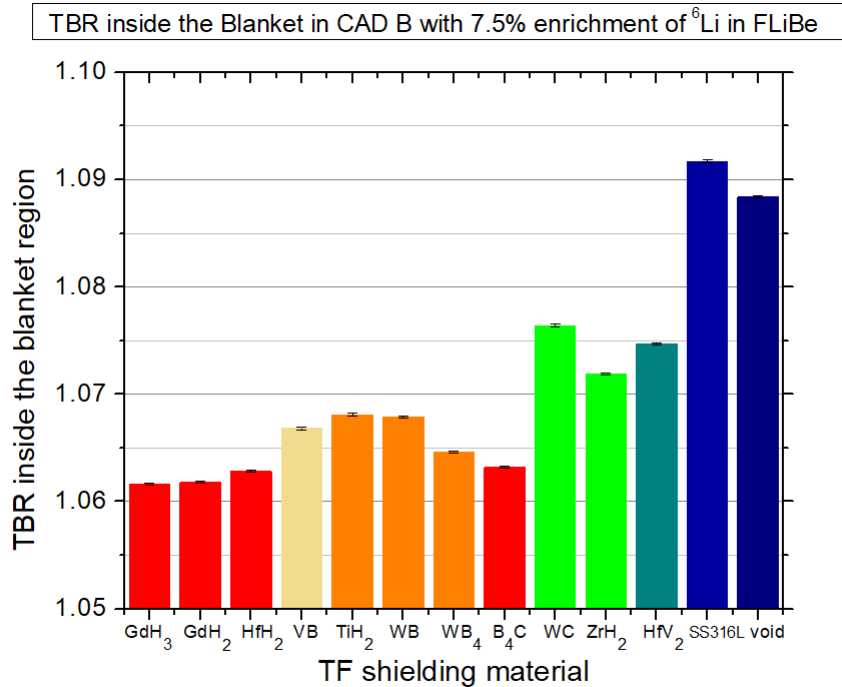


Figure 4: TBR evaluated inside the Blanket region for different TF shield materials. The evaluation was made with  $4.75\text{E+07}$  particles in CAD B

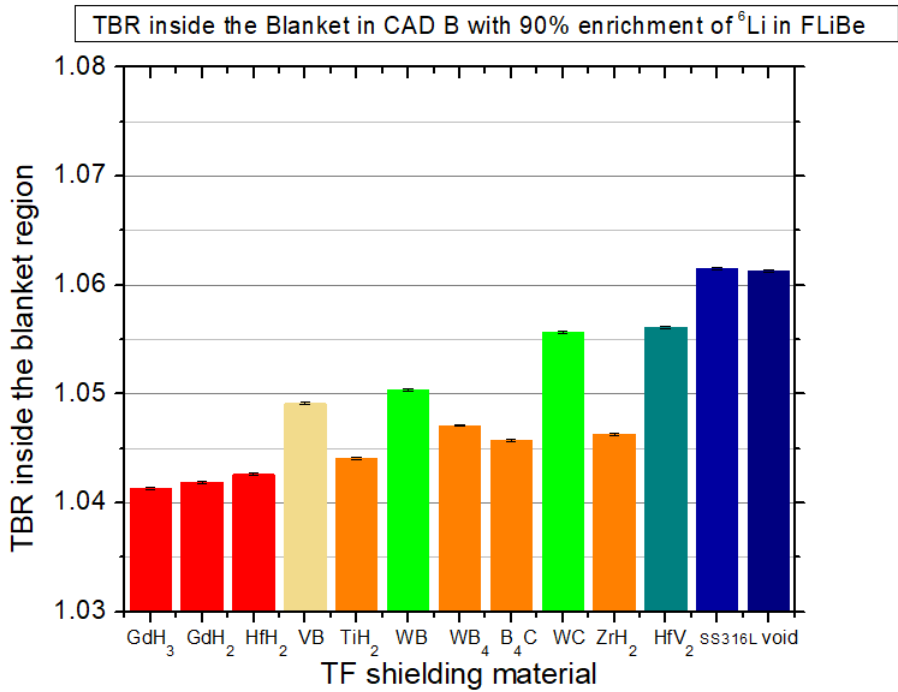


Figure 5: TBR evaluated inside the Blanket region for different TF shield materials. The evaluation was made with 4.75E+07 particles in CAD B

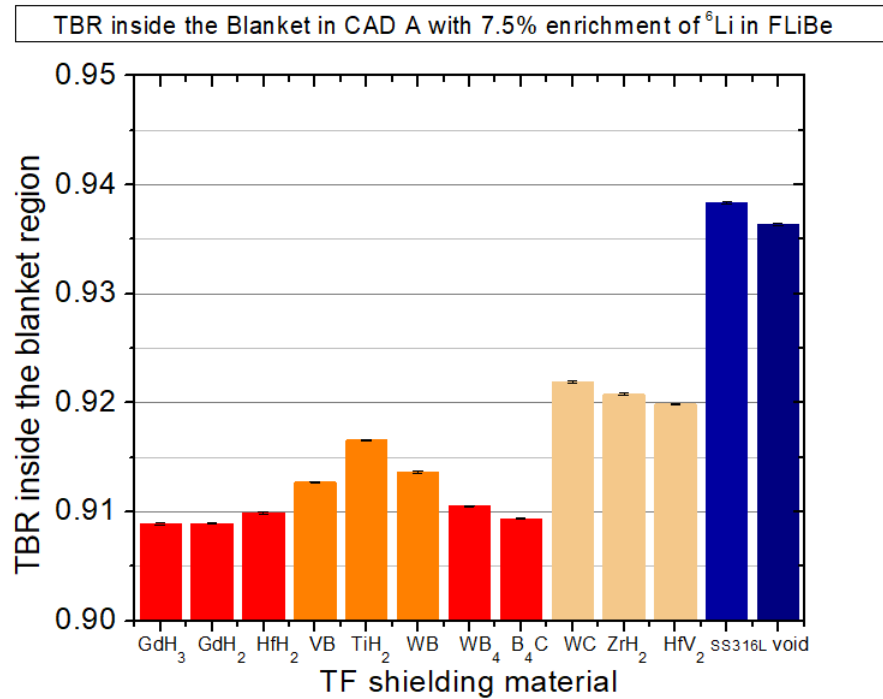


Figure 6: TBR evaluated inside the Blanket region for different TF shield materials. The evaluation was made with 4.75E+07 particles in CAD A

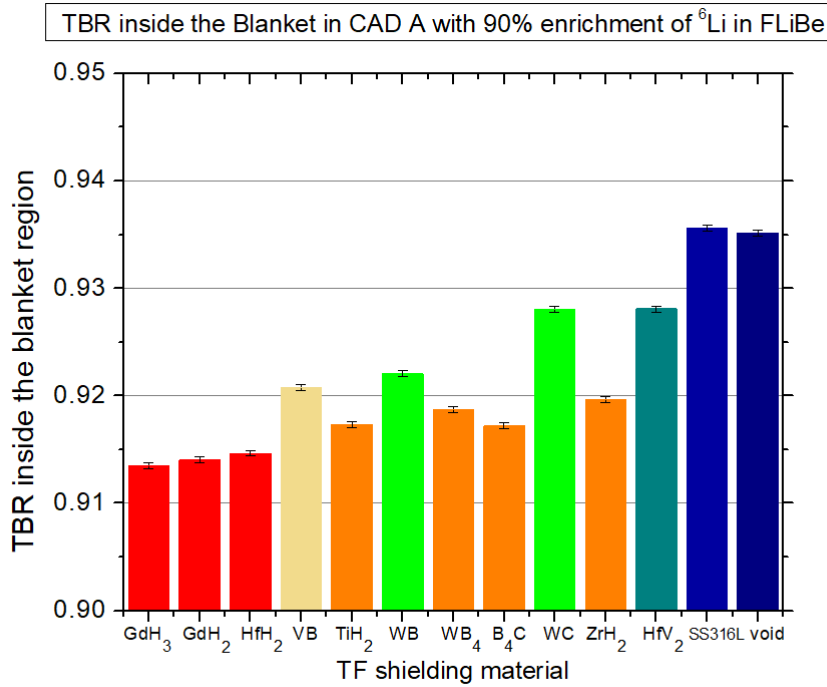


Figure 7: TBR evaluated inside the Blanket region for different TF shield materials. The evaluation was made with 4.75E+07 particles in CAD A

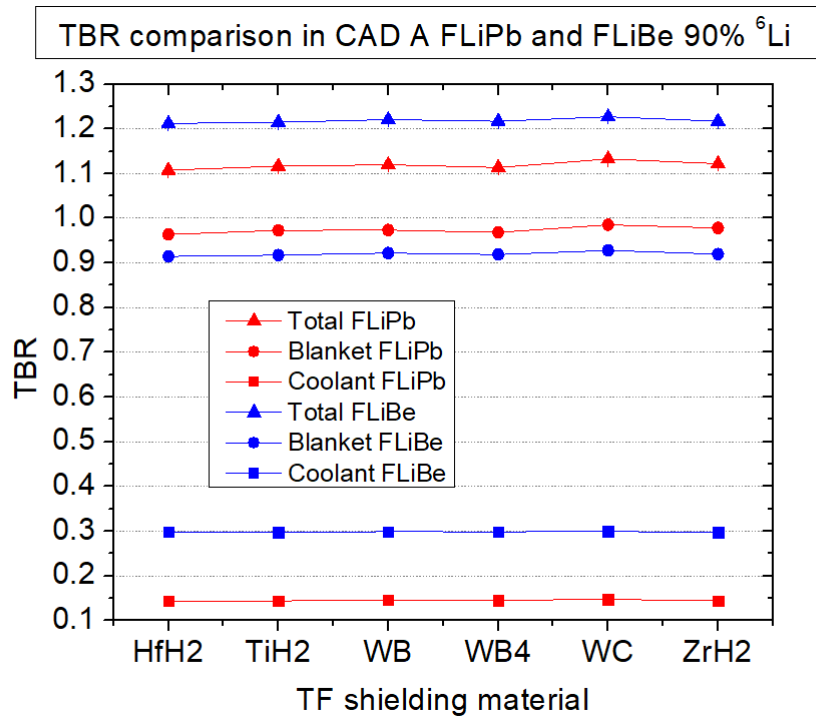


Figure 8: TBR comparison between FLiBe and FLiPb both at 90% enrichment of  ${}^6\text{Li}$

## Integral neutron flux

Now that TBR has been evaluated, it is possible to proceed to the evaluation of the neutron environment trying to understand if and how shielding properties are related to the tritium breeding. All the fluxes have been evaluated on the most critical HTS region. Figure 9a shows the integral flux maps in the case in which TF shield is void-filled.

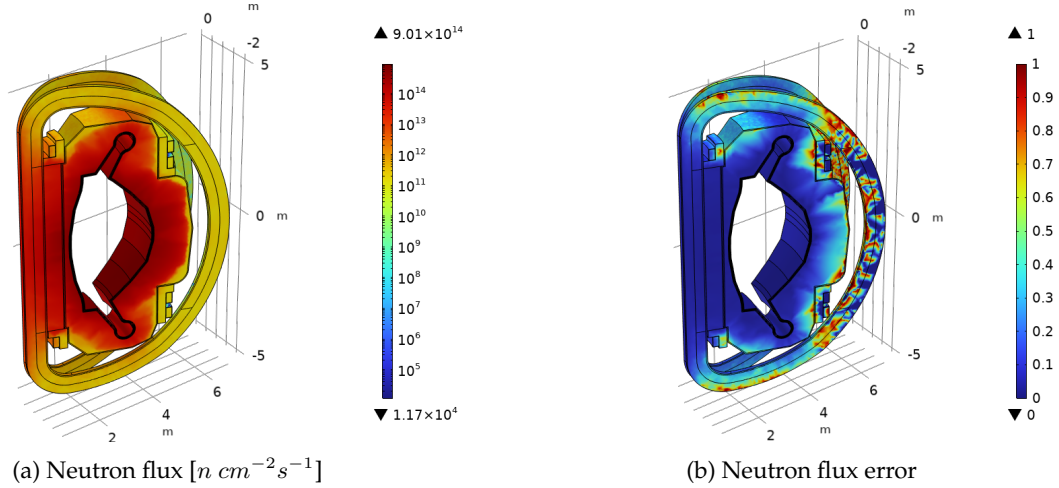


Figure 9: Neutron flux map simulating 4.75E+07 particles without VR techniques. TF shield here represented was filled with void

Those values possess sufficient statistical significance to be considered reliable for this purpose. In fact the TF superconducting coil was divided in 4 different regions. One of these regions is in correspondence of the inboard TF. As it can be seen from Figure 9b in the case of a void shield enough particles reach the TF region to obtain relative errors  $< 10\%$ . The other sides of the TF exceed 40% up to the case in which values are not reliable anymore. For this reason only the part shielded is considered in the evaluation. As a matter of fact this is the most critical region in terms of neutron environment.

The scenario shifts when tangible materials replace the void. Under those circumstances, statistical uncertainties rise, implying a necessity for a greater number of particles. Consequently, computational time will increase. For this reason, variance reduction techniques have been employed to mitigate this issue. As demonstrated in Figures 10a and 11a, the neutron flux map, when a shield is present, does not accurately represent the neutron environment. Utilizing the same number of particles and computational resources, variance reduction techniques not only enhance statistical accuracy but also decrease computational time.

Table 6 shows the integral neutron fluxes assessed using 4.75E+07 particles. This evaluation compares scenarios where the toroidal field (TF) shield is void-filled and composed of zirconium hydride ( $\text{ZrH}_2$ ), with simulations conducted both with and without VR techniques. Additionally, the table delineates the computational costs associated with each simulation.

Integral neutron flux			
Simulation	Integral neutron flux $[n \text{ cm}^{-2} \text{s}^{-1}]$	r.err. [%]	CPU time [s]
void	1.19E+14	0.0001	1.00E+06
void with VR	1.1875E+14	0.003	2.50E+05
$\text{ZrH}_2$	6.6250E+10	0.0429	9.00E+05
$\text{ZrH}_2$ with VR	5.5722E+10	0.0356	1.50E+05

Table 6: Results computed with 4.75E+07 particles

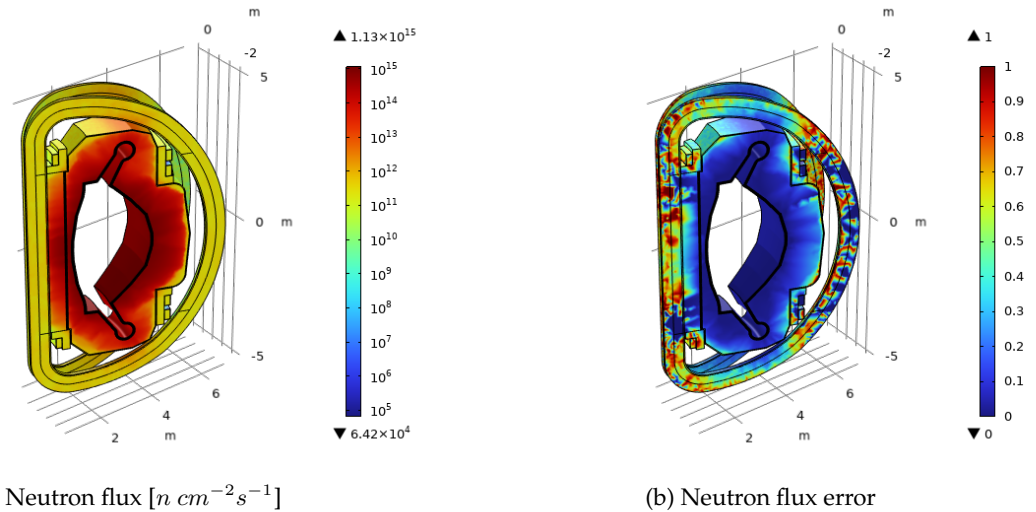


Figure 10: Neutron flux map simulating 4.75E+07 particles without VR techniques. TF shield here represented is made of  $\text{ZrH}_2$

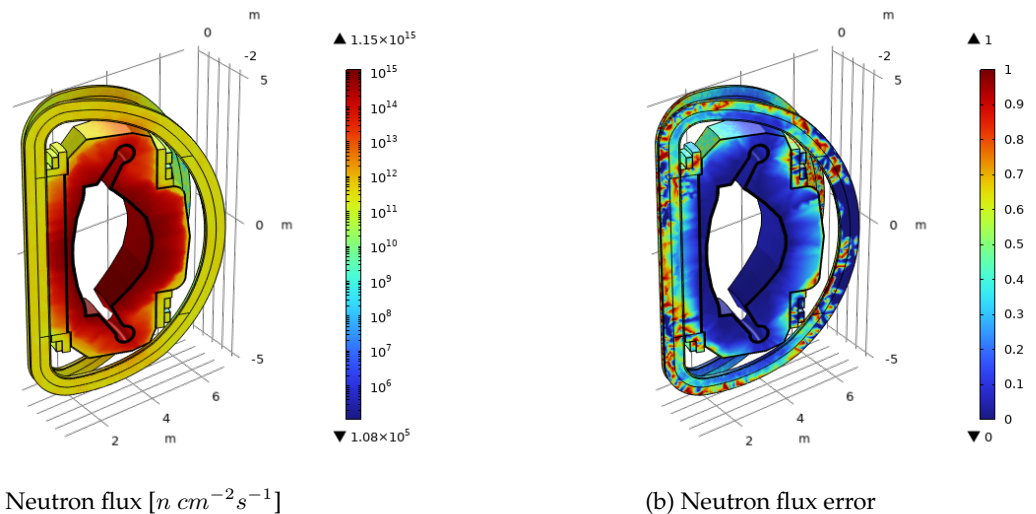


Figure 11: Neutron flux map simulating 4.75E+07 particles with VR techniques. TF shield here represented is made of  $\text{ZrH}_2$

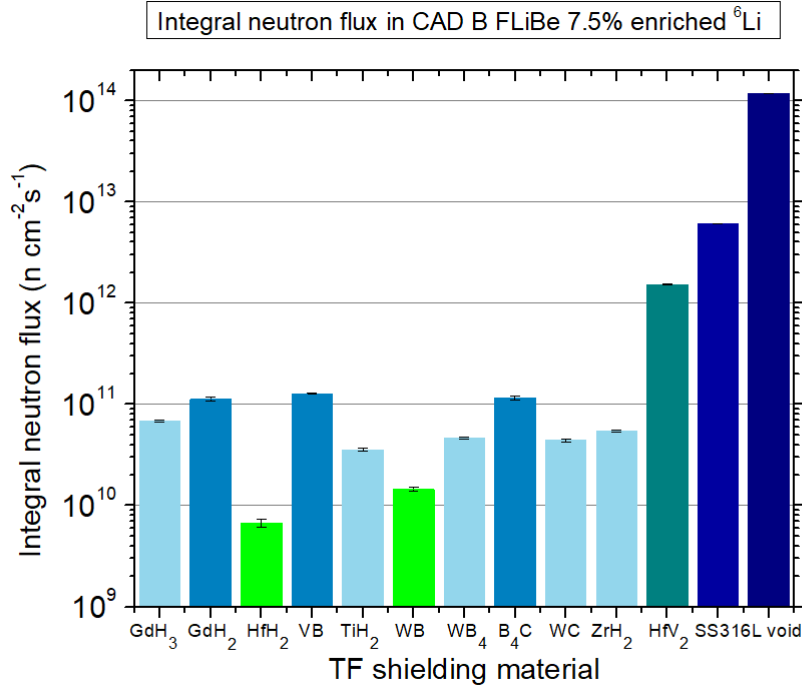


Figure 12: Integral neutron fluxes evaluated using VR techniques on the most critical region of the HTS for different TF shield materials.

Neutron fluxes in 90% enriched  ${}^6\text{Li}$  showcase lower values when compared to the lower enrichment, because of the greater number of thermal neutrons. When FLiPb replace FLiBe instead, due to the lower amount of Li in the former case, fluxes increase as it was expected (Figure 17). Between the different material analyzed as TF shield hafnium hydride shows the lower neutron flux, followed by WB, WC and WB<sub>4</sub>. The rest of the material reveal an ascending trend from ZrH<sub>2</sub> to the unshielded case for different configurations, but by no means all. In fact it is noteworthy that TiH<sub>2</sub> shows lower value of integral neutron flux with respect to zirconium hydride, but for the most critical configuration (CAD B with natural FLiBe composition). Figures 12, 13 and 15 show the Integral neutron fluxes simulating 4.75E+07 particles using VR. Figure 16 summarize the mentioned results for all the analyzed design configurations.

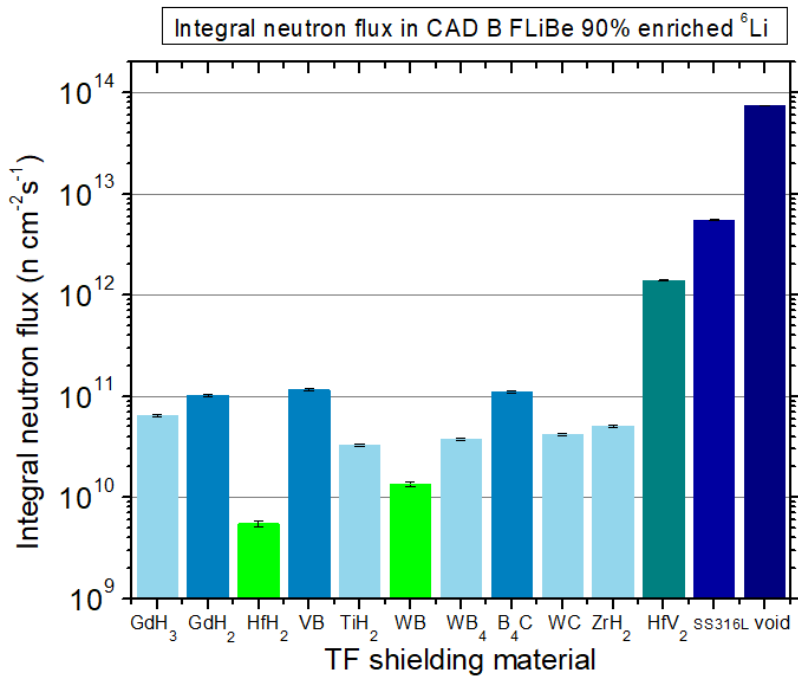


Figure 13: Integral neutron fluxes evaluated using VR techniques on the most critical region of the HTS for different TF shield materials.

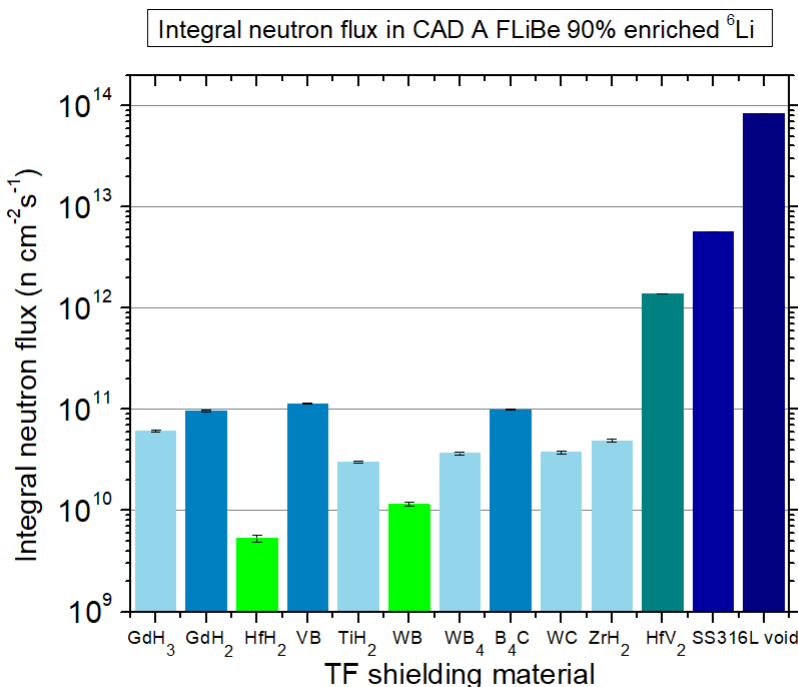


Figure 14: Integral neutron fluxes evaluated using VR techniques on the most critical region of the HTS for different TF shield materials.

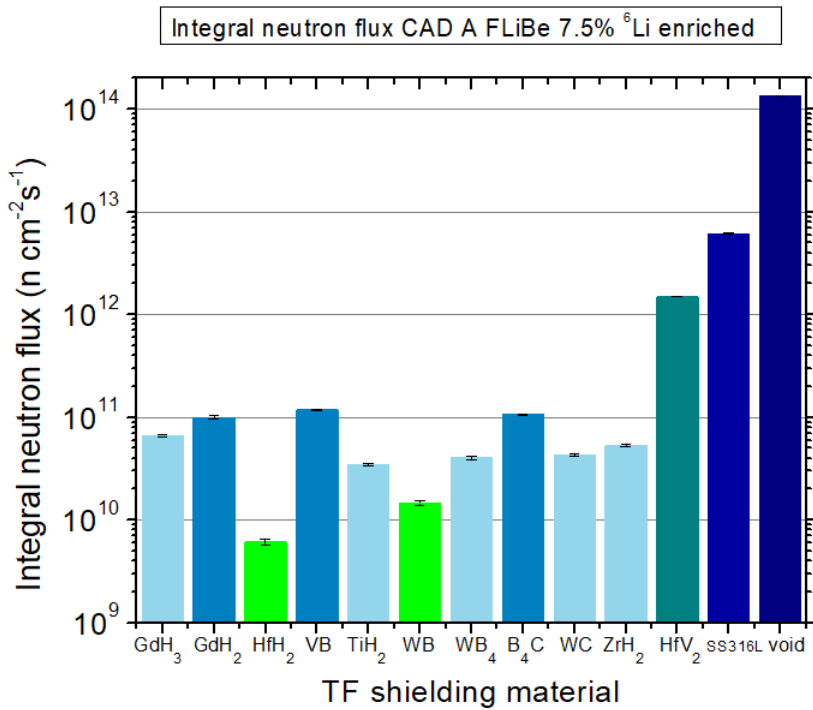


Figure 15: Integral neutron fluxes evaluated using VR techniques on the most critical region of the HTS for different TF shield materials.

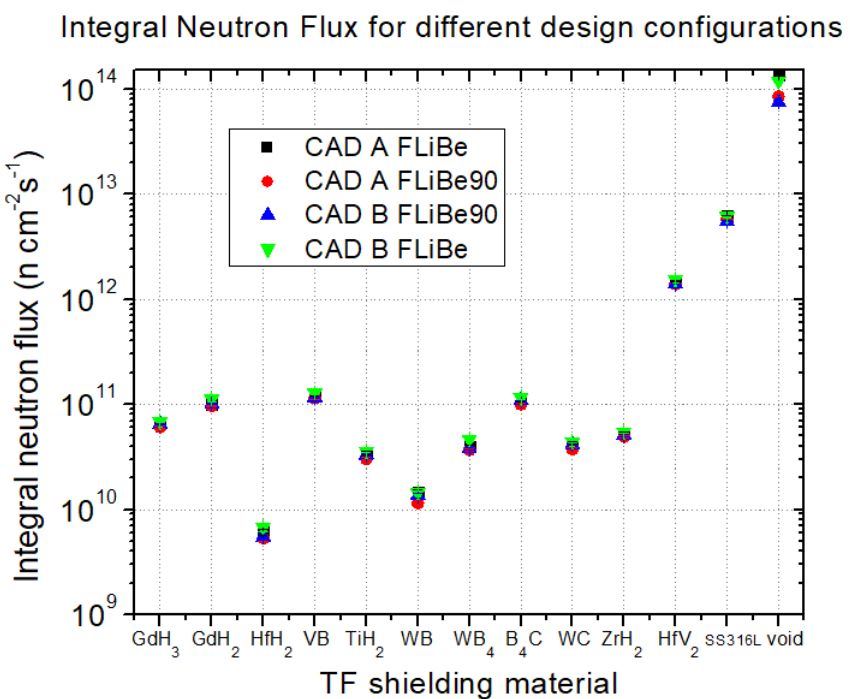


Figure 16: Integral neutron fluxes evaluated using VR techniques on the most critical region of the HTS for all the analyzed cases.

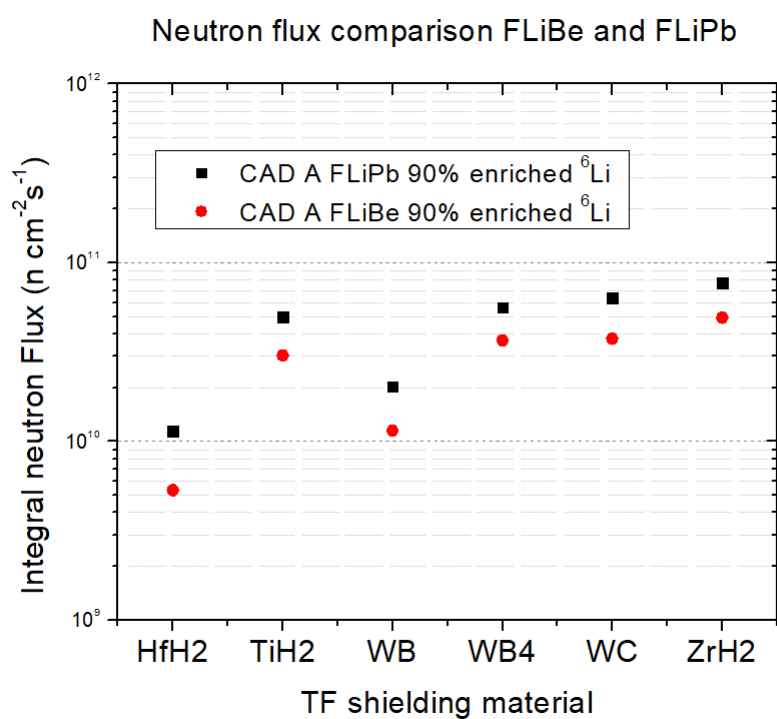


Figure 17: Integral neutron fluxes comparison between FLiBe and FLiPb both at 90% enrichment of  $^6\text{Li}$

## Neutron spectra

The neutron spectra were evaluated for all materials under analysis. This evaluation was conducted employing variance reduction techniques for all materials, whereas for zirconium hydride and void (CAD B natural FLiBe composition), the assessment was performed also without the application of VR techniques. Figure 18 illustrate the comparison between the spectra evaluated both with and without VR. Utilization of weight windows result in drastically decreasing relative errors as it can be seen from the error bars in Figure 19. For this reason the neutron environment were computed for all the materials and different configurations, using VR, as it is shown in Figures 20 and 21 . All the neutron spectra have been evaluated on the most critical HTS region.

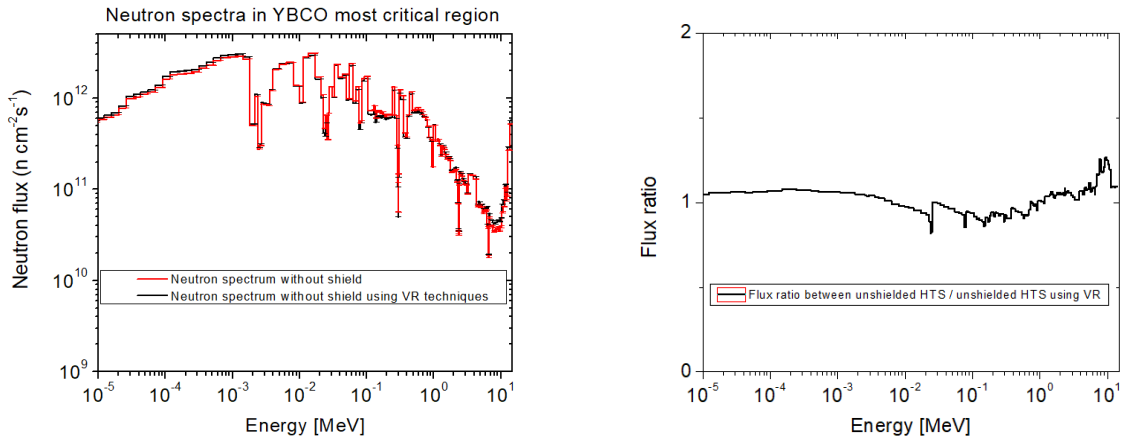


Figure 18: Neutron spectra (left) and neutron spectra ratio (right) in the unshielded TF case, with and without the use of variance reduction techniques

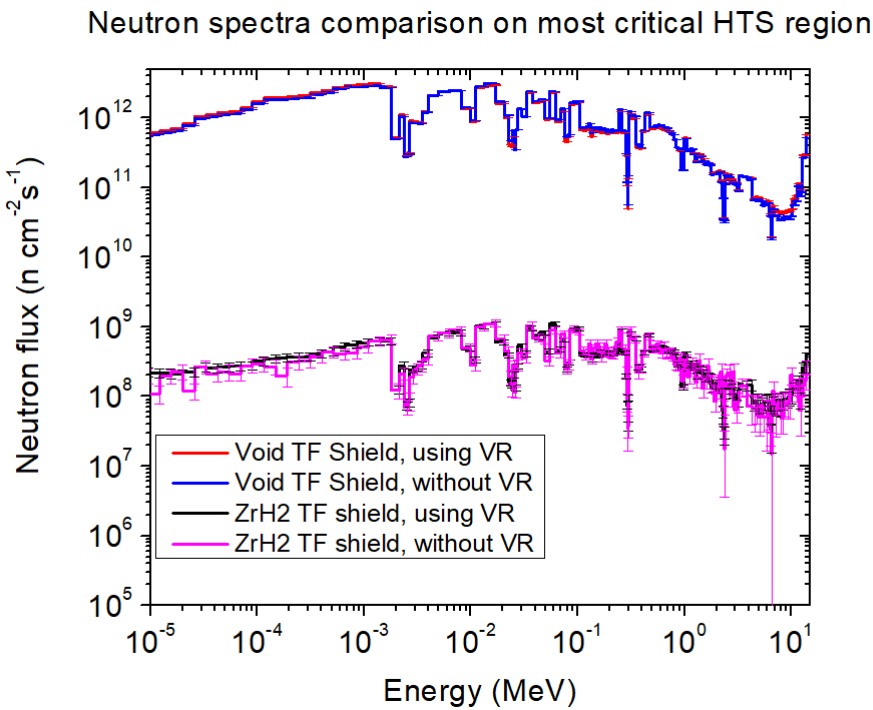


Figure 19: Neutron spectra comparison between void and ZrH<sub>2</sub> TF shields, both with and without the use of variance reduction techniques

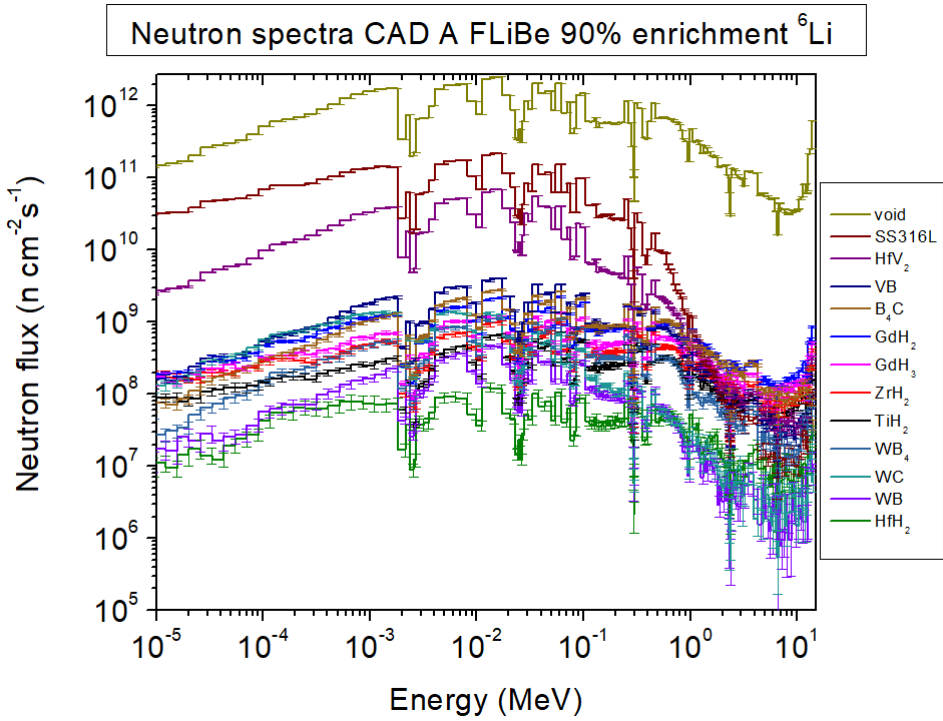


Figure 20: Neutron spectra comparison between all the analyzed materials, using VR techniques

The results are consistent with the previous analysis on the integral neutron fluxes. In fact hafnium hydride and tungsten boride presents the lowest neutron spectra, followed by WC, WB<sub>4</sub>, TiH<sub>2</sub>, ZrH<sub>2</sub> and gadolinium hydrides confirming the superior shielding property compared with the adjunct materials under investigation in this study.

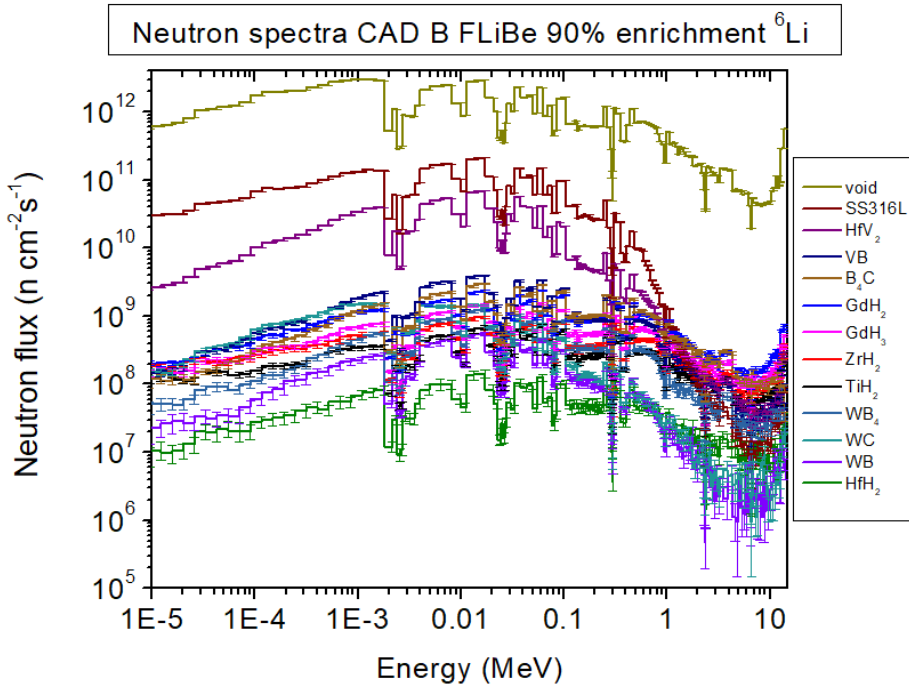


Figure 21: Neutron spectra comparison between all the analyzed materials, using VR techniques

Moreover the neutron spectra provides important information about the energy distribution, enhancing the difference for  $\text{TiH}_2$  based on the design configurations. Furthermore some of the aforementioned materials are noteworthy namely  $\text{HfH}_2$  (that shows the lowest neutron spectra), WB and WC (which as well presents good shielding properties) and titanium and zirconium hydrides (which are the most cost-effective). Low enrichment of  ${}^6\text{Li}$  as well as lower vacuum vessel thickness lead to higher neutron spectra as it shown in Figures 22 and 23. As expected FLiPb leads to higher neutron spectra in terms of magnitude, as it is shown in Figure 24, while also for other TF shielding materials the flux ratio is similar to the one reported in 25.

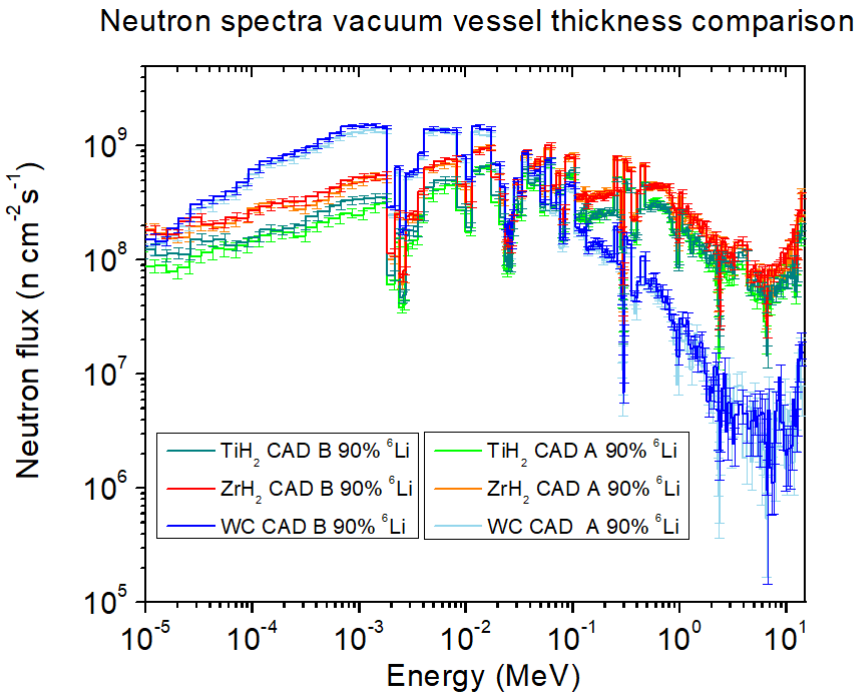


Figure 22: Neutron spectra comparison between the most relevant materials CAD A has 5 cm vacuum vessel thickness (both inner and outer), CAD B has 2 cm vacuum vessel thickness (both inner and outer).

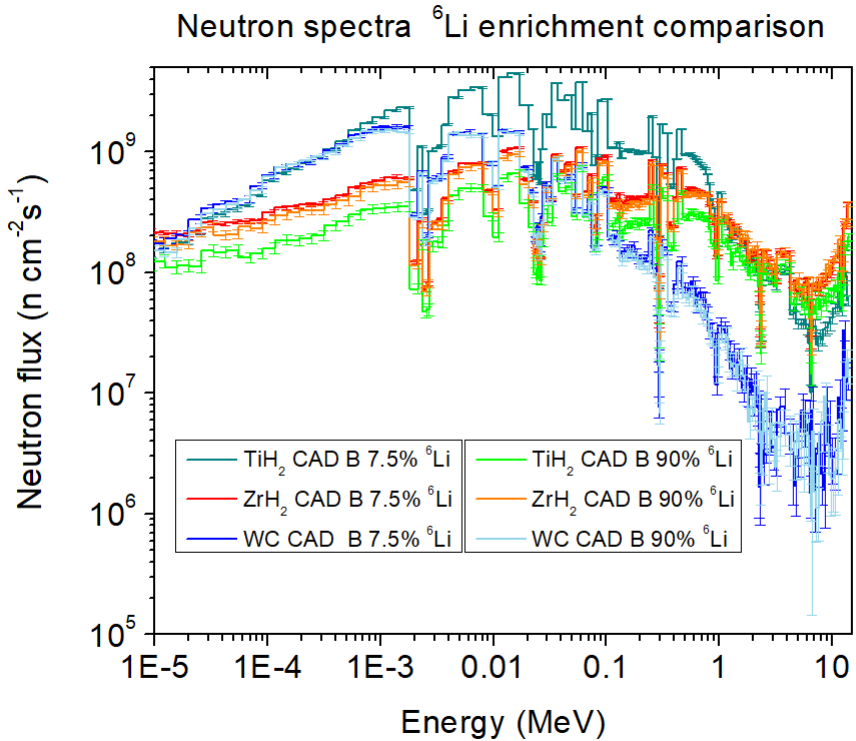


Figure 23: Neutron spectra comparison between the most relevant materials CAD A has 5 cm vacuum vessel thickness (both inner and outer), CAD B has 2 cm vacuum vessel thickness (both inner and outer).

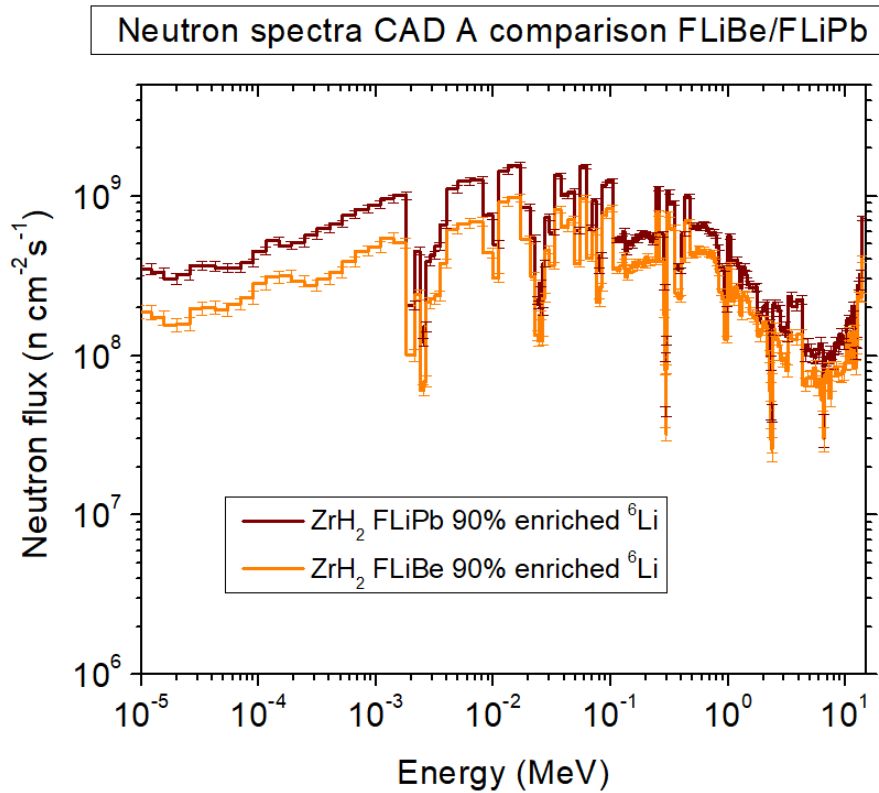


Figure 24: Neutron spectra comparison for the two molten salt configurations analyzed.

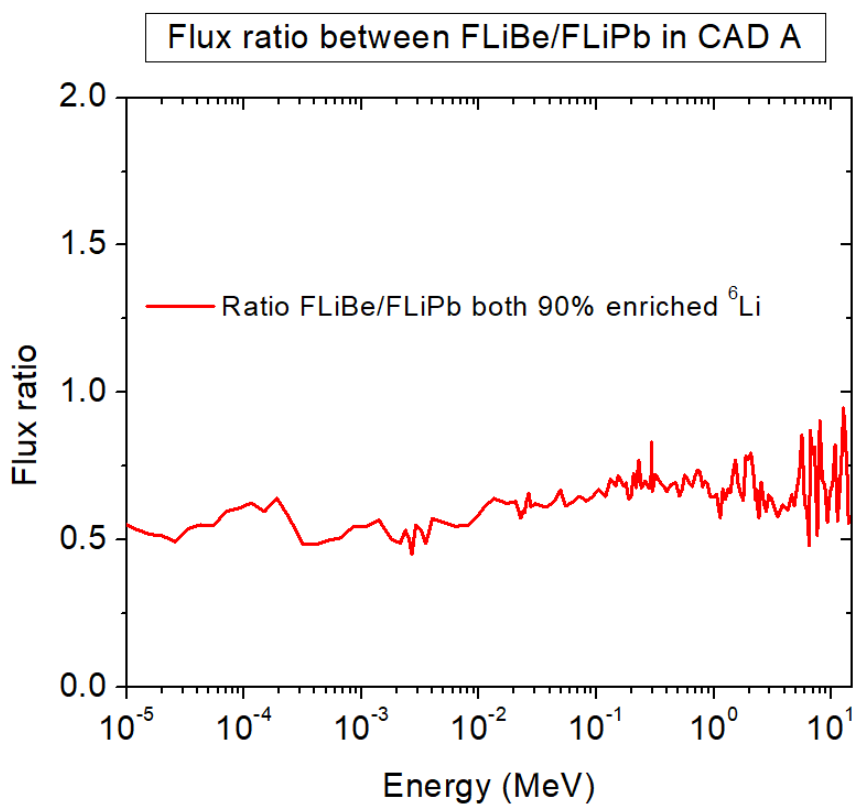


Figure 25: Neutron spectra ratio for the two molten salt configurations analyzed using  $\text{ZrH}_2$ , similar results also for different TF shield materials.

## PKA spectra & DPA

Primary Knock-on atoms represent a crucial step in evaluating the radiation damage in order to further investigate the defects morphology through Molecular dynamics (MD) simulations. To this purpose it is then employed SPECTRA-PKA. The displacement per atom (dpa) measures convert the energy deposited into a material due to irradiation into a single number. Whereas it finds well agreement with various radiation phenomena, it is not suitable to distinguish between different type of irradiation. At last, but not least, dpa does not extend information about damage evolution [33]. Nevertheless dpa after 1 FPY has been evaluated for all the different scenarios with 4.75E+07 particles from the previous neutron spectra. The results (Figure 26) summarize the previous results improving clarity of representation. The slightly difference from the recent work [14] may find a reasonable explanation in the dissimilarities of both geometry parameters design and materials choice. Moreover Figure 27 shows the comparison between FLiPb and FLiBe in CAD A for some of the most interesting configurations. Figure 28 shows the PKA spectrum when TF coil shield is  $\text{ZrH}_2$  (right) and void-filled (left) both computed in the most critical HTS region for CAD A in FLiBe 90% enriched of  ${}^6\text{Li}$  composition, taking as input the neutron spectra shown in the previous section.

DPA after 1 year for different design configurations

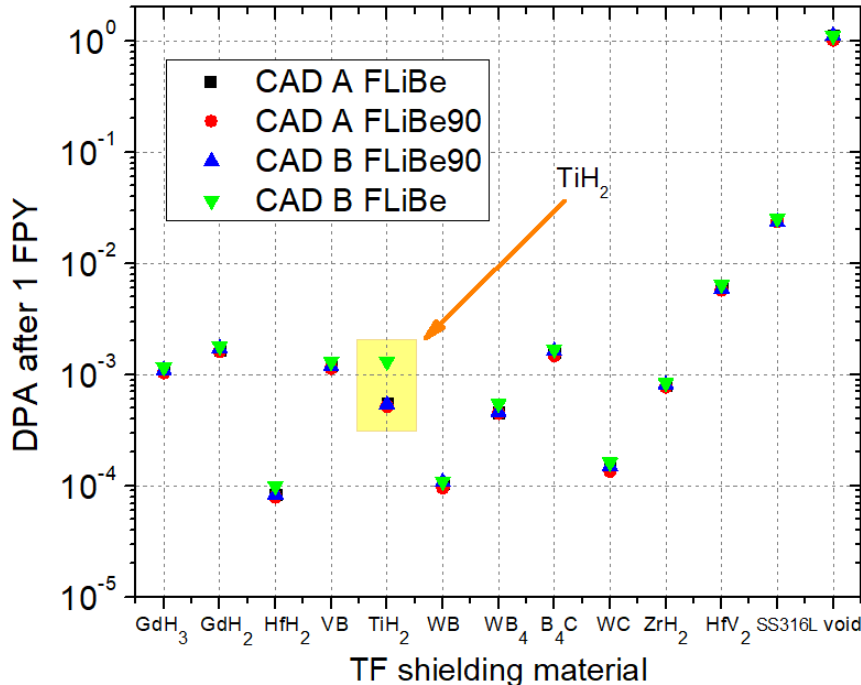


Figure 26: NRT-dpa after 1 FPY on the most critical HTS region computed through SPECTRA-PKA

The results find a good agreement with literature [12]. The PKA spectra for all the other configurations can be found (or will be found) in Appendix B. As expected the results are complementary of the neutron spectrum. Furthermore PKA spectra provide additional information about the starting point of the cascade damage in YBCO due to irradiation. In Figure it is shown a comparison of the PKA spectra between the thicker vacuum vessel configuration (CAD A) in high  ${}^6\text{Li}$  enrichment and CAD B in natural FLiBe composition, both with  $\text{TiH}_2$  toroidal field shield.

### DPA after 1 FPY comparison FLiBe and FLiPb

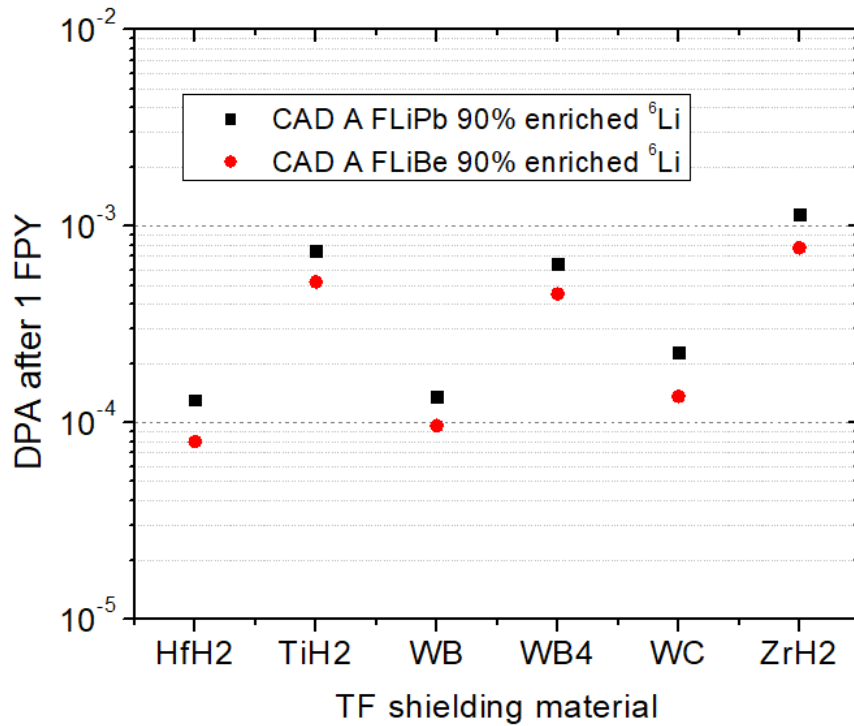
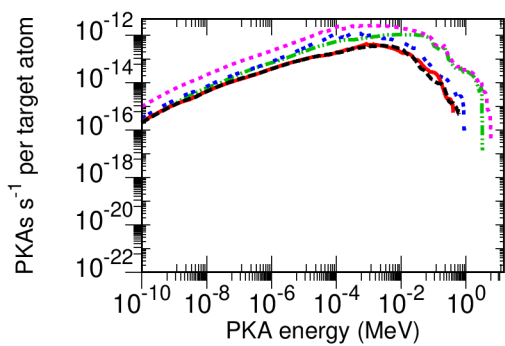


Figure 27: NRT-dpa after 1 FPY on the most critical HTS region computed through SPECTRA-PKA

PKA spectrum on YBCO with void shield



PKA spectrum on YBCO with ZrH<sub>2</sub> shield

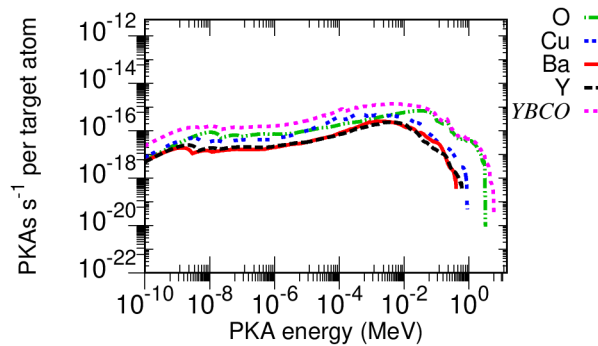
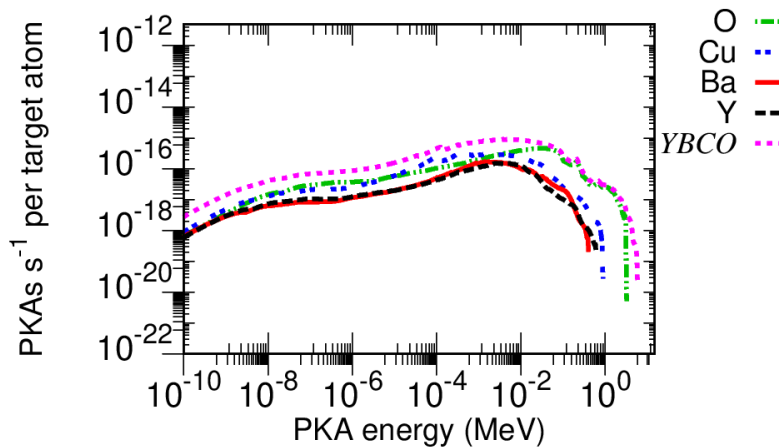


Figure 28: PKA spectra with 51 cm ZrH<sub>2</sub> shield (right) and void (left), both from the neutron spectra computed for CAD A in high  $^6\text{Li}$  enrichment

PKA spectrum on YBCO with  $\text{TiH}_2$  shield



PKA spectrum on YBCO with  $\text{TiH}_2$  shield

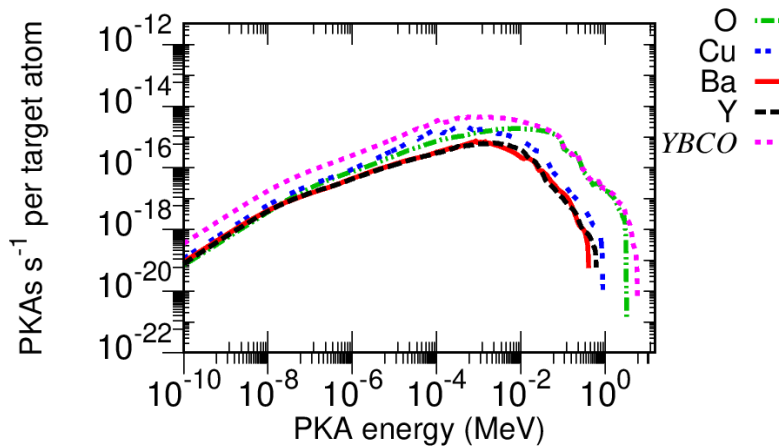


Figure 29: PKA spectra comparison between CAD A high enriched configuration (up) and CAD B low enriched configuration (down), both with 51 cm  $\text{TiH}_2$  shield

## Activity and dose rate

Evaluation of the specific activity and dose rate have been performed due to the recent developments in Phits and Dchain [19]. For this reason I made a different geometry in order to be able to compare the results with literature [24]. The main parameters are listed in table 7. Figure 30 illustrate the geometry meshed.

Main geometry features		
Parameters	CAD A	CAD C
Outer vacuum vessel thickness	5 cm	5 cm
Beryllium layer thickness	1 cm	1 cm
FLiBe channel thickness	2 cm	2 cm
Inner vacuum vessel thickness	5 cm	5 cm
First wall (FW) armature	0.5 cm	1.5 cm

Table 7: Geometry made to compare the results with literature [24]

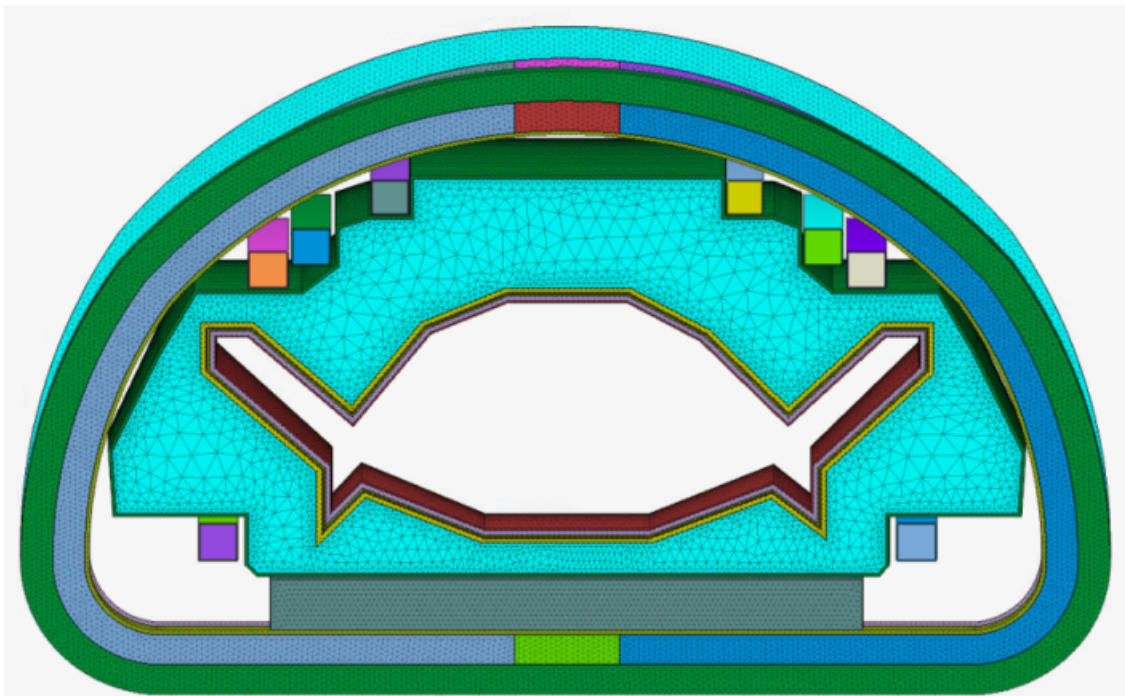


Figure 30: Geometry closer to the actual reference for neutronic simulation by Commonwealth Fusion Systems (CFS). Made by the author in Solidworks and meshed through Altair Simlab.

Precisely vacuum vessel materials V4Cr4Ti, F82H and SiC have been evaluated considering an irradiation time of 2 EFPY analyzing the specific activity and a cooling periods of 1 day, 30 days, 1 year and 2 years after the irradiation. For the SDR a R2S method has been used in order to impose the gamma source (calculated by DCHAIN from the output of the first simulation in Phits) in the vacuum vessel geometry. The results of the specific activity underscore the capabilities and appropriateness of V4Cr4Ti and SiC as a candidate material for structural components. F82H demonstrates greater activity levels, surpassing V4Cr4Ti by one order of magnitude and SiC by three orders of magnitude, one day post-irradiation. Results are shown in Figure 31.

Keeping V4Cr4Ti as structural material, and using FLiPb instead of FLiBe results into slightly different activity levels as it shown in Figures 32 and 33. In particular, since the neutral flux in FLiPb configuration is higher, the activity of the structural materials as well will increase. Conversely for the salt coolant channel and blanket component the specific activity will decrease due to the fact that main contributor is  $^{3}\text{He}$ , which is diminished as a consequence of the reduction of Li in the material compared to FLiBe

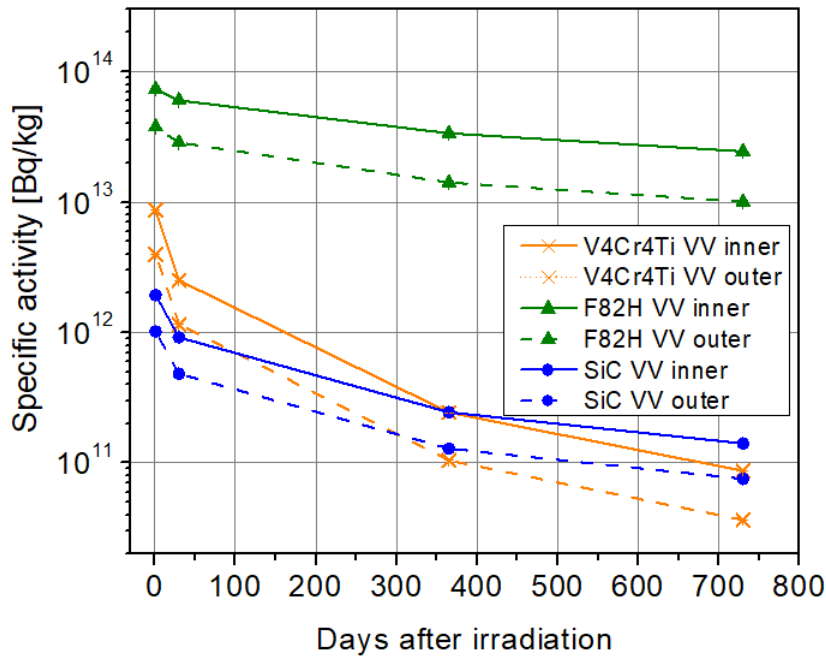


Figure 31: Specific activity for different structural component designs

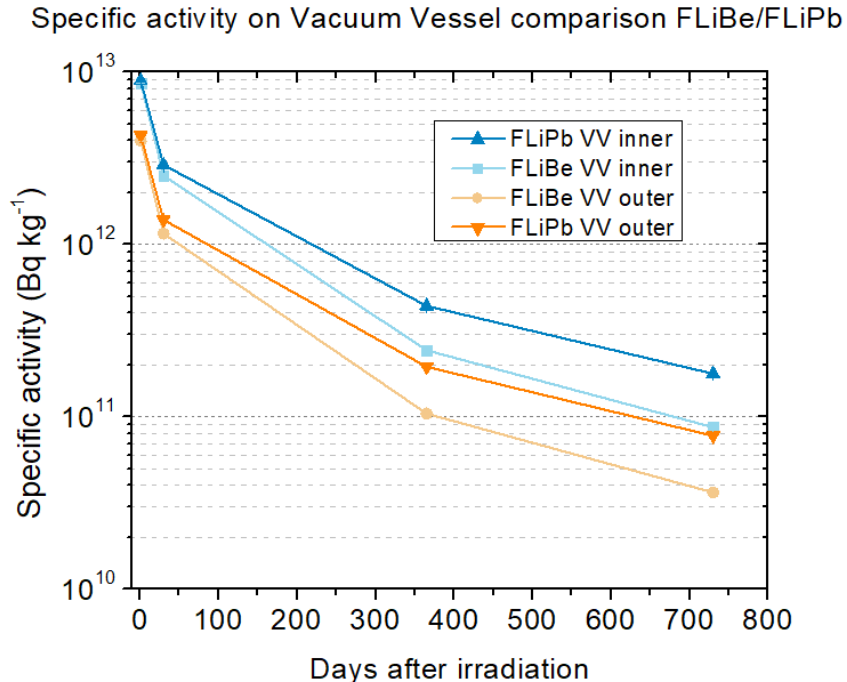


Figure 32: Specific activity of the vacuum vessel for different molten salt designs.

at same enrichment.

The main analysis have been carried out only for V4Cr4Ti. Figure 34 and 35 show the main radioactive isotopes in the vacuum vessel deploying FLiBe as coolant and blanket 1 day and 2 year after the irradiation, respectively. The main product  $^{48}\text{Sc}$  derives from  $(n, x)$  reaction from  $^{48}\text{Ti}$ ,  $^{49}\text{Ti}$  and  $^{51}\text{V}$  or from  $\beta^-$

### Specific activity FLiBe - FLiPb comparison

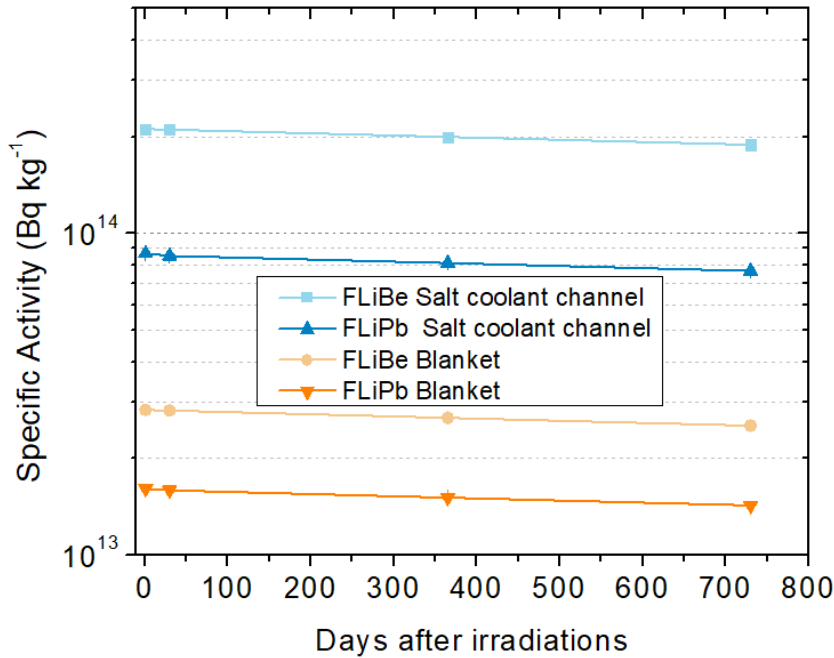


Figure 33: Specific activity of the vacuum vessel for different molten salt designs.

from  $^{48}\text{Ca}$ . After two years the main isotopes contribution are  $^{49}\text{V}$  (half life is  $2.850\text{E+}07$  s),  $^{45}\text{Ca}$  (half life  $1.405\text{E+}07$  s) and  $^{3}\text{He}$  (half life  $3.888\text{E+}08$  s).

V4Cr4Ti4 =  $6.31753\text{e+}12$  Bq/kg, 1 day after shutdown

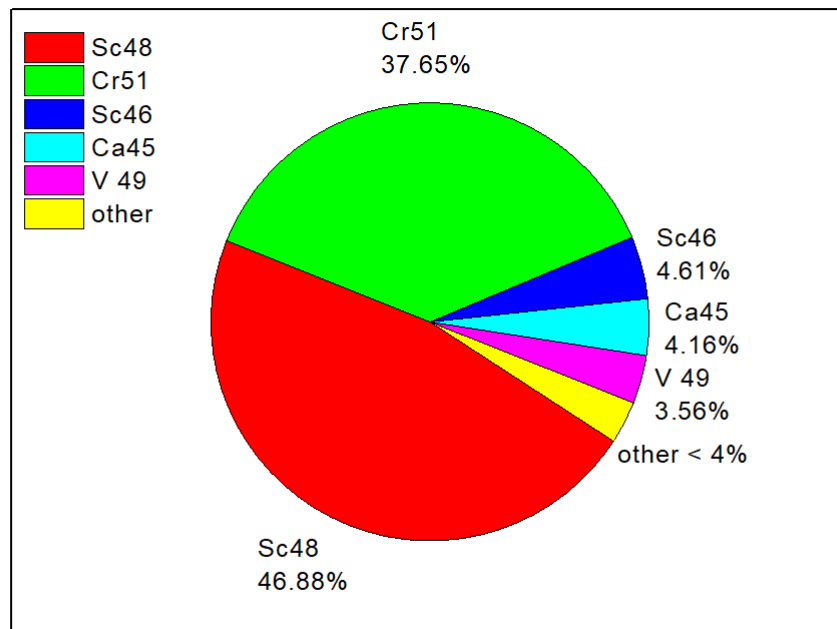


Figure 34: Main isotopes contribution average between vacuum vessel inner and outer 1 day after the shutdown.

V4Cr4Ti = 4.3539e10 Bq/kg, 2 years after shutdown

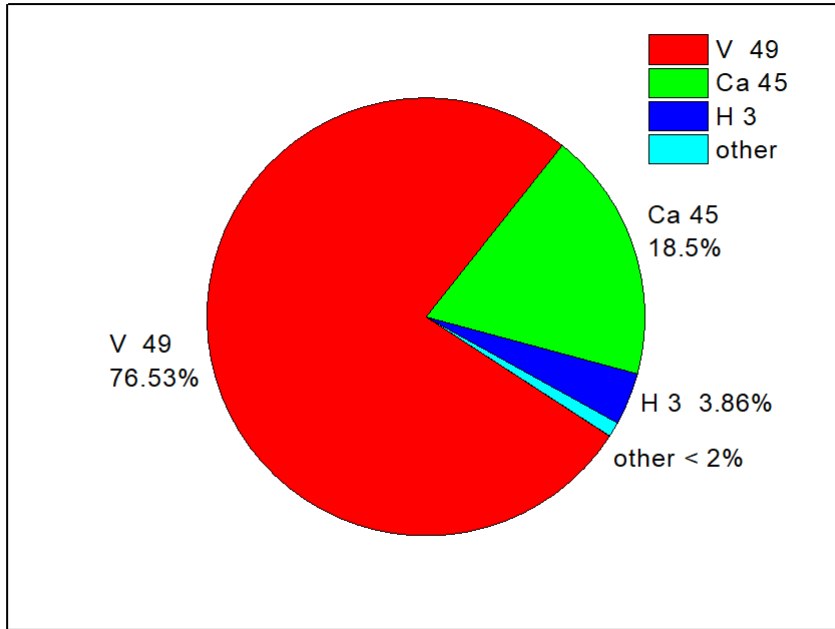


Figure 35: Main isotopes contribution average between vacuum vessel inner and outer 2 years after the shutdown.

Figures 36 and 37 show the main isotopes contributions of the vacuum vessel inner 1 day and 2 years after the shutdown when FLiPb is selected as molten salt.

Moreover Table 8 and 9 illustrate the decay heat of V4Cr4Ti vacuum vessel after 2 EFPY as a function of time. The primary contribution arise from decay gamma emissions, with decay beta observed at levels one order of magnitude lower across all considered output times. Decay alpha emissions are absent. Nevertheless the overall decay heat is not worrisome for this type of material. Concerning the decay heat of the molten salt, variations can be observed if FLiPb is deployed instead of FLiBe. More precisely the overall decay heat remains the same since beta decay does not change significantly. However the decay gamma increase and alpha decay are present due to not worth bothering about trace of  $^{210}\text{Po}$ . In fact taking into account the vacuum vessel (inner and outer) and FLiPb molten salt the percentage of  $^{210}\text{Po}$  1 day after shutdown is 0.0005%. Considering only the Salt coolant channel the trace of  $^{210}\text{Po}$  are 0.02% 1 day after the shutdown, which halve during the first year of cooling.

Total activity and decay heat after irradiation				
Parameter	1 day	30 day	1 year	2 year
Total activity [Bq/cm <sup>3</sup> ]	5.23451E+10	1.51422E+10	1.46987E+09	5.25497E+08
Total decay heat [W]	1.6498E+04	7.9449E+02	5.0958E+01	3.7817E+00
Decay beta [W]	1.0872E+03	7.0480E+01	9.0731E+00	1.6822E+00
Decay gamma [W]	1.5411E+04	7.2401E+02	4.1885E+01	2.0994E+00

Table 8: V4Cr4Ti vacuum vessel inner decay heat and specific activity as a function of time. Relative errors lower than 0.05%.

The SDR was computed only for the V4Cr4Ti configuration, which is the main structural material under investigation in this study. The results 1 day after irradiation, computed as explained in *Shutdown* section using a mapped mesh consent to individuate the most activated area of the vacuum vessel (Figure 38).

Using this approach results that the main activated regions would be near the divertor regions. There is no evidence in literature that this should be the actual behavior of the specific activity. Despite that,

V4Cr4Ti inner VV = 8.8892E12 Bq/kg, 1 day after shutdown

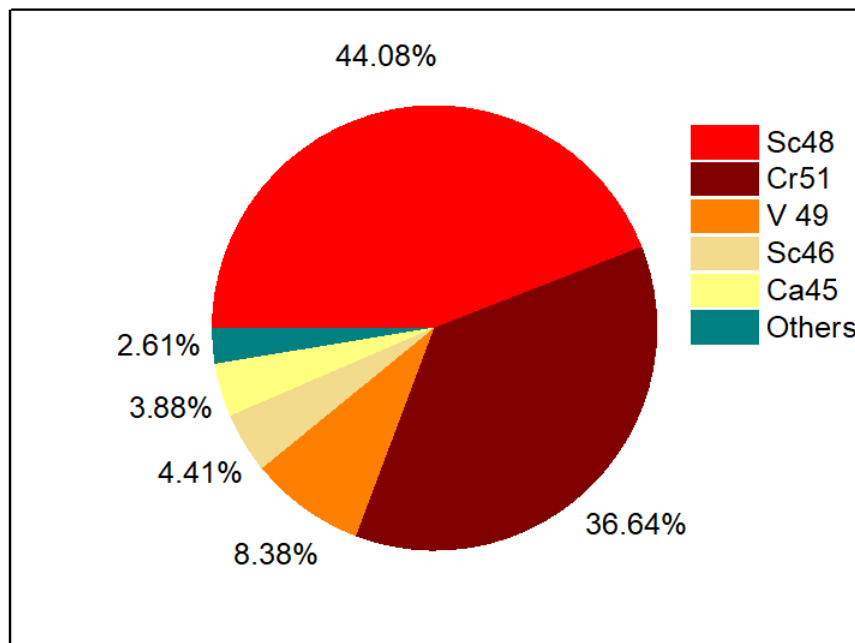


Figure 36: Main isotopes contribution on V4Cr4Ti vacuum vessel inner using FLiPb as coolant and blanket 1 day after the shutdown.

V4Cr4Ti inner VV = 1.7759E11 Bq/kg, 2 years after shutdown

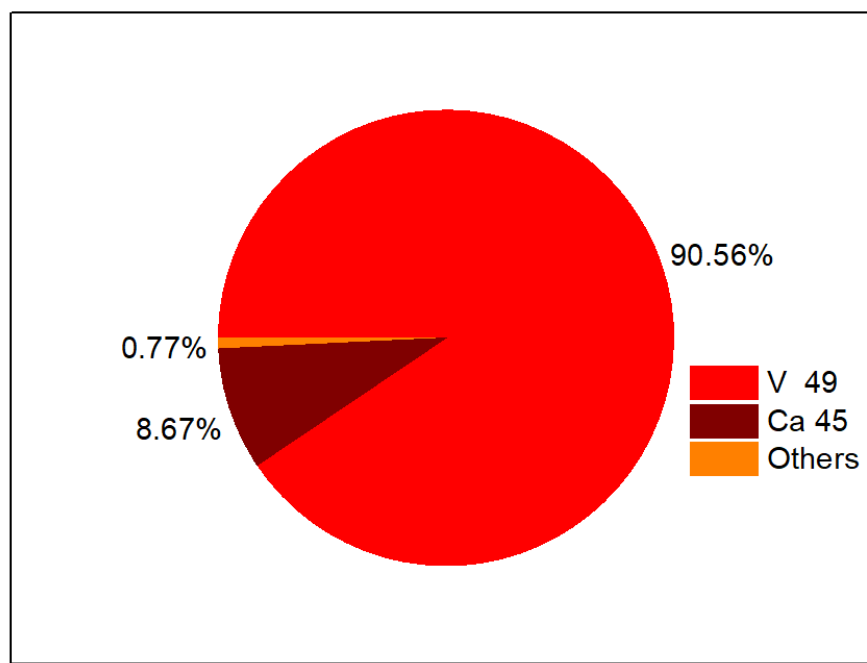


Figure 37: Main isotopes contribution on V4Cr4Ti vacuum vessel inner using FLiPb as coolant and blanket 2 years after the shutdown.

Total activity and decay heat after irradiation				
Parameter	1 day	30 day	1 year	2 year
Total activity [Bq/cm <sup>3</sup> ]	2.40970E+10	6.98871E+09	6.31692E+08	2.19963E+08
Total decay heat [W]	7.8844E+03	4.0388E+02	2.5778E+01	1.8577E+00
Decay beta [W]	5.1958E+02	3.4827E+01	4.3605E+00	0.78917E+00
Decay gamma [W]	7.3648E+03	3.6905E+02	2.1418E+01	1.0685E+00

Table 9: V4Cr4Ti vacuum vessel outer decay heat and specific activity as a function of time. Relative errors lower than 0.05%.

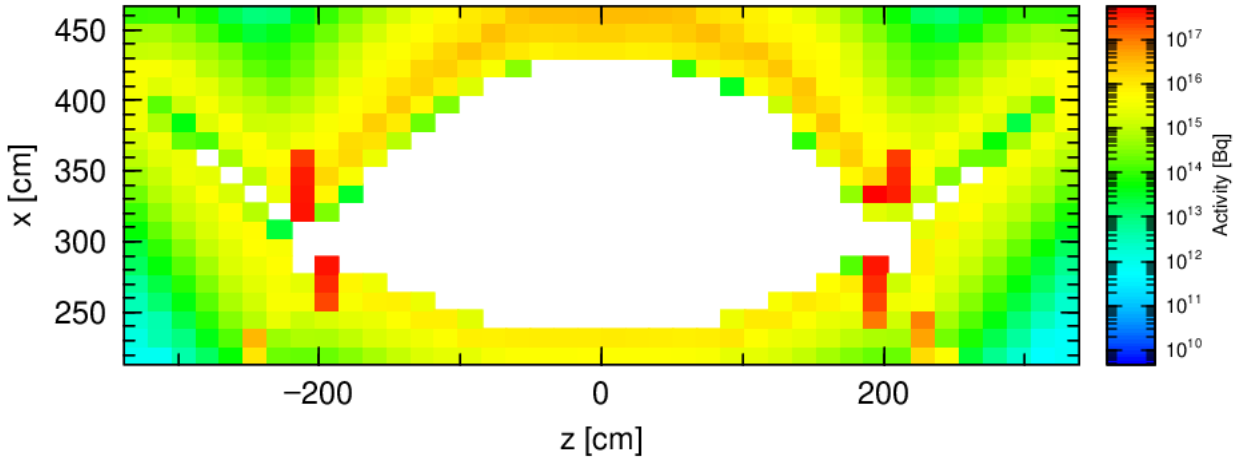


Figure 38: Activity [Bq] of V4Cr4Ti 1 day after irradiation

neutral fluxes are actually focused near the TF shielding material in the inboard side of the reactor, while materials are the same. This considerations suggest that the activity shown in Figure 38 may be to a numerical error due to an insufficient mesh size of the tally. Increasing the mesh size is cumbersome because it rises memory issues due to the huge amount of data (neutron spectra with 1968 energy bin structure, material chemical compositions and estimated density) required for each element of the mesh size as input for the activation analysis. In fact using a tetrahedral mesh importing only the vacuum vessel inner (in order to avoid memory issues), it can be seen from Figure 39 that the distribution is actually focused along the areas subjected to higher neutron fluxes.

Computing the dose rate taking as input the activity in Figure 38 the results of dose rate will be as well focused near the divertor region, as it shown in Figure 40; 1 day and 2 years after irradiation, respectively. It must be said that the major contribution on the dose rate, despite the high activity level of the molten salts, derives from the vacuum vessel material. For this reason, and in order to avoid numerical errors related to the geometrical shape and mesh size, the vacuum vessel has been modeled as toroidal shell to better represent the geometry shape and take into account of self-shielding. This approach reduced computational time and eliminate all the complexity related to this kind of computation while maintaining an accurate physical distribution of the dose rate. The toroidal shell major and inner radius have been set to fulfill the geometry volume of the vacuum vessel inner ( $1.09 \text{ m}^3$ ). Moreover one side present an higher radial thickness, in order to ensure that the inboard region of the vacuum vessel has higher dose rate as it expected from the distribution of the activity shown in Figure 39. Figures 43 and 44 shows the effective dose equivalent from 3 years to 10 years after the shutdown. Scale in Figure 44 is different to enhance legibility.

Time=0

Activity - (a.u.) Volume: 1 day after irradiation (1)

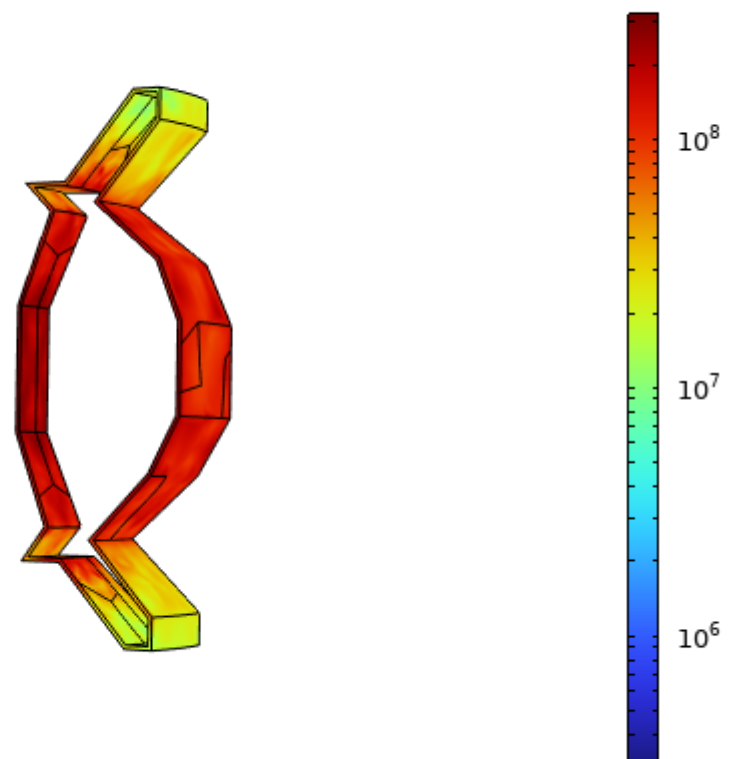


Figure 39: Activity 1 day after irradiation generated using a tetrahedral mesh to highlights the activity distribution along the vacuum vessel (a.u.)

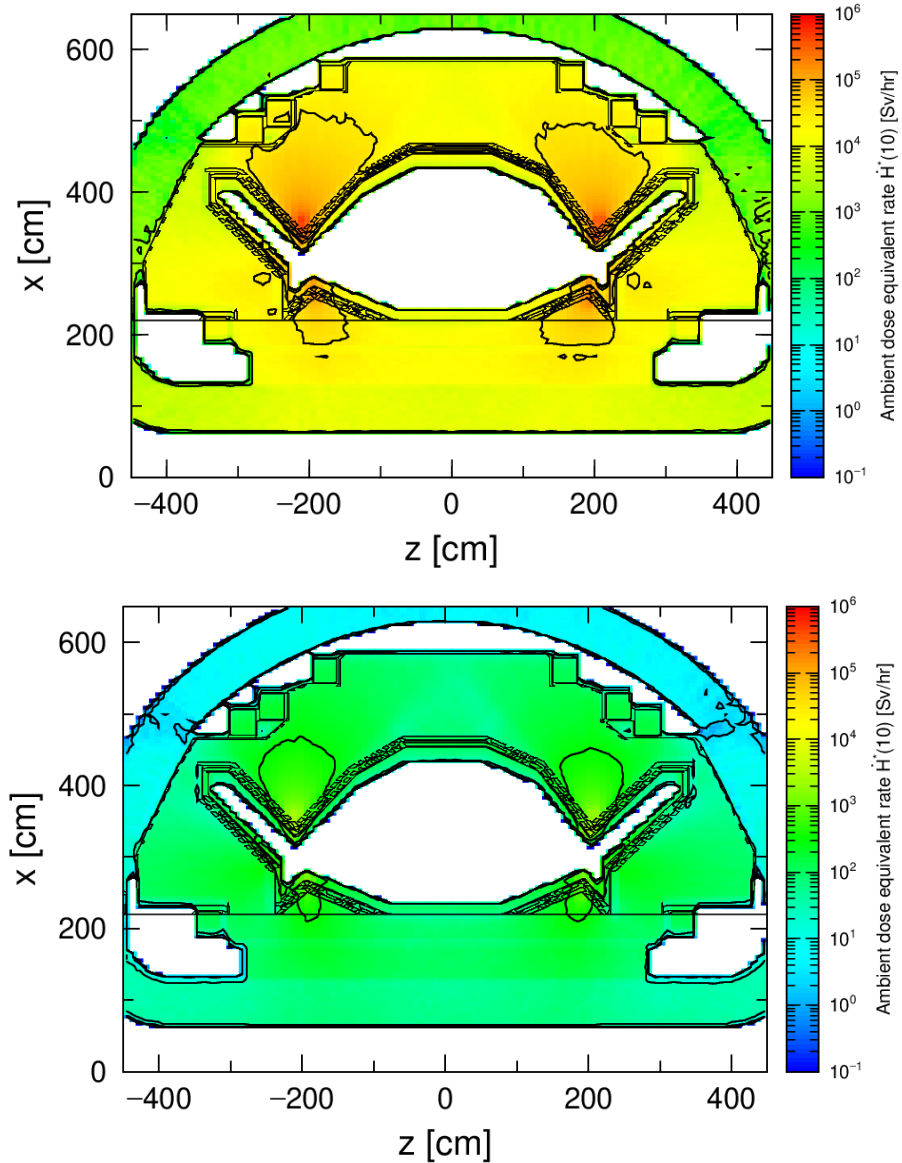


Figure 40: Ambient dose rate 1 day (up) and 2 years (down) after irradiation computed from the activity distribution as in Figure 38 using FLiBe as molten salt. Not appreciable difference have been observed using FLiPb. In this case also the surrounding materials are taken into account. Peaks near the divertor regions may be correlated to numerical errors due to the edges on the geometry and the mesh of the tally.

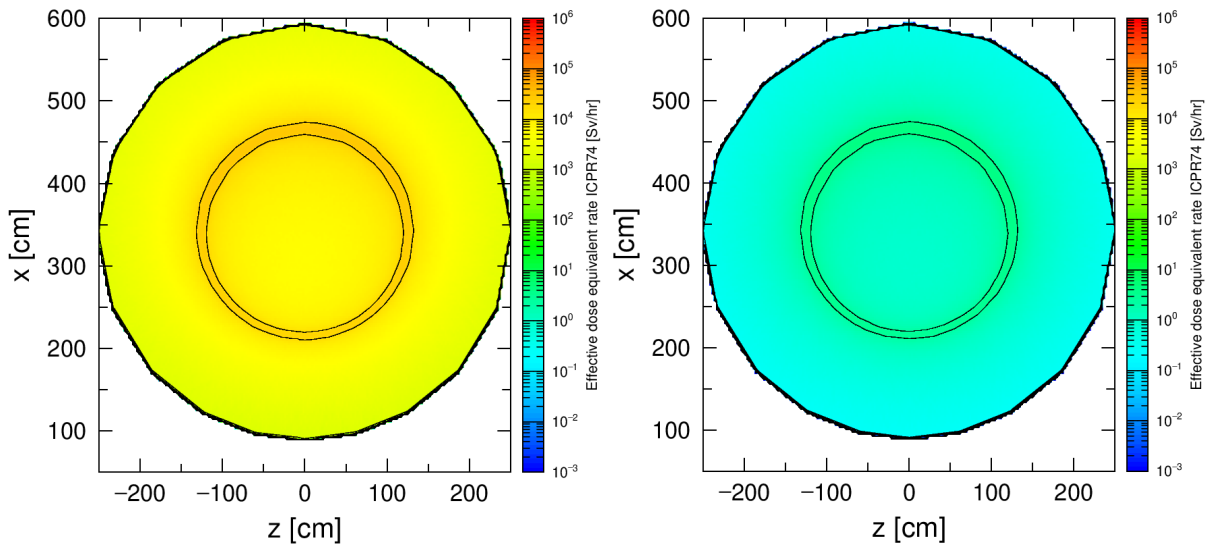


Figure 41: Effective dose equivalent 1 day (left) and 2 years (right) after the irradiation, vacuum vessel inner of V4Cr4Ti represented as toroidal shell to simulate the real geometry. Molten salt used in this configuration was FLiBe.

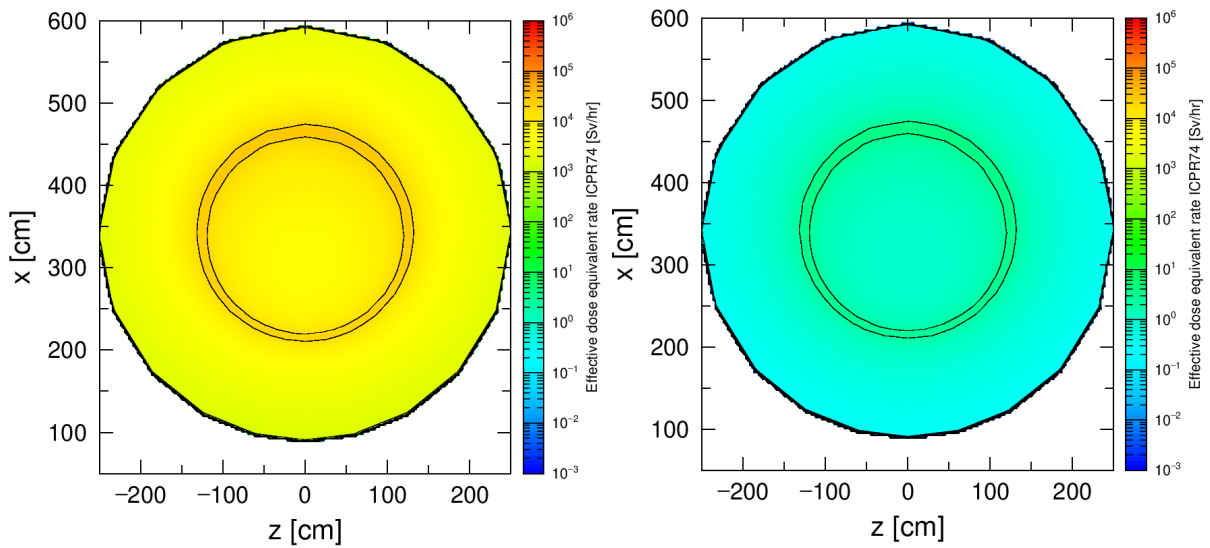


Figure 42: Effective dose equivalent 1 day (left) and 2 years (right) after the irradiation, vacuum vessel inner of V4Cr4Ti represented as toroidal shell to simulate the real geometry. Molten salt used in this configuration was FLiPb.

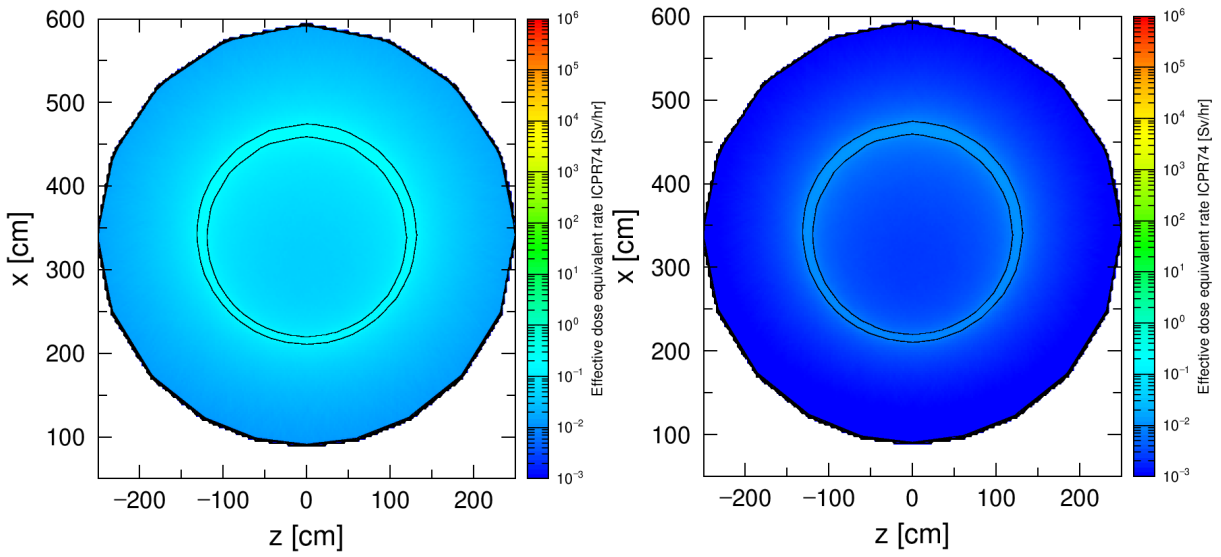


Figure 43: Effective dose equivalent 3 years (left) and 4 years (right) after the irradiation, vacuum vessel inner of V4Cr4Ti represented as toroidal shell to simulate the real geometry. Molten salt used in this configuration was FLiPb.

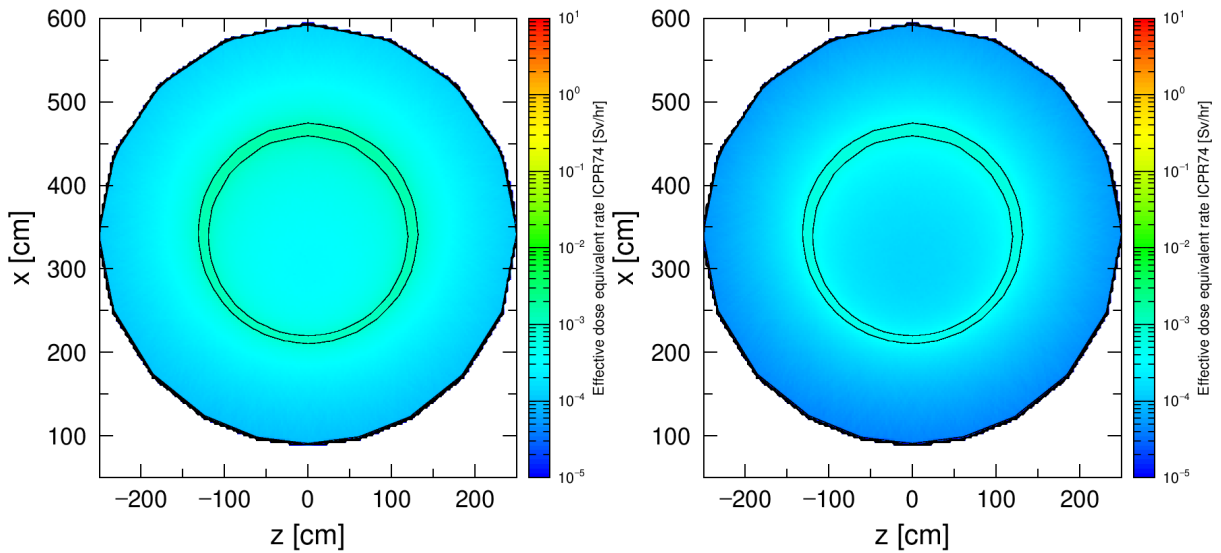


Figure 44: Effective dose equivalent 5 years (left) and 10 years (right) after the irradiation, vacuum vessel inner of V4Cr4Ti represented as toroidal shell to simulate the real geometry. Molten salt used in this configuration was FLiPb. Different scale with respect to the previous plots.

## Conclusion

In summary, the present work confirm that relation between TBR and neutron environment exist, as it was already observed in other work [42]. As expected it is true that materials with large cross section for thermal neutron capture coupled with efficient moderator of fast neutron reduce the neutron flux experienced from HTS magnets. Nevertheless materials with such efficient shielding characteristic will reduce the Tritium breeding ratio inside the blanket region. While generally consistent, this trend is not physically accurate.

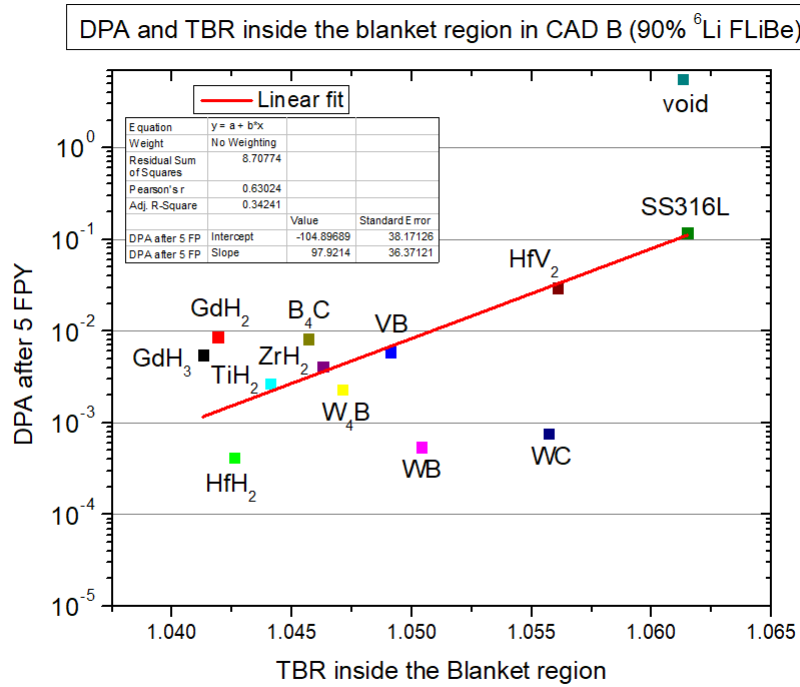


Figure 45: DPA after 5 FPY as a function of the TBR for all the analyzed materials

As it shows Figure 45 materials like gadolinium hydrides reduce more the TBR with respect to  $\text{HfH}_2$  while achieving higher neutron flux (and so spectra) when compared to  $\text{ZrH}_2$ . In fact since the shielding is outside of the blanket region, the impact on the TBR is due to scattering of thermal neutron. Gadolinium has similar properties in terms of neutron absorption if compared to Zr, but will not contribute to elastic scattering of thermal neutron, i.e. to the tritium production due to the presence of  ${}^6\text{Li}$  inside the blanket. Hafnium present better absorption but as well do not add back-scattering in the blanket. Conversely, vanadium and tungsten in these materials play the role of reflectors, contributing to TBR production. Instead boron and carbon are efficient moderator and so, while together do not exhibit a proper shielding capabilities, combined with W turns into the favorable choice for the TF shield component. Moreover, since the choice of the TF shield in commercial reactors not only depends from the neutron absorption but will be economic-driven [42], careful investigations are required in order to minimize the capital expenditures (CapEX) of the power plant. The uncertainties related to the manufacturing cost makes not trivial CapEX evaluation, which is out of the scope of this work, but for instance  $\text{HfH}_2$  and WB are expensive and so not suitable for commercial applications. Tungsten carbide may represent a good trade off between the baseline ( $\text{ZrH}_2$ ) and aforementioned materials. In fact WC present acceptable shielding properties and do not impact negligibly on TBR. While for some design configurations titanium hydride would be an interesting choice, since it may be even more cost-effective than  $\text{ZrH}_2$  while demonstrating slightly better performance, even if it will reduce more the TBR. Another interesting materials analyzed in this study regards the molten salt. In fact this work demonstrate that FLiPb does not increase neutron flux and DPA drastically. For instance deploying a shielding of tungsten carbide, displacement per atoms will still be lower than FLiBe highly enriched using  $\text{TiH}_2$ . The pros of using this FLiPb with respect to FLiBe as molten salt is a huge reduction of the capital cost. More precisely Pb has a cost of approximately 2 dollars per kilogram, while Be is really expensive. But

the real advantage is mainly due to the reduction of Li (reduced by a factor of 4.3) due to the different chemical composition. The main cost of FLiBe is correlated to the enrichment process, and a reduction of Li (and consequently of  $^6\text{Li}$ ) in FLiPb may be game changer parameter for the choice of the molten salt in commercial reactors. The drawback for this configuration is the reduction of the TBR and the weight of the blanket and salt coolant channel, which is double compared to FLiBe, due to the presence of lead. Moreover further investigations regarding the FLiPb physical properties are needed to evaluate the feasibility of such material under irradiation and corrosion environments.

Qualitative comparison of the molten salt FLiBe/FLiPb for the same reactor design					
Molten salt	Neutron flux	DPA	TBR	weight	cost
FLiBe (90% $^6\text{Li}$ )	↓	↓	↗	↓	↗
FLiPb (90% $^6\text{Li}$ )	↗	↗	↘	↗	↘

Table 10: Relation between FLiPb and FLiBe as molten salt in blanket and salt coolant channel.

Configurations with high enrichment  $^6\text{Li}$  levels are inherently favored due to their capacity to attenuate neutron flux, thereby diminishing the HTS radiation damage. Furthermore, such configurations also mitigate proliferation concerns, as it was observed in recent works [26]. Speaking of concerns the activity levels of the vacuum vessel and surrounding materials reveal that a cooling time greater than 2 years is required to reach the annual radiation dose limit. Further study on materials activation and irradiation time can emend the effective dose rate and must be taken into account during the design process. In fact fusion energy has the opportunity to distinguish itself by proactively addressing public concerns rather than reacting to them. This involves anticipating potential issues and engaging with the community early in the development process [39]. Achieving a social license is essential for the successful deployment of fusion energy technologies. Without public or community support, fusion energy may face significant barriers similar to those encountered by other technologies like fission reactors [39].

In the context of materials down-selection and design, optimization of material composition rather than extraction of scientific relations, machine learning (ML) algorithms is congenial [11]. Future works will delve to extend the results generated through all the simulations to build a dataset for ML training and validation. The selection of machine learning methodologies is contingent upon the volume and quality of input data as well as the specific objectives of the desired output. Varied types of ML algorithms may be employed commensurate with the scale and nature of the dataset and the complexity of the anticipated output. Taking into account the complex simulation setup and the time required to obtain an accurate dataset, my idea is to investigate computational modeling techniques based on reinforcement learning, such as agent-based modeling (ABM) and multi-agent systems (MAS). The application of ABMs in material design and complex product development has gained significant traction due to their ability to simulate and manage intricate systems. These models leverage autonomous, interacting agents to represent various components and their interactions within a system, providing valuable insights into the design process, risk assessment, and performance evaluation. Agent-based models are effective in simulating and optimizing complex systems, including those in material design, due to their ability to handle distributed and heterogeneous environments [34]. Moreover intelligent agents enhance CAD modeling by adapting to new situations and maintaining consistency across multiple views. These agents possess their own knowledge and can communicate and infer based on feature grammars, making CAD models more intelligent and adaptable [2]. In conclusion, a careful selection of machine learning methods may lead to an innovative and powerful tool able not only to predict all the computed output in this work, but also equipped to propose optimized nuclear fusion reactor design. By leveraging innovative ML techniques, even with limited datasets, we pave the way for more efficient, reliable, and ultimately scalable fusion energy solutions.

## References

- [1] A. Boozer et al. "What is a stellarator". In: *Physical review letters* (1998).
- [2] A. Fougères et al. "Intelligent agents for feature modelling in computer aided design". In: *J. Comput. Des. Eng.* (2018).
- [3] A. Knizhnik et al. "Interrelation of preparation conditions, morphology, chemical reactivity and homogeneity of ceramic YBCO". In: *Physica C: Superconductivity* (2003).
- [4] A. Sykes et al. "Compact fusion energy based on the spherical tokamak". In: *Nuclear Fusion* (2017).
- [5] A. Zylstra et al. "Experimental achievement and signatures of ignition at the national ignition facility." In: *Physical Review* (2022).
- [6] A.J. Creely et al. "SPARC as a platform to advance tokamak science". In: *Physics of Plasmas* (2023).
- [7] B. Kadomtsev et al. "Tokamaks". In: *Nuclear Fusion* (1990).
- [8] B. Sorbom et al. "ARC: A compact, high-field, fusion nuclear science facility and demonstration power plant with demountable magnets". In: *Fusion Engineering and Design* (2014).
- [9] Barry W. Brook et al. "Why nuclear energy is sustainable and has to be part of the energy mix". In: *Sustainable Materials and Technology* (2014).
- [10] C.G. Windsor et al. "Design of cemented tungsten carbide and boride-containing shields for a fusion power plant". In: *Nuclear Fusion* (2018).
- [11] D. Cohen-Tanugi et al. "Materials for Fusion Energy: Key Challenges and Guiding Principles for Developing Under High Design Uncertainty". In: *ArXiv* (2023).
- [12] D. Torsello et al. "Expected radiation environment and damage for YBCO tapes in compact fusion reactors". In: *Superconductor Science and Technology* (2023).
- [13] E. Alizadeh et al. "Tritium use in fusion reactors offers potential energy gain, but concerns about its safety and environmental impact must be addressed". In: *Journal of Fusion Energy* (2006).
- [14] F. Ledda et al. "3D Neutronic and Secondary Particles Analysis on YBa<sub>2</sub>Cu<sub>3</sub>O<sub>7</sub> Tapes for Compact Fusion Reactors". In: *IEEE TRANSACTIONS ON APPLIED SUPERCONDUCTIVITY* (2024).
- [15] F.A. Hernández et al. "First principles review of options for tritium breeder and neutron multiplier materials for breeding blankets in fusion reactors". In: *Fusion Engineering and Design* (2018).
- [16] G. Grieger et al. "Physics optimization of stellarators". In: *Physics of fluids. B, Plasma physics* (1992).
- [17] G. E. Sturdy et al. "The Gadolinium-Hydrogen System". In: *Contribution from thec University of California, Los Alamos Scientific Laboratory* (1955).
- [18] H. Rahman et al. "High yield fusion in a staged Z-pinch". In: *Journal of Plasma Physics* (2009).
- [19] H.N. Rantliff et al. "Modernization of the DCHAIN-PHITS activation code with new features and updated data libraries 2020". In: *Physics of Plasmas* (2020).
- [20] H.Y. Fu et al. "Fabrication using electron beam melting of a V-4Cr-4Ti alloy and its thermo-mechanical strengthening study". In: *Journal of Nuclear Materials* (2013).
- [21] J. Hammer et al. "High yield inertial confinement fusion target design for a z-pinch-driven hohlraum". In: *Physical review letters* (1999).
- [22] J. Miernik et al. "Z-Pinch fusion-based nuclear propulsion". In: *Acta Astronautica* (2013).
- [23] J. W. Bae et al. "ARC reactor neutronics multi-code validation". In: *Nucl. Fusion* 62 066016 (2022).
- [24] J. W. Bae et al. "Integral Analysis of the Effect of Material Dimension and Composition on Tokamak Neutronics". In: *Nucl. Fusion in press* (2024).
- [25] Jerry L. Holechek et al. "A Global Assessment: Can Renewable Energy Replace Fossil Fuels by 2050?" In: *Sustainability* (2022).
- [26] J.L. Ball et al. "Assessing the Risk of Proliferation via Fissile Material Breeding in ARC-class Fusion Reactors". In: *ArXiv* (2024).
- [27] K. Borowiec et al. "3D high-fidelity automated neutronics guided optimization of fusion blanket designs". In: *Fusion Engineering and Design* (2022).
- [28] K. Persson et al. "Materials Data on HfV2 (SG:227) by Materials Project". In: (2015).

- [29] M. Cuneo et al. "Double Z-pinch hohlraum drive with excellent temperature balance for symmetric inertial confinement fusion capsule implosions." In: *Physical review letters* (2002).
- [30] M. ITO et al. "Thermomechanical Properties of Hafnium Hydride". In: *Journal of NUCLEAR SCIENCE and TECHNOLOGY* (2010).
- [31] M.A.N. Giménez et al. "Tungsten Carbide compact primary shielding for Small Medium Reactor". In: *Annual of Nuclear Energy* (2018).
- [32] M.C. Osborn et al. "Neutron irradiation effects on the density, tensile properties and microstructural changes in Hi-Nicalone and Sylramice SiC fibers". In: *Journal of Nuclear Materials* (1998).
- [33] M.R. Gilbert et al. "Energy spectra of primary knock-on atoms under neutron irradiation". In: *Journal of Nuclear Materials* (2015).
- [34] N. Li et al. "Risk assessment model based on multi-agent systems for complex product design". In: *Informations System Frontiers* (2015).
- [35] R. Bouillon et al. "Molten salt breeding blanket: Investigations and proposals of pre-conceptual design options for testing in DEMO". In: *Fusion Engineering and Design* (2021).
- [36] R. Craxton et al. "Direct-drive inertial confinement fusion: A review". In: *Physics of Plasmas* (2015).
- [37] R. Penzhorn et al. "Technology and component development for a closed tritium cycle". In: *Fusion Engineering and Design* (1991).
- [38] R. G. Clemmer et al. "Fusion reactor designs must incorporate tritium breeding systems and strict environmental control to ensure safe and efficient use of this essential element in near-term thermonuclear reactors." In: *Nuclear Engineering and Design* (1976).
- [39] S. Hoeld et al. "Achieving a social license for fusion energy". In: *Physics of Plasmas* (2022).
- [40] S. Meschini et al. "Review of commercial nuclear fusion projects". In: *frontiers* (2023).
- [41] S. O'hira et al. "Radiochemical characteristics of tritium to be considered in fusion reactor facility design". In: *Journal of Radioanalytical and Nuclear Chemistry* (2007).
- [42] S. Segantin et al. "Preliminary investigation of neutron shielding compounds for ARC-class tokamaks". In: *Fusion Engineering and Design* (2022).
- [43] Shen Qu et al. "Study on Multiphysics Coupling and Automatic Neutronic Optimization for Solid Tritium Breeding Blanket of Fusion Reactor". In: *Energies* (2021).
- [44] T. Nagasaka et al. "Progress in flibe corrosion study toward material research loop and advanced liquid breeder blanket". In: *NIFS-925, National Inst. for Fusion Science* (2008).
- [45] T. Sato et al. "Features of Particle and Heavy Ion Transport code System (PHITS) version 3.02". In: *JOURNAL OF NUCLEAR SCIENCE AND TECHNOLOGY* (2018).
- [46] Uri Shumlak et al. "Z-pinch fusion". In: *Journal of Applied Physics* (2020).
- [47] V. Moiseenko et al. "Research on stellarator-mirror fission-fusion hybrid". In: *Plasma Physics and Controlled Fusion* (2014).
- [48] Vladimir S. Arutyunov et al. "Energy resources of the 21st century: problems and forecasts. Can renewable energy sources replace fossil fuels". In: *Russian Chemical Reviews* (2017).
- [49] Yoichi Watanabe et al. "Determination of the Required Tritium Breeding Ratio for the Next Fusion Experimental Reactor". In: *Fusion technology* (1989).
- [50] Zachary Hartwig et al. "The SPARC Toroidal Field Model Coil Program". In: *IEEE TRANSACTIONS ON APPLIED SUPERCONDUCTIVITY* (2024).
- [51] P. Andreo. "Monte Carlo techniques in medical radiation physics." In: *Physics in medicine and biology* (1991).
- [52] J. Bardeen, L. Cooper, and J. Schrieffer. "Theory of superconductivity". In: *Il Nuovo Cimento* (1955-1965) (1957).
- [53] "Compendium of Material Composition Data for Radiation Transport Modeling". In: *Pacific Northwest National Laboratory* (2021).
- [54] Charles W. Forsberg. "Sustainability by combining nuclear, fossil, and renewable energy sources". In: *Progress in Nuclear Energy* (2009).

- [55] C. Giannone. "Monte Carlo Calculations in Nuclear Medicine: Applications in Diagnostic Imaging". In: *Physiological Measurement* (1999).
- [56] "Hafnium hydride (HfH<sub>2</sub>) properties". In: *AZO materials* (2004).
- [57] Z. Hartwig. "Fusion Energy". In: *Nuclear Science and Engineering Course 22.061* (2024).
- [58] L. Landau and V. Ginzburg, "On the theory of superconductivity". In: *Zh. Eksp. Teor. Fiz.* (1950).
- [59] W. Meissner and R. Ochsenfeld. "Ein neuer effekt bei eintritt der supraleitfähigkeit". In: *Naturwissenschaften* (1933).
- [60] A. Muller and J. G. Bednorz. "Possible High T<sub>c</sub> Superconductivity in the Ba-La-Cu-O System". In: *Zeitschrift fur Physik B Condensed Matter* (1986).
- [61] H. Onnes. "Investigations into the properties of substances at low temperatures, which have led, amongst other things, to the preparation of liquid helium". In: (2013).
- [62] R. Scanlan, A. Malozemoff, and D. Larbalestier. "Superconducting materials for large scale applications". In: *Proceedings of the IEEE* (2004).
- [63] B. L. Sjenitzer and J. E. Hoogenboom. "Dynamic Monte Carlo Method for Nuclear Reactor Kinetics Calculations". In: *Nuclear Science and Engineering* (2013).
- [64] "Tungsten Boride WB". In: *Stanford Advanced Material* (2024).
- [65] "Vanadium Boride VB". In: *AMERICAN ELEMENTS, THE MATERIALS SCIENCE MANUFACTURER* (2024).
- [66] Yican Wu et al. "CAD-based Monte Carlo Program for Integrated Simulation of Nuclear System SuperMC". In: (2014).
- [67] H. Zaidi. "Relevance of accurate Monte Carlo modeling in nuclear medical imaging." In: *Medical physics* (1999).

## Appendix A

### ICRP74 conversion coefficient

Conversion coefficient gamma flux( $\Phi$ ) to dose ( $E$ )	
Photon energy [MeV]	$E/\Phi$ [ $pSv \cdot cm^2$ ]
1.0000E-03	4.8518E-03
5.0000E-03	2.4259E-02
1.0000E-02	4.8518E-02
1.5000E-02	1.2542E-01
2.0000E-02	2.0496E-01
3.0000E-02	2.9994E-01
4.0000E-02	3.3805E-01
5.0000E-02	3.5724E-01
6.0000E-02	3.7801E-01
8.0000E-02	4.3993E-01
1.0000E-01	5.1717E-01
1.5000E-01	7.5234E-01
2.0000E-01	1.0041E+00
3.0000E-01	1.5083E+00
4.0000E-01	1.9958E+00
5.0000E-01	2.4657E+00
6.0000E-01	2.9082E+00
8.0000E-01	3.7269E+00
1.0000E+00	4.5800E+00
3.0000E+00	9.9200E+00
5.0000E+00	1.3400E+01
1.0000E+01	2.0800E+01
1.5000E+01	2.8400E+01
2.0000E+01	3.3500E+01
5.0000E+01	5.2600E+01
1.0000E+02	6.6100E+01
5.0000E+02	8.5400E+01
1.0000E+03	9.1300E+01
1.0000E+04	1.0500E+02

Table 11: Conversion coefficient used to compute the effective dose equivalent

## Appendix B

The following subsections contains the PKA spectra on the most critical irradiated HTS region for different design configuration. The subsection title resume the material used for the simulation followed by the thickness layer in cm. Blanket tank is made of the same structural material with thickness 3 cm. The salt coolant channel chemical composition can be deduced from the name as well. For instance FLiBe means FLiBe natural composition, FLiBe90 means FLiBe with 90% enrichment of  $^{6}\text{Li}$ .

**W 0.5 - V4Cr4Ti 5 - FLiBe90 2 - Be 1 - V4Cr4Ti 5**

### PKA spectrum on YBCO with void shield

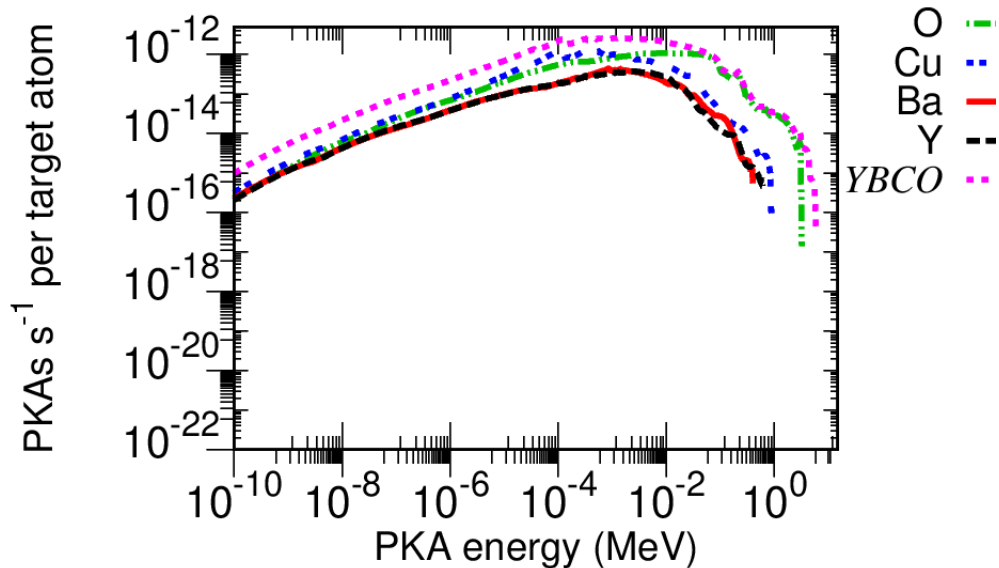


Figure 46: PKA spectra on the most critical HTS region

## PKA spectrum on YBCO with ZrH<sub>2</sub> shield

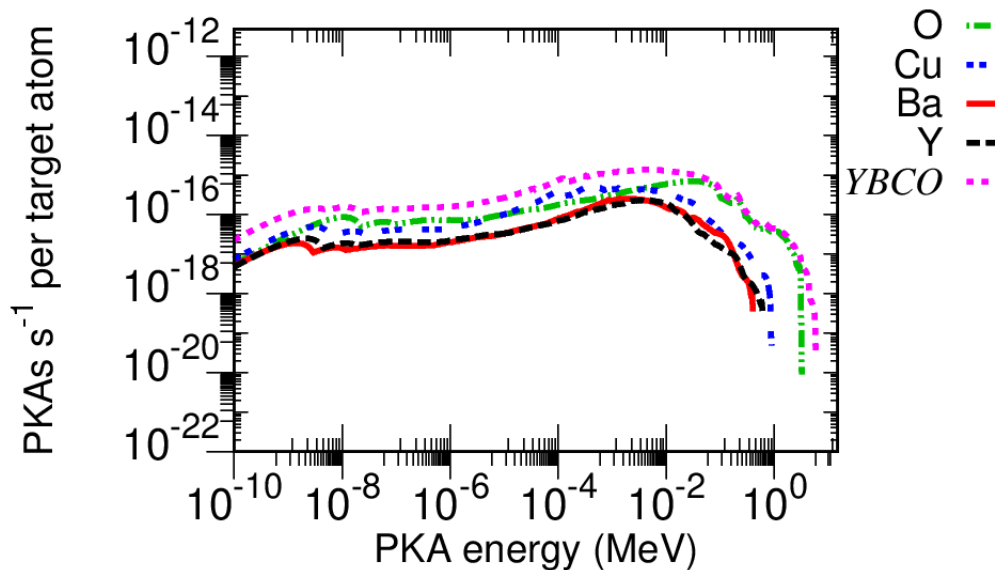


Figure 47: PKA spectra on the most critical HTS region with 51 cm shield

## PKA spectrum on YBCO with TiH<sub>2</sub> shield

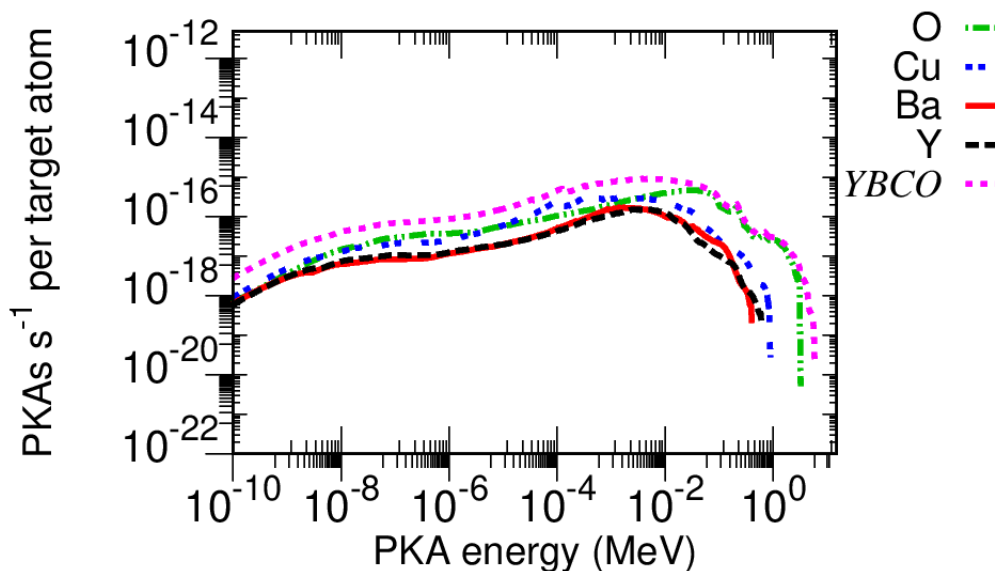


Figure 48: PKA spectra on the most critical HTS region with 51 cm shield

## PKA spectrum on YBCO with WB shield

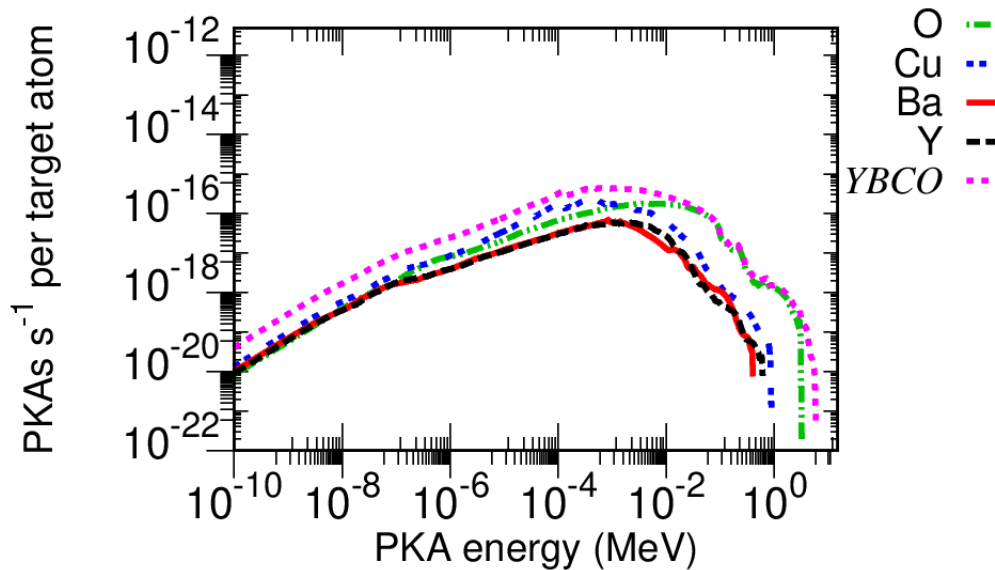


Figure 49: PKA spectra on the most critical HTS region with 51 cm shield

## PKA spectrum on YBCO with WC shield

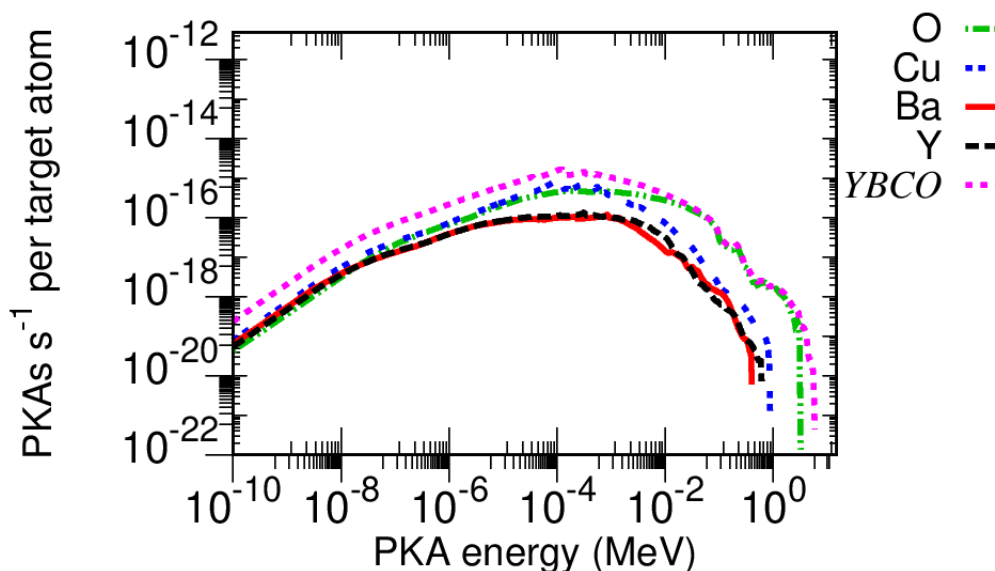


Figure 50: PKA spectra on the most critical HTS region with 51 cm shield

## PKA spectrum on YBCO with WB4 shield

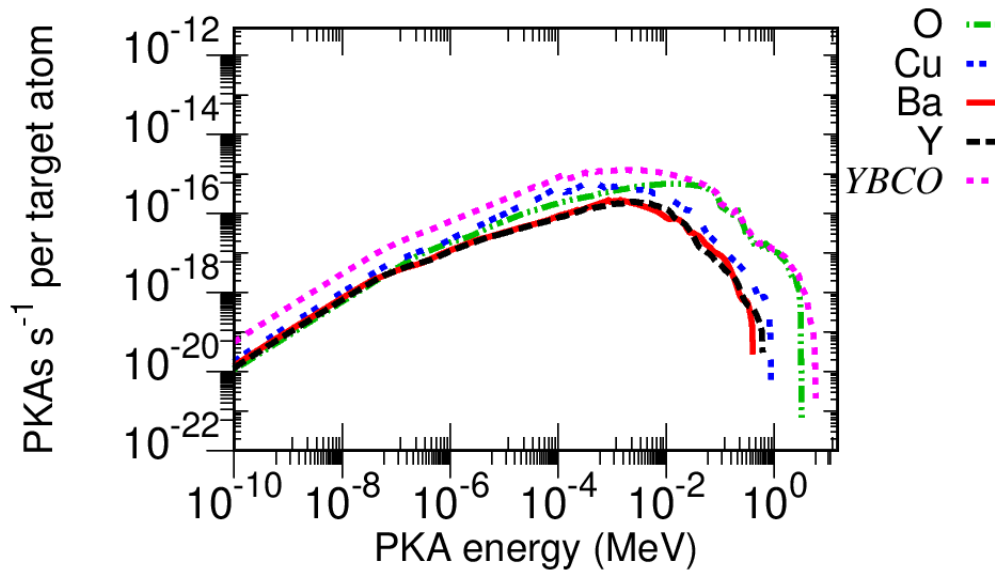


Figure 51: PKA spectra on the most critical HTS region with 51 cm shield

## PKA spectrum on YBCO with HfH<sub>2</sub> shield

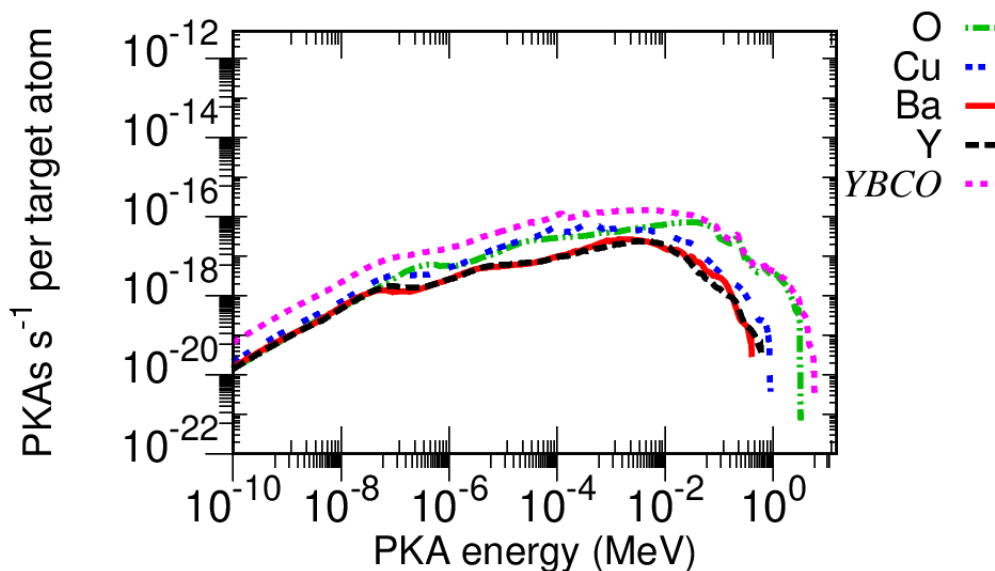


Figure 52: PKA spectra on the most critical HTS region with 51 cm shield

## PKA spectrum on YBCO with $\text{HfV}_2$ shield

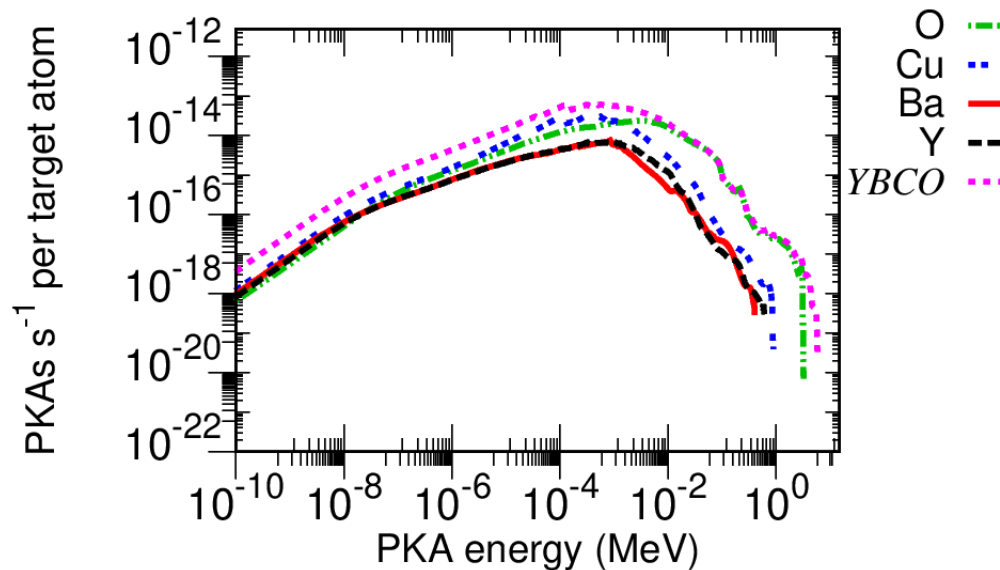


Figure 53: PKA spectra on the most critical HTS region with 51 cm shield

## PKA spectrum on YBCO with SS316L shield

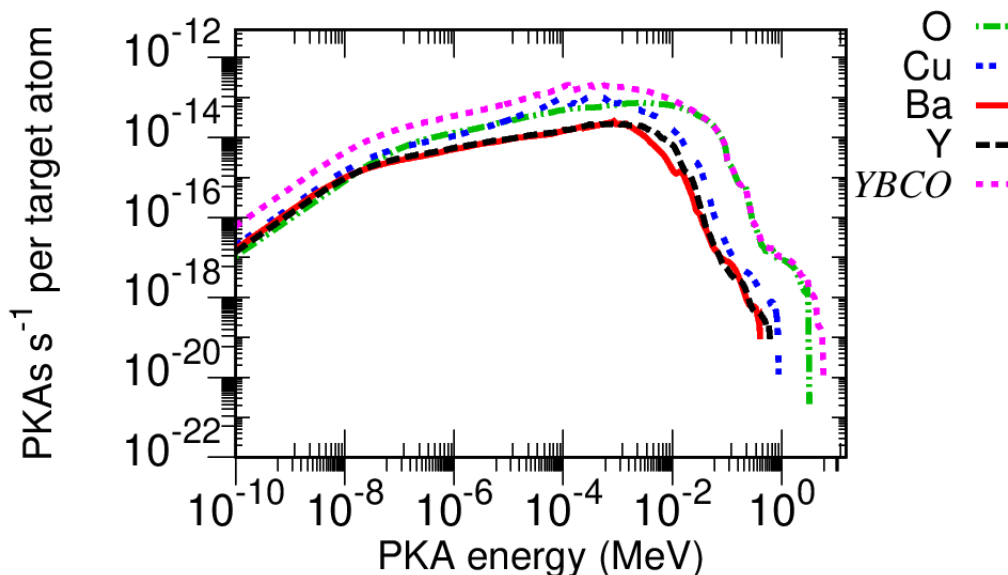


Figure 54: PKA spectra on the most critical HTS region with 51 cm shield

## PKA spectrum on YBCO with VB shield

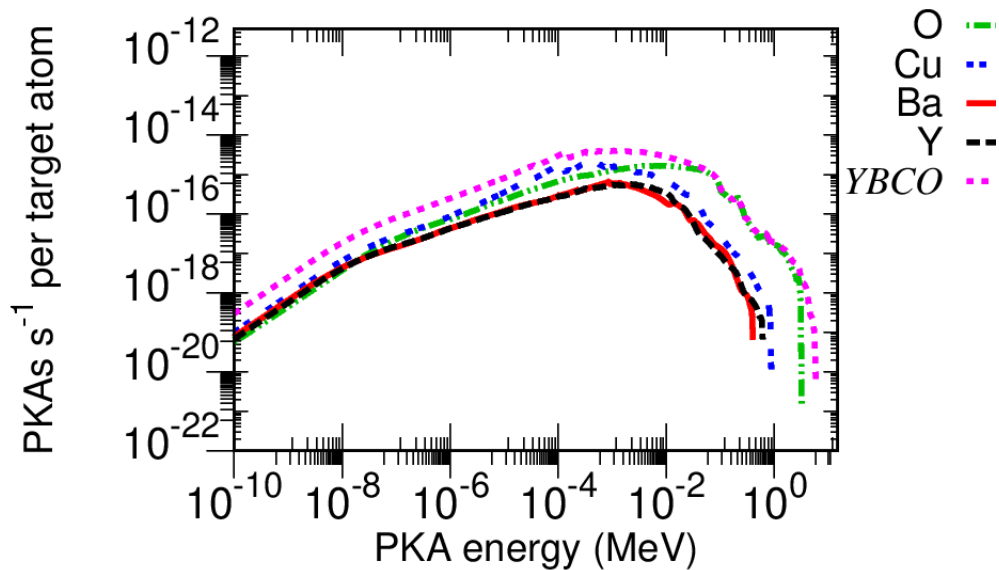


Figure 55: PKA spectra on the most critical HTS region with 51 cm shield

## PKA spectrum on YBCO with $\text{GdH}_3$ shield

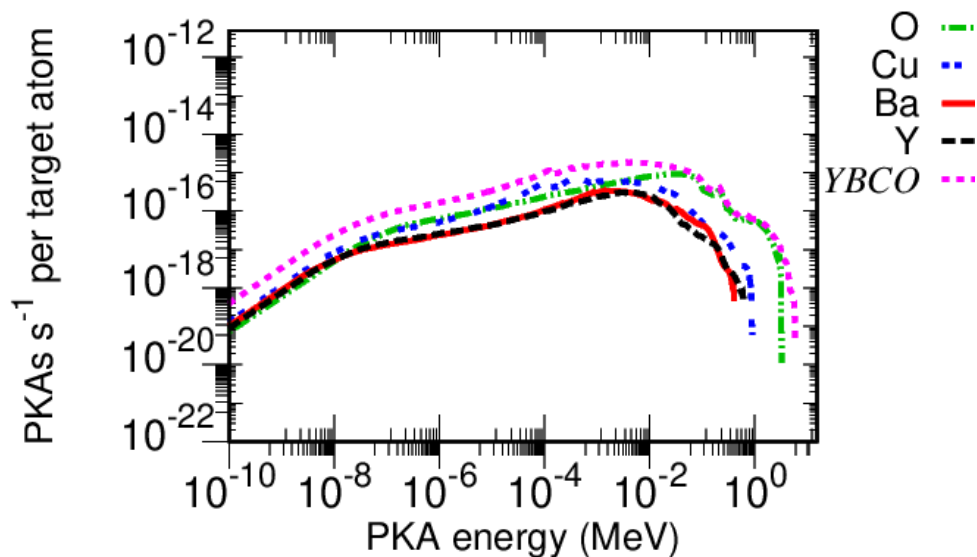


Figure 56: PKA spectra on the most critical HTS region with 51 cm shield

## PKA spectrum on YBCO with $\text{GdH}_2$ shield

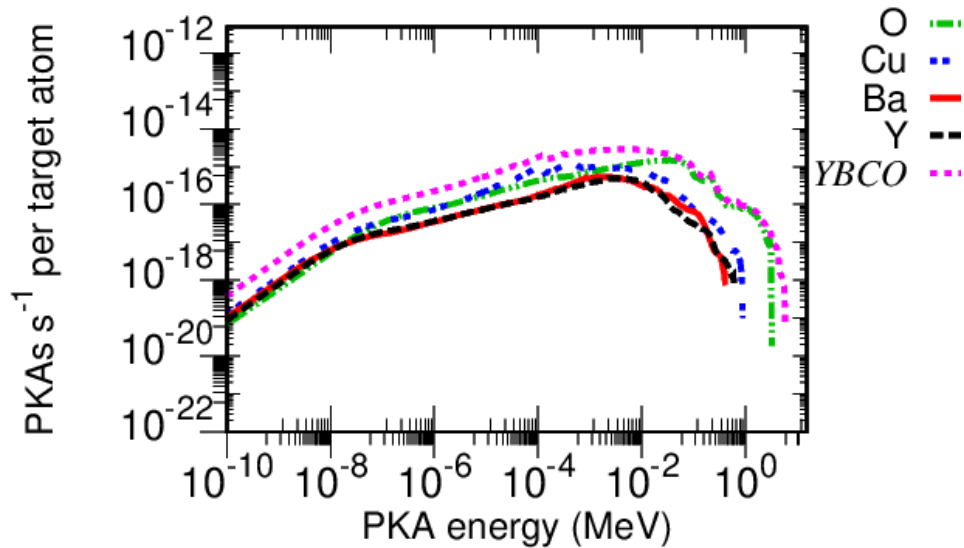


Figure 57: PKA spectra on the most critical HTS region with 51 cm shield

## PKA spectrum on YBCO with $\text{B}_4\text{C}$ shield

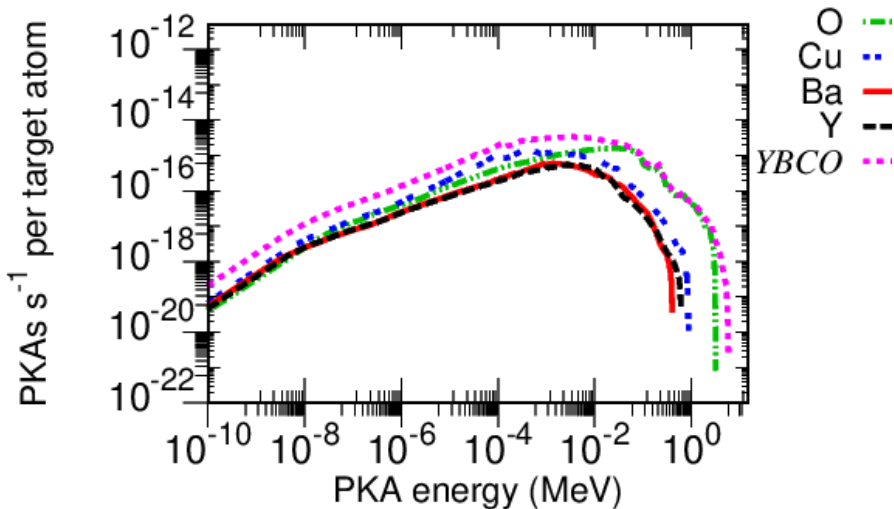


Figure 58: PKA spectra on the most critical HTS region with 51 cm shield

### PKA spectrum on YBCO with void shield

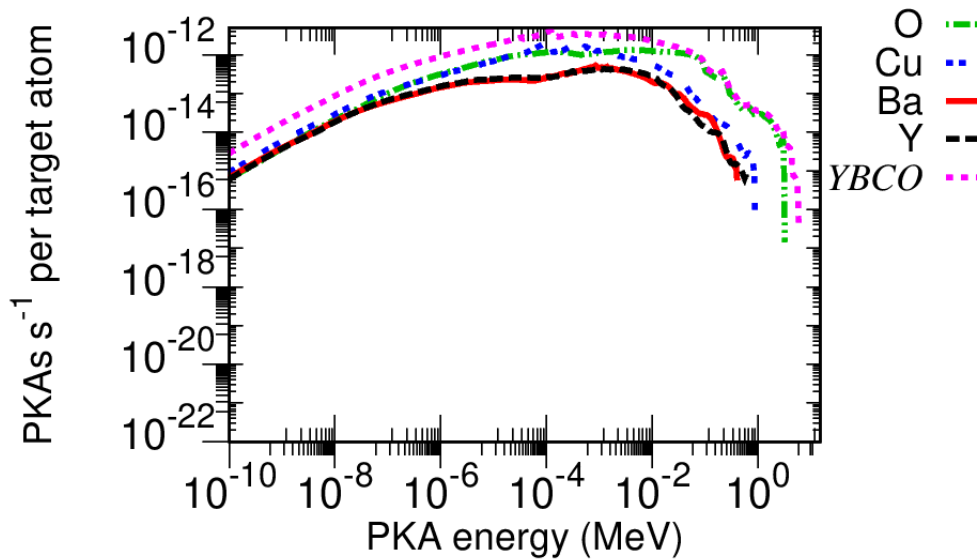


Figure 59: PKA spectra on the most critical HTS region

### PKA spectrum on YBCO with ZrH2 shield

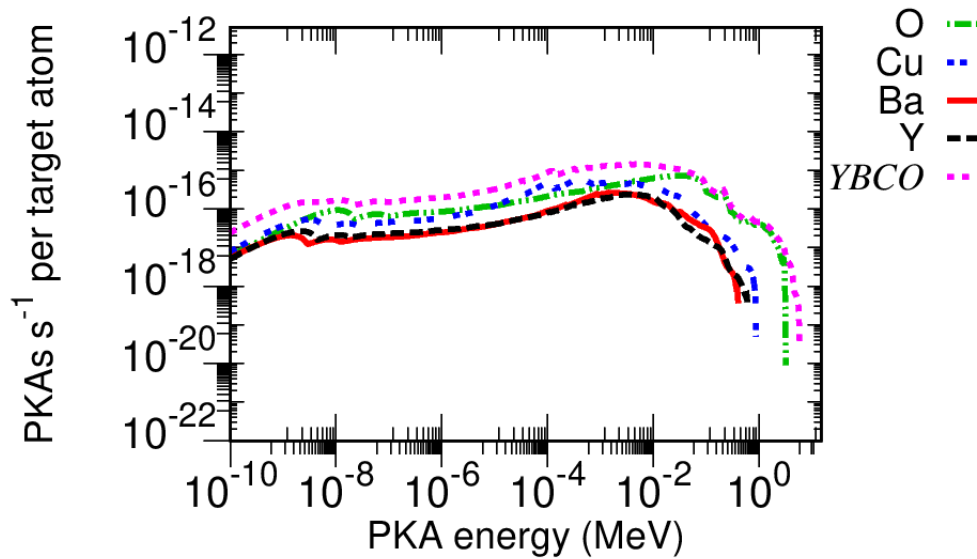


Figure 60: PKA spectra on the most critical HTS region with 51 cm shield

## PKA spectrum on YBCO with $\text{TiH}_2$ shield

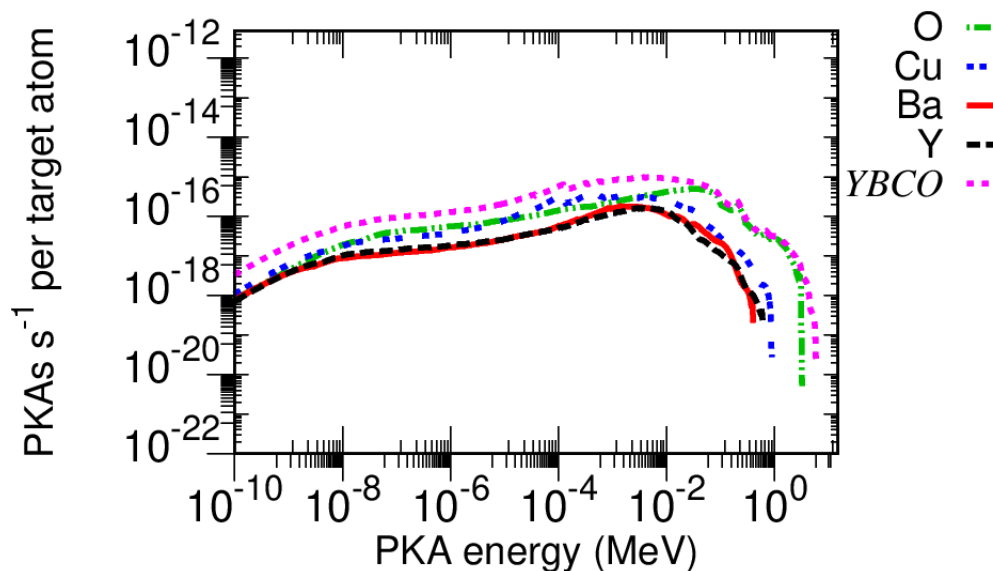


Figure 61: PKA spectra on the most critical HTS region with 51 cm shield

## PKA spectrum on YBCO with WB shield

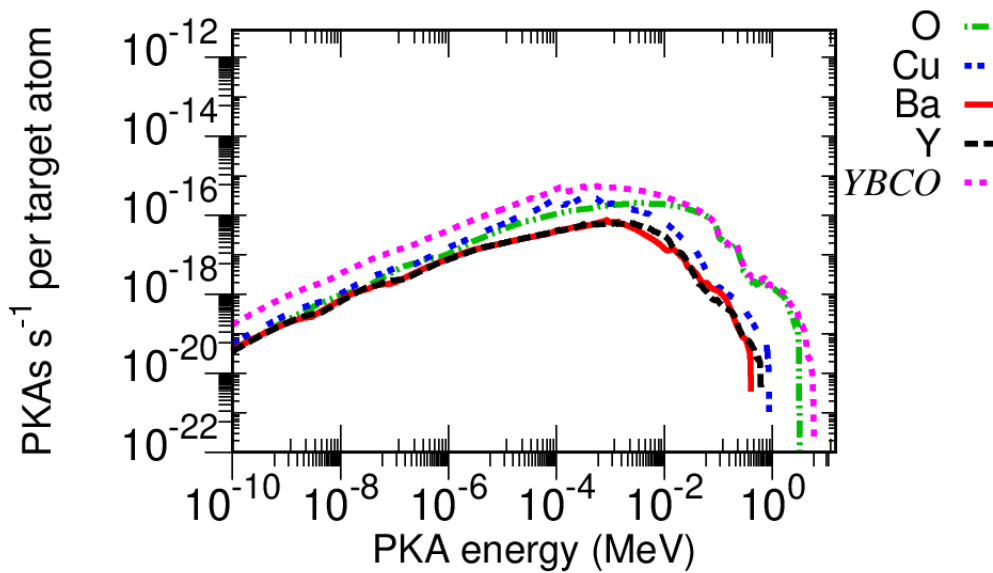


Figure 62: PKA spectra on the most critical HTS region with 51 cm shield

## PKA spectrum on YBCO with WC shield

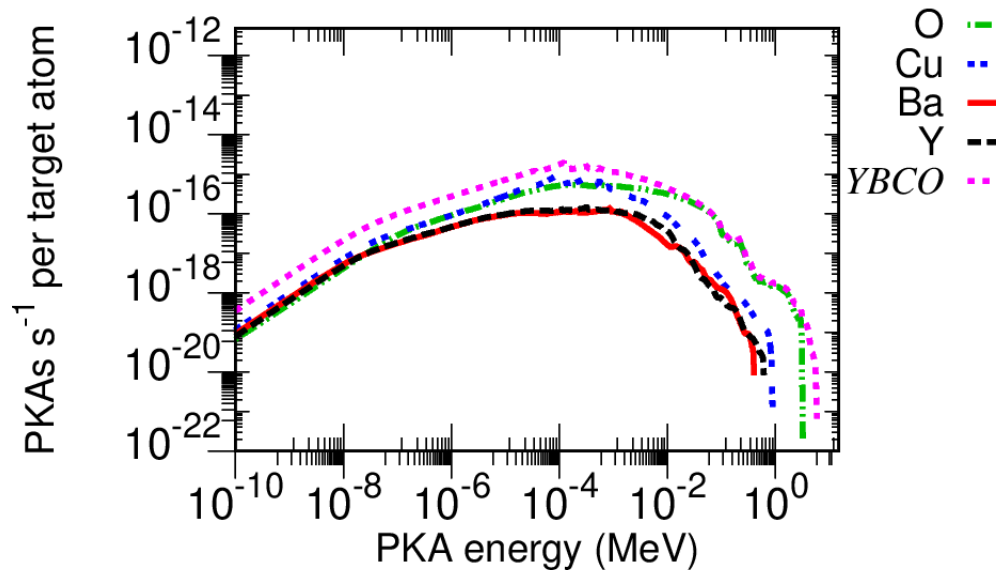


Figure 63: PKA spectra on the most critical HTS region with 51 cm shield

## PKA spectrum on YBCO with WB<sub>4</sub> shield

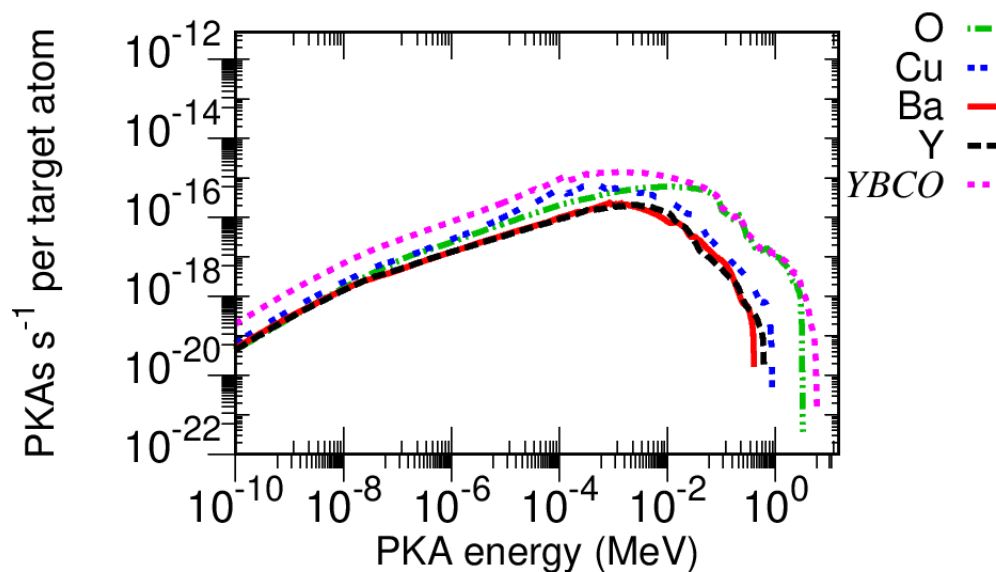


Figure 64: PKA spectra on the most critical HTS region with 51 cm shield

## PKA spectrum on YBCO with $\text{HfH}_2$ shield

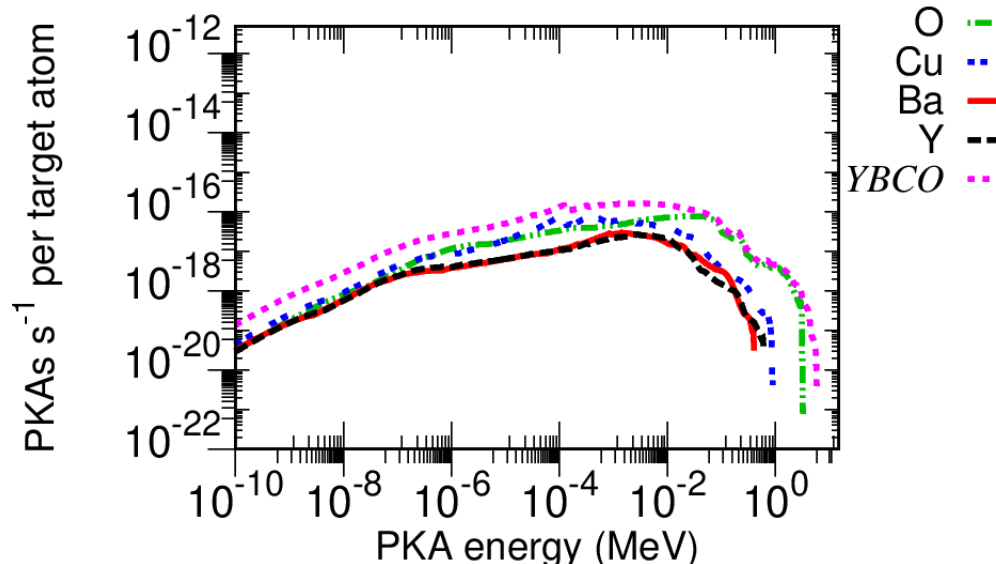


Figure 65: PKA spectra on the most critical HTS region with 51 cm shield

## PKA spectrum on YBCO with $\text{HfV}_2$ shield

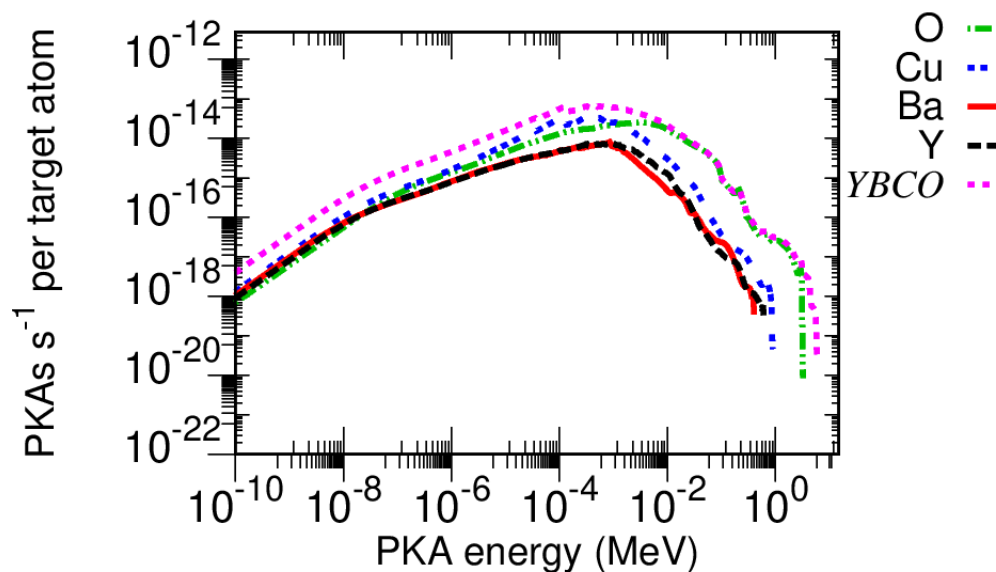


Figure 66: PKA spectra on the most critical HTS region with 51 cm shield

## PKA spectrum on YBCO with SS316L shield

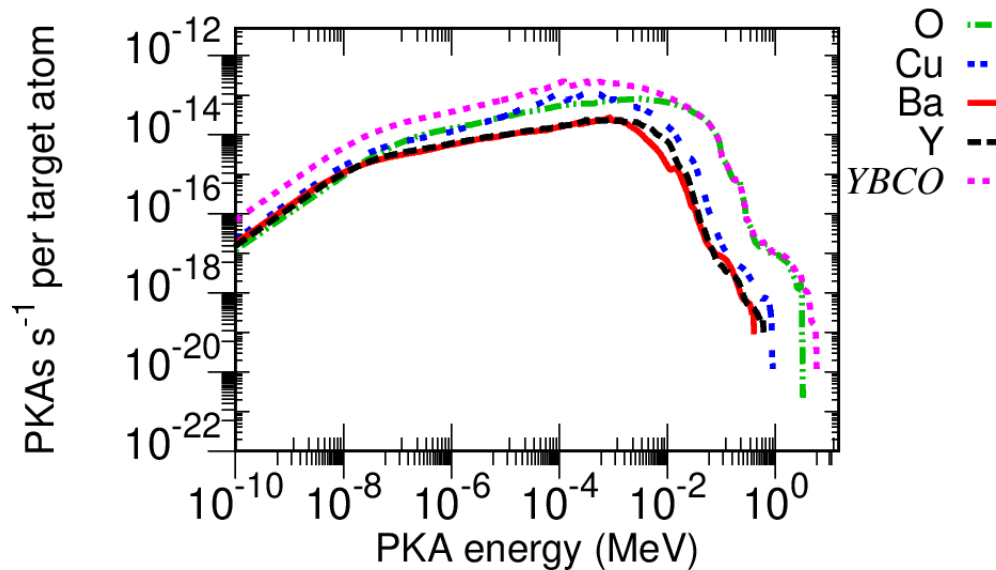


Figure 67: PKA spectra on the most critical HTS region with 51 cm shield

## PKA spectrum on YBCO with VB shield

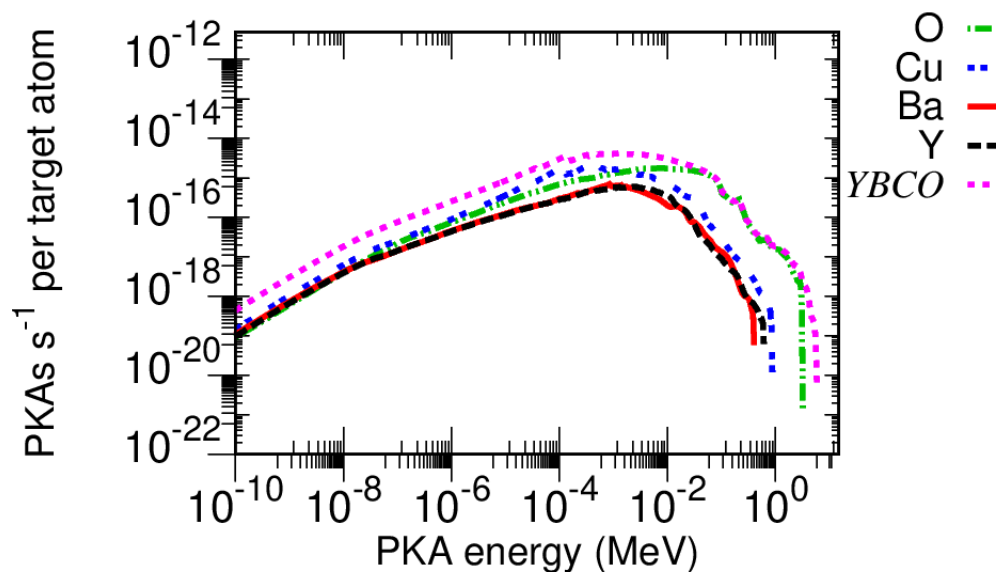


Figure 68: PKA spectra on the most critical HTS region with 51 cm shield

## PKA spectrum on YBCO with $\text{GdH}_3$ shield

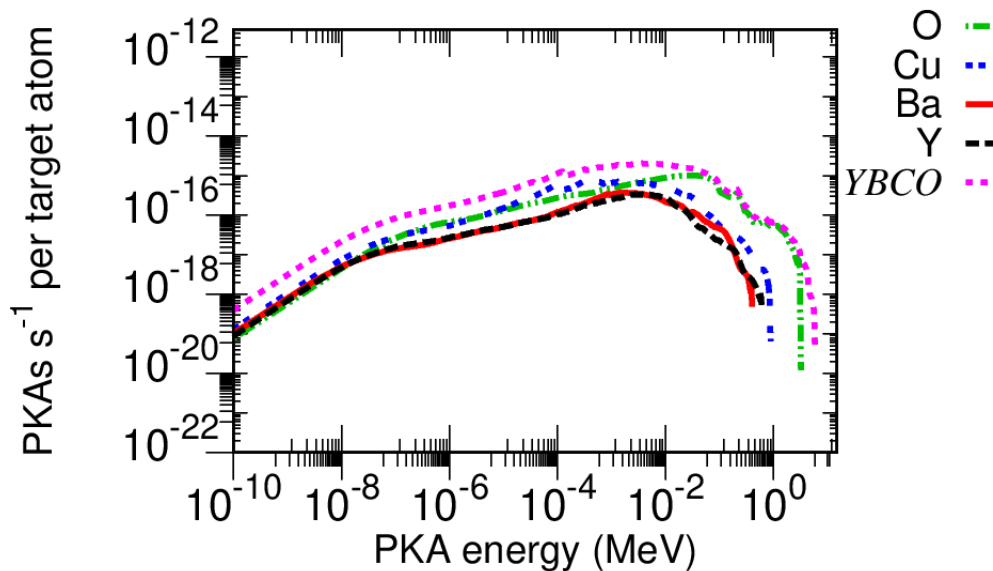


Figure 69: PKA spectra on the most critical HTS region with 51 cm shield

## PKA spectrum on YBCO with $\text{GdH}_2$ shield

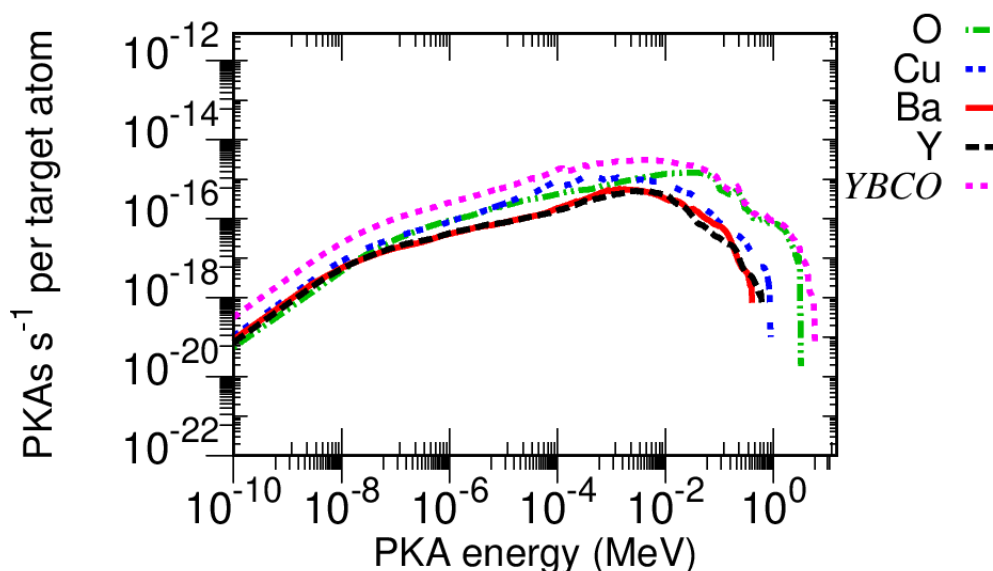


Figure 70: PKA spectra on the most critical HTS region with 51 cm shield

## PKA spectrum on YBCO with $B_4C$ shield

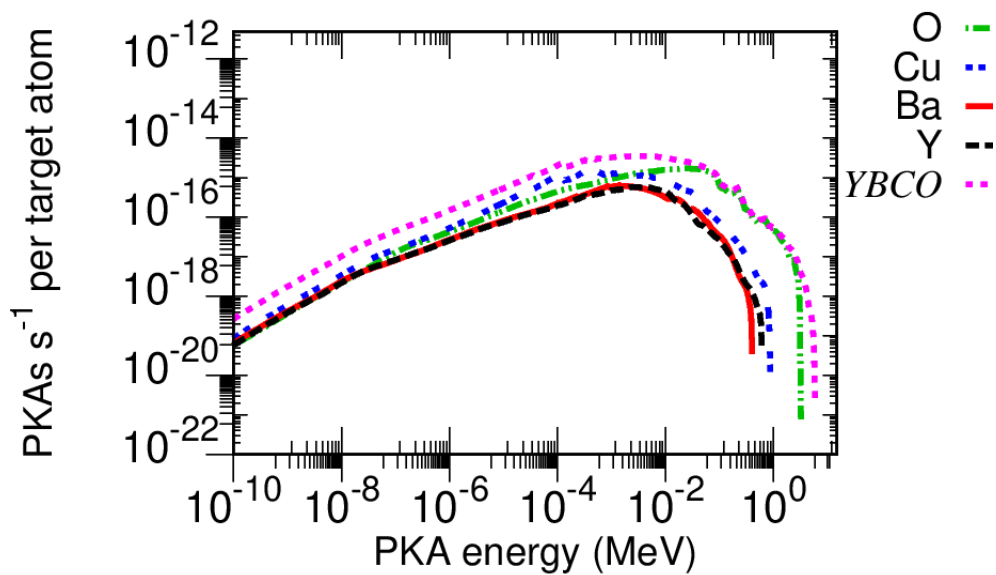


Figure 71: PKA spectra on the most critical HTS region with 51 cm shield

### PKA spectrum on YBCO with void shield

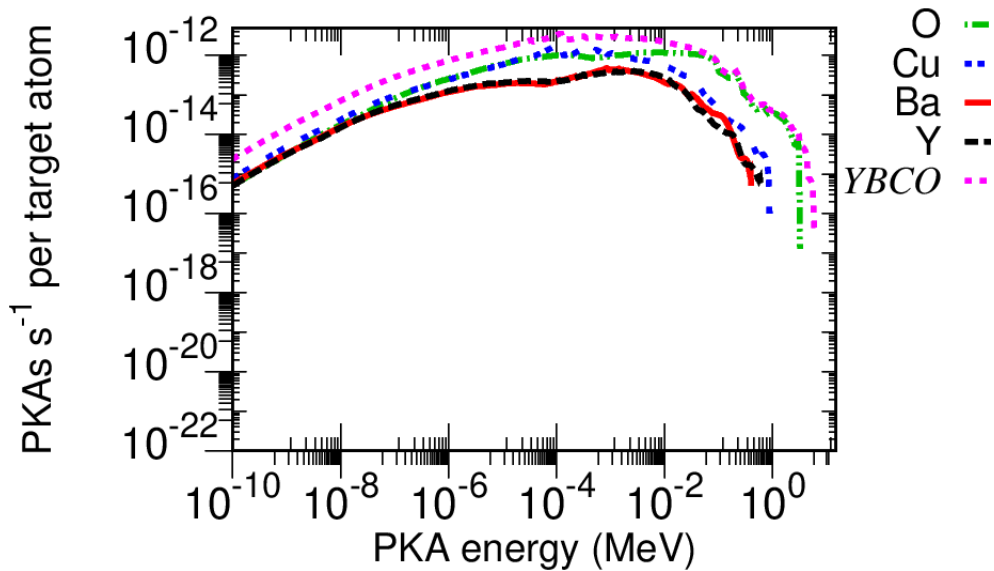


Figure 72: PKA spectra on the most critical HTS region

### PKA spectrum on YBCO with ZrH<sub>2</sub> shield

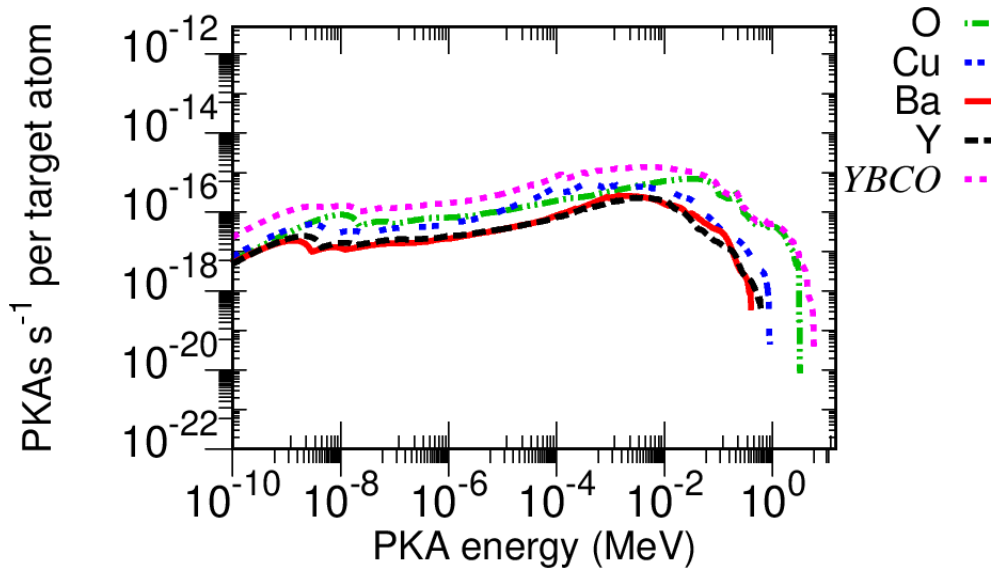


Figure 73: PKA spectra on the most critical HTS region with 51 cm shield

## PKA spectrum on YBCO with $\text{TiH}_2$ shield

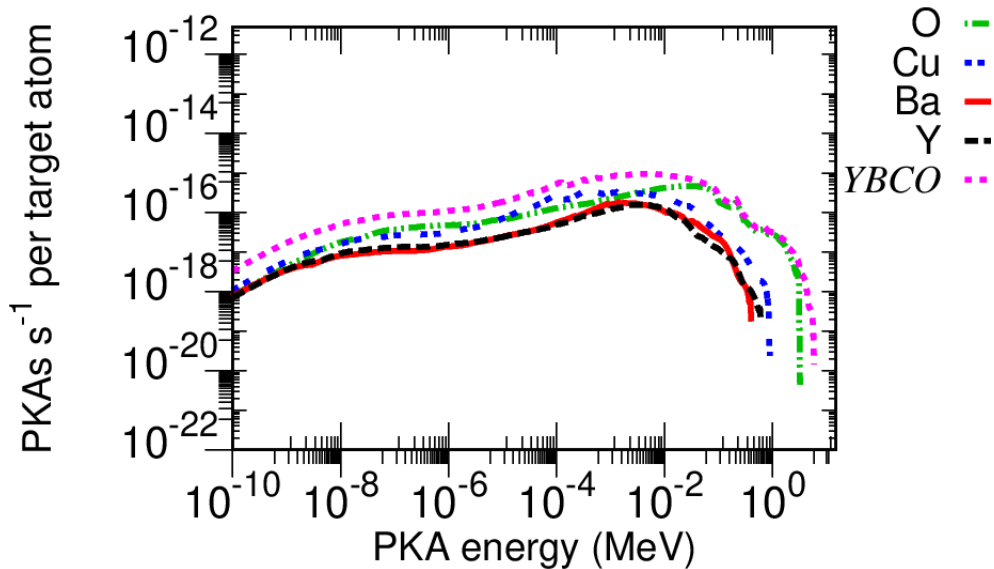


Figure 74: PKA spectra on the most critical HTS region with 51 cm shield

## PKA spectrum on YBCO with WB shield

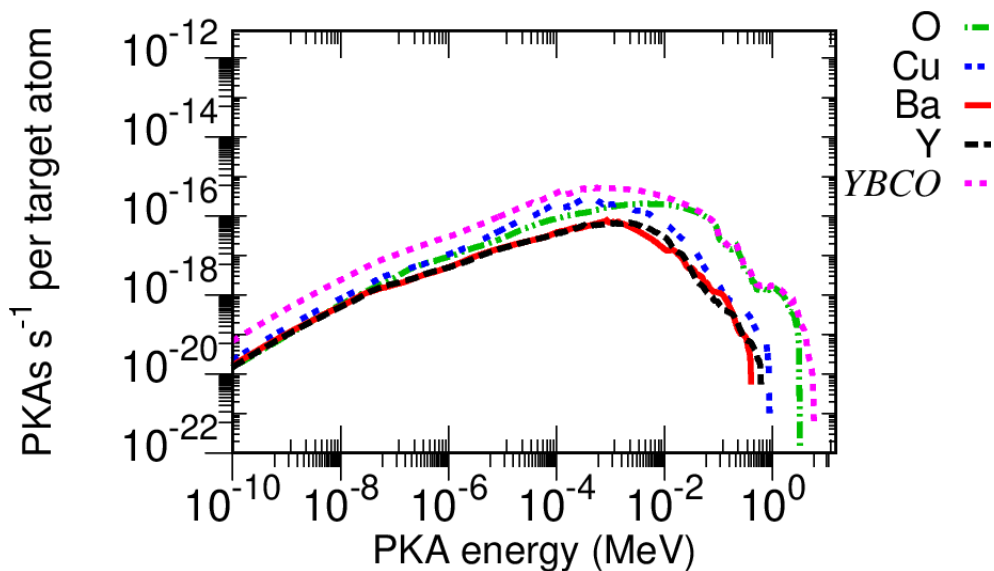


Figure 75: PKA spectra on the most critical HTS region with 51 cm shield

## PKA spectrum on YBCO with WC shield

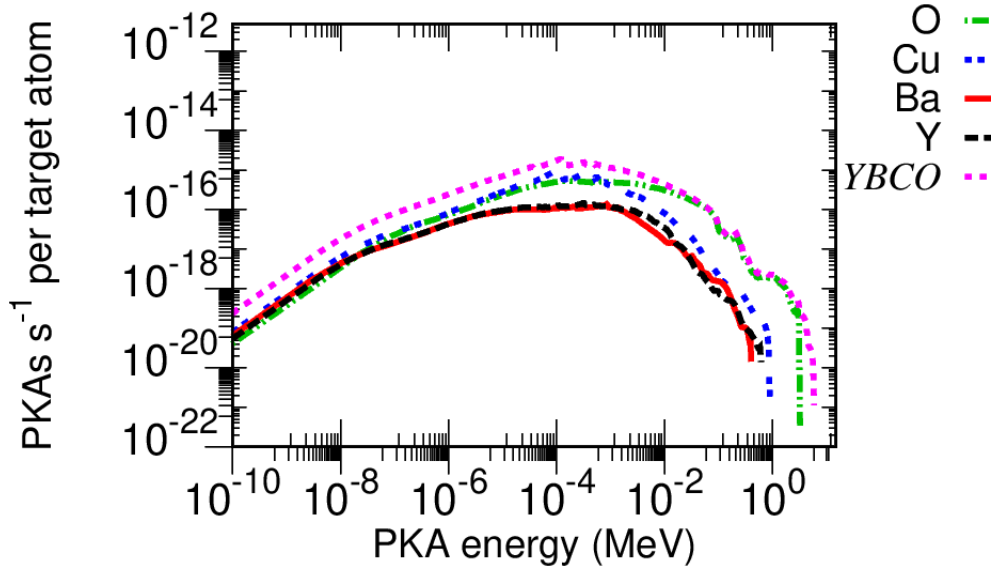


Figure 76: PKA spectra on the most critical HTS region with 51 cm shield

## PKA spectrum on YBCO with WB<sub>4</sub> shield

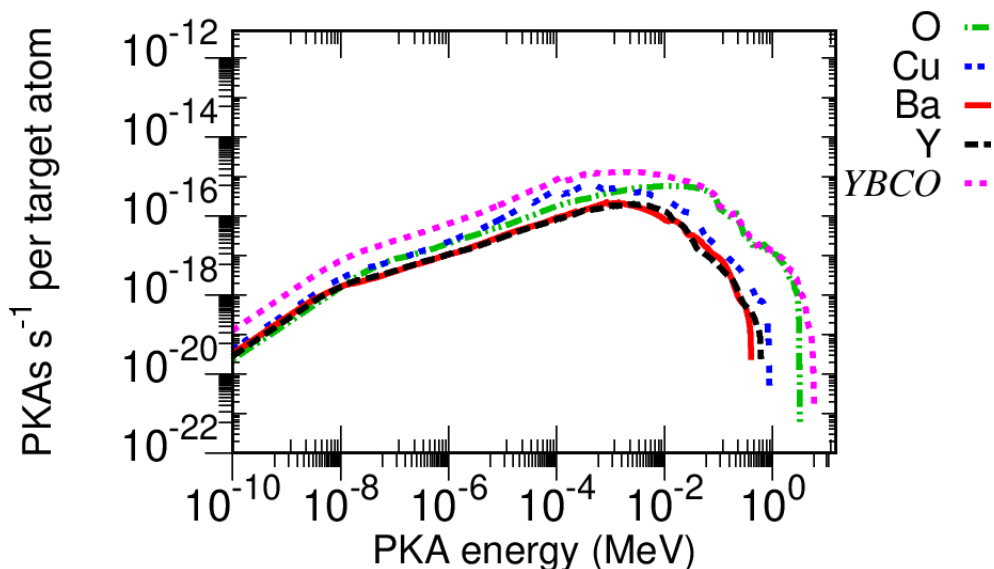


Figure 77: PKA spectra on the most critical HTS region with 51 cm shield

## PKA spectrum on YBCO with HfH<sub>2</sub> shield

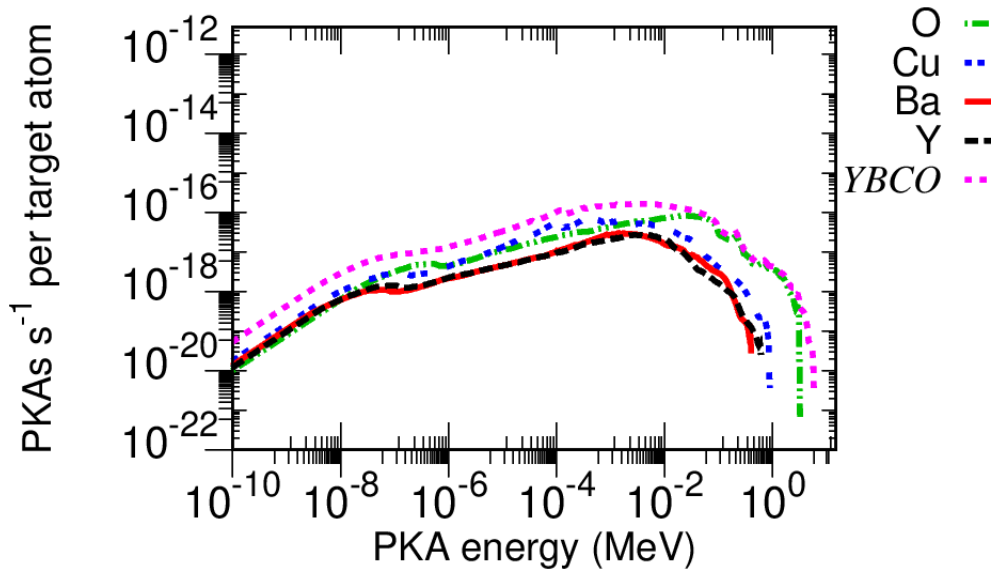


Figure 78: PKA spectra on the most critical HTS region with 51 cm shield

## PKA spectrum on YBCO with HfV<sub>2</sub> shield

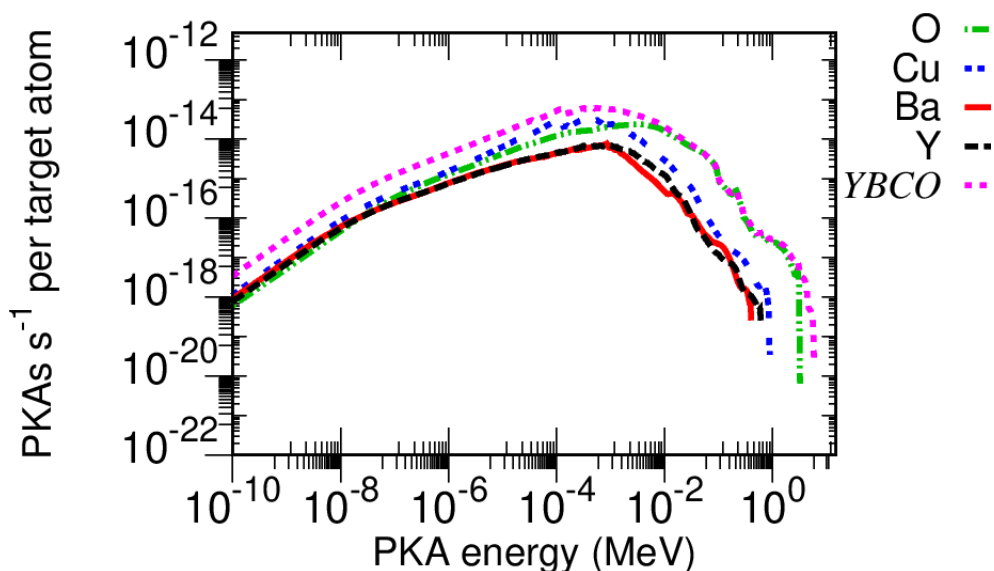


Figure 79: PKA spectra on the most critical HTS region with 51 cm shield

## PKA spectrum on YBCO with SS316L shield

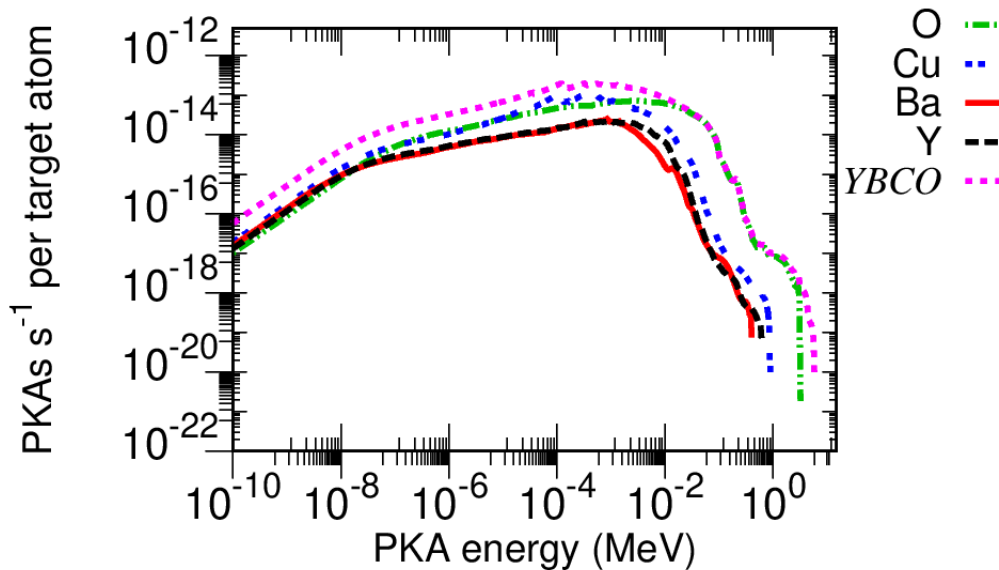


Figure 80: PKA spectra on the most critical HTS region with 51 cm shield

## PKA spectrum on YBCO with VB shield

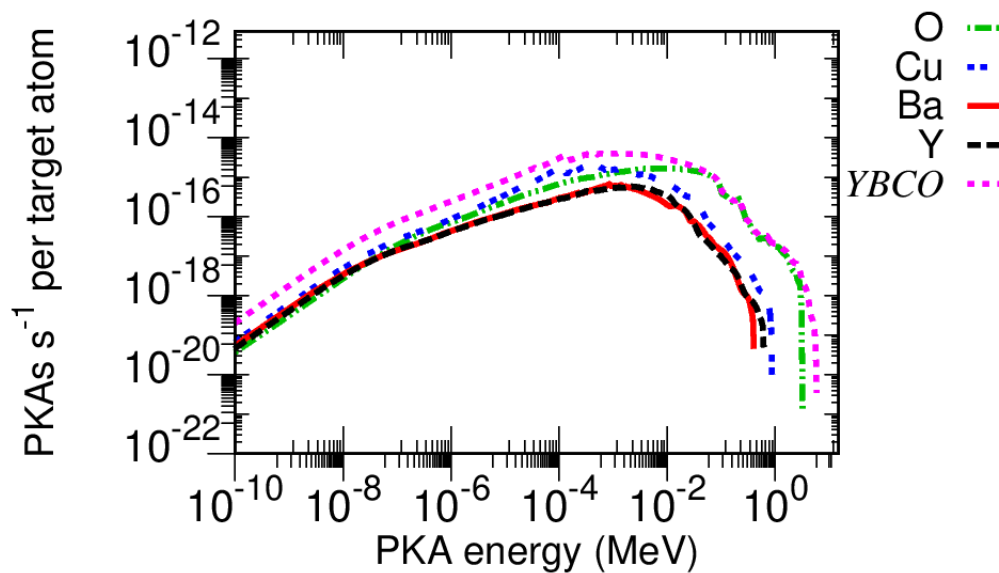


Figure 81: PKA spectra on the most critical HTS region with 51 cm shield

## PKA spectrum on YBCO with $\text{GdH}_3$ shield

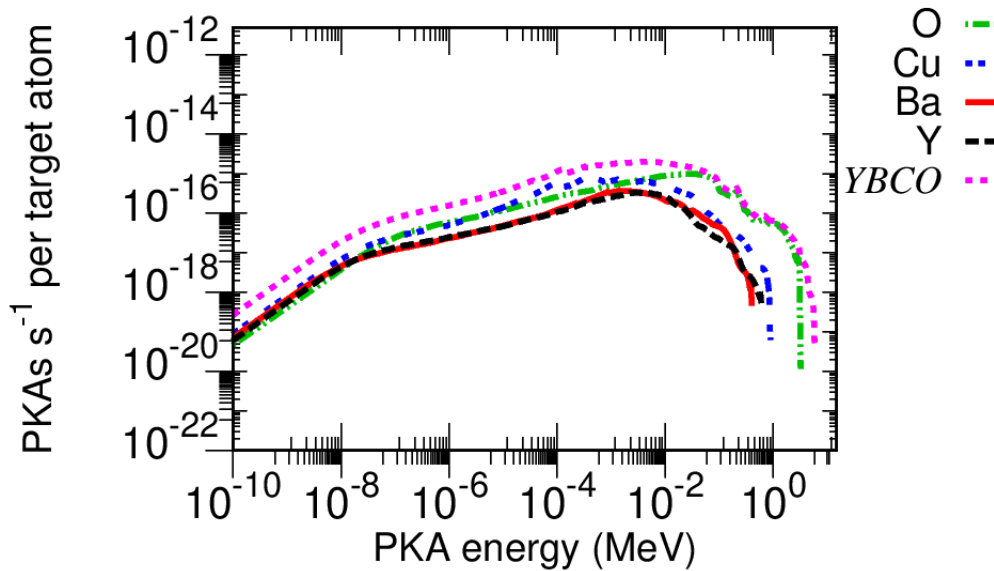


Figure 82: PKA spectra on the most critical HTS region with 51 cm shield

## PKA spectrum on YBCO with $\text{GdH}_2$ shield

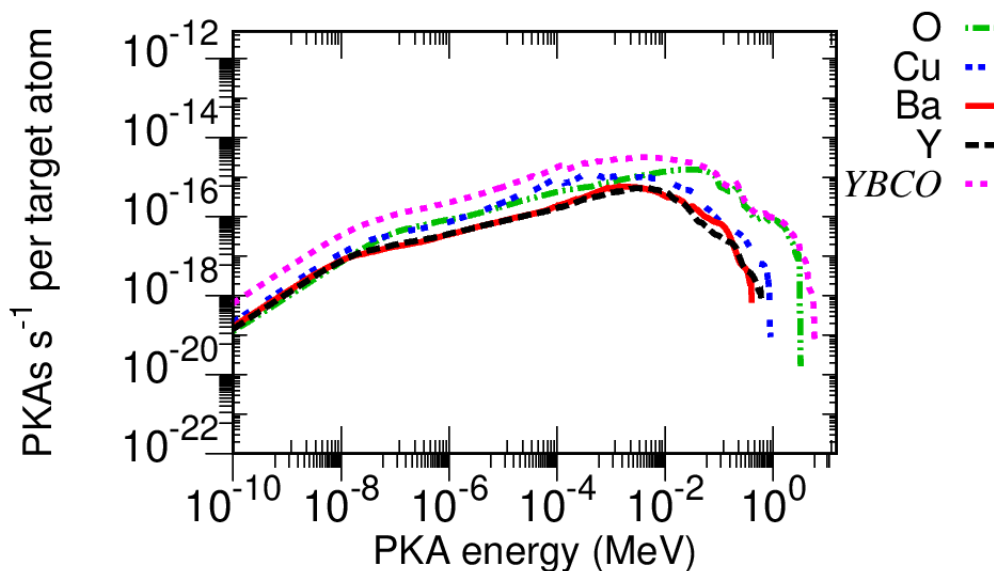


Figure 83: PKA spectra on the most critical HTS region with 51 cm shield

## PKA spectrum on YBCO with $B_4C$ shield

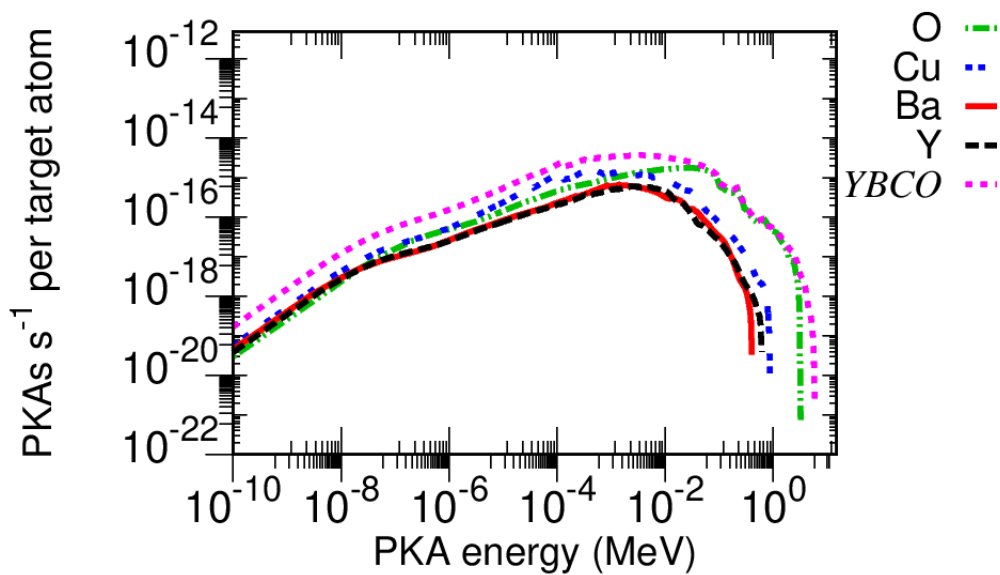


Figure 84: PKA spectra on the most critical HTS region with 51 cm shield

### PKA spectrum on YBCO with void shield

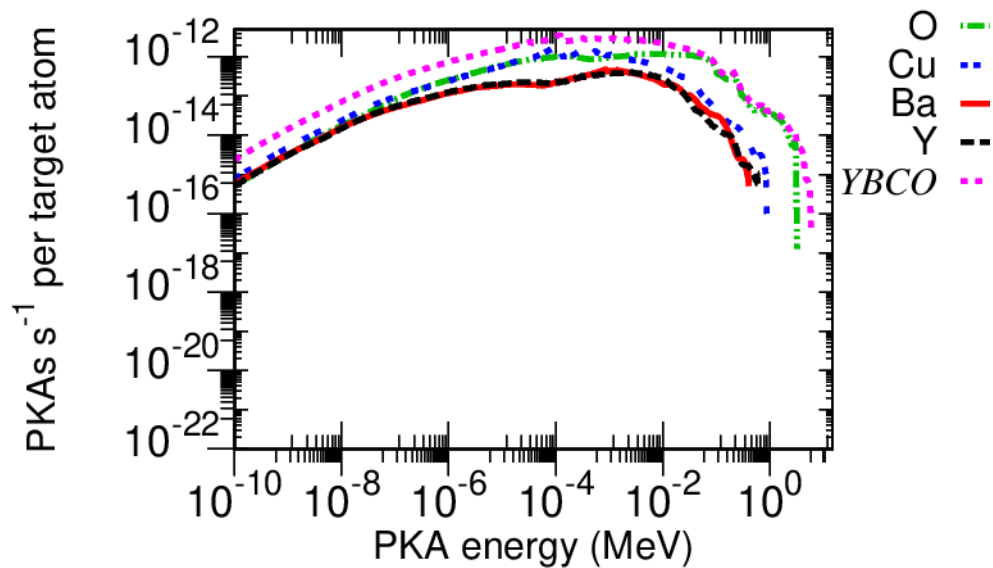


Figure 85: PKA spectra on the most critical HTS region

### PKA spectrum on YBCO with ZrH<sub>2</sub> shield

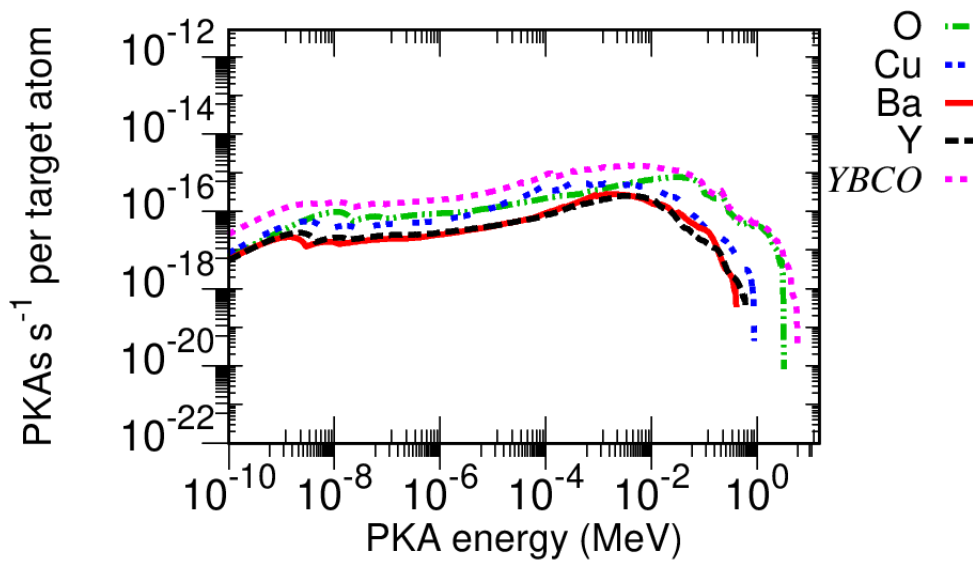


Figure 86: PKA spectra on the most critical HTS region with 51 cm shield

## PKA spectrum on YBCO with $\text{TiH}_2$ shield

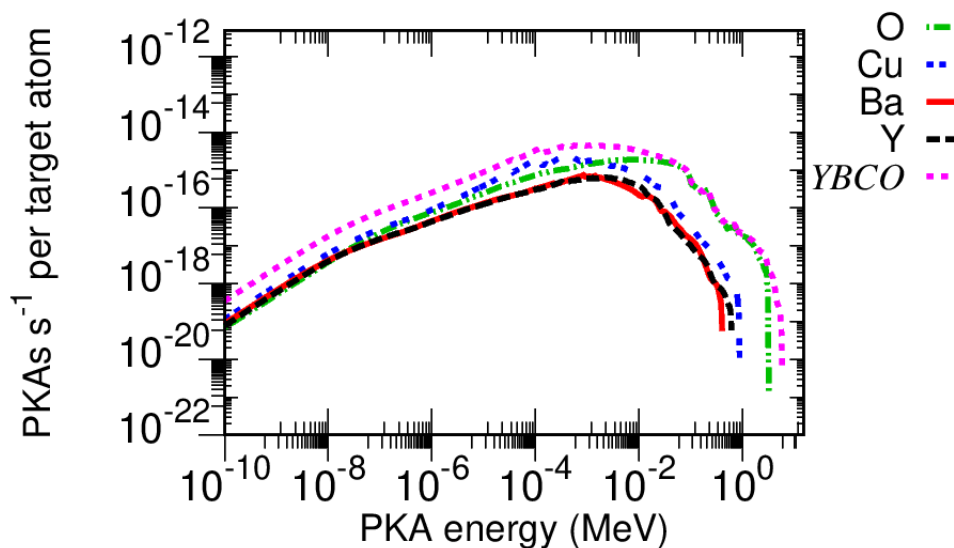


Figure 87: PKA spectra on the most critical HTS region with 51 cm shield

## PKA spectrum on YBCO with WB shield

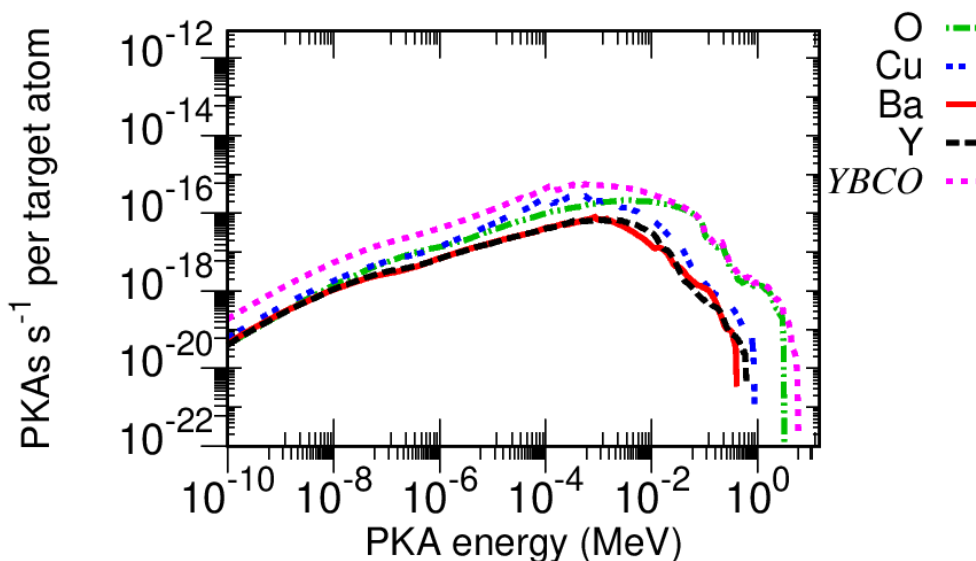


Figure 88: PKA spectra on the most critical HTS region with 51 cm shield

## PKA spectrum on YBCO with WC shield

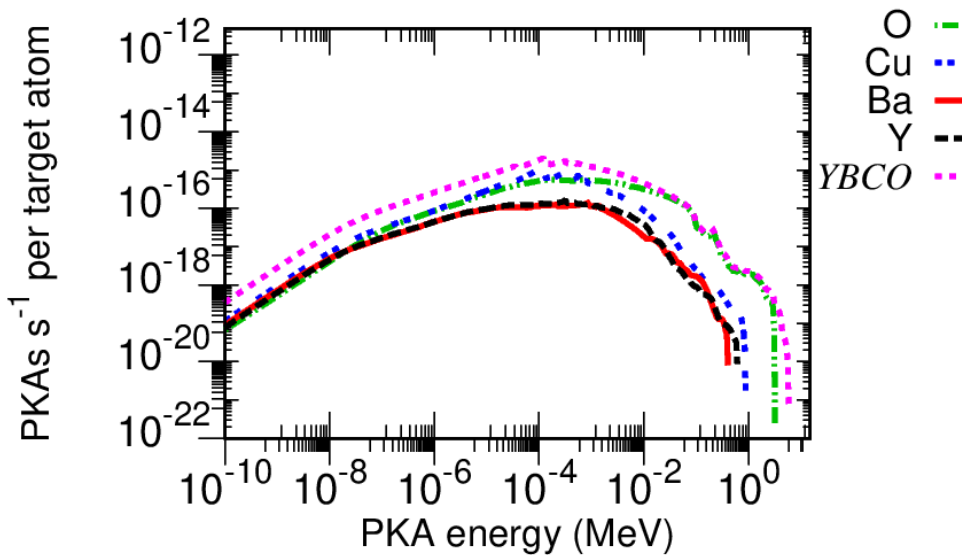


Figure 89: PKA spectra on the most critical HTS region with 51 cm shield

## PKA spectrum on YBCO with WB<sub>4</sub> shield

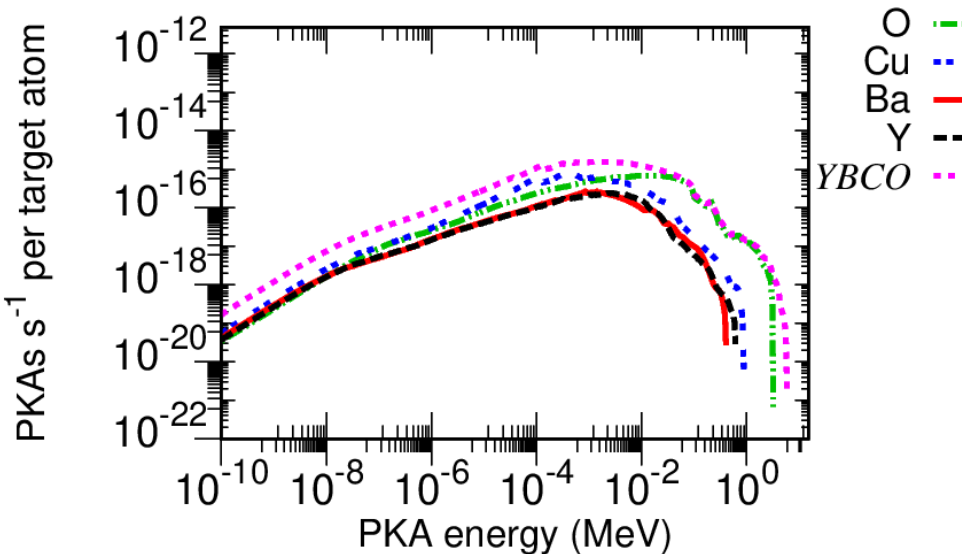


Figure 90: PKA spectra on the most critical HTS region with 51 cm shield

## PKA spectrum on YBCO with $\text{HfH}_2$ shield

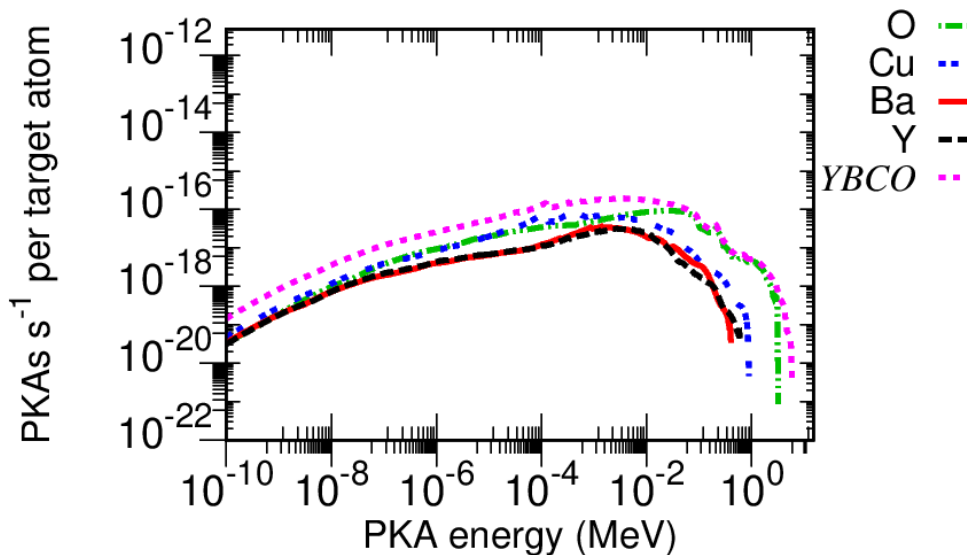


Figure 91: PKA spectra on the most critical HTS region with 51 cm shield

## PKA spectrum on YBCO with $\text{HfV}_2$ shield

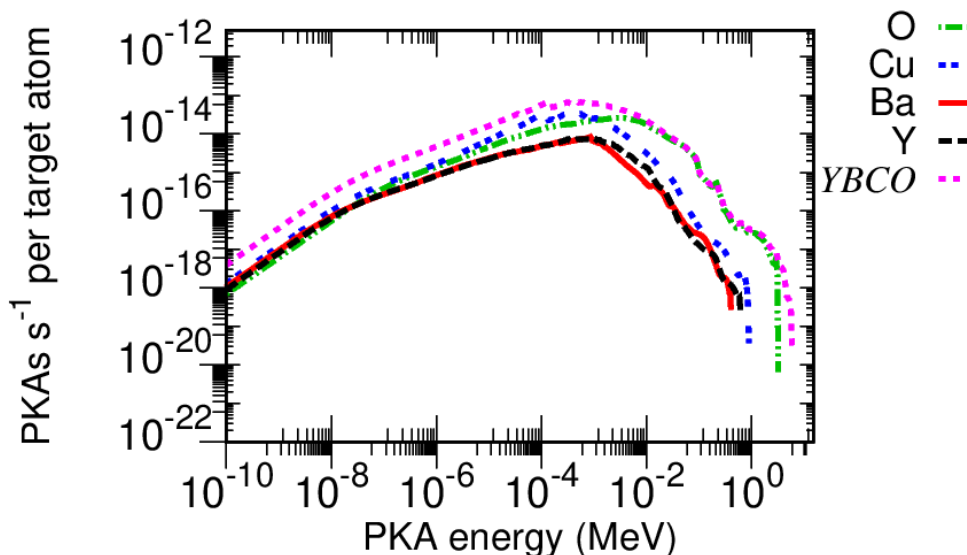


Figure 92: PKA spectra on the most critical HTS region with 51 cm shield

## PKA spectrum on YBCO with SS316L shield

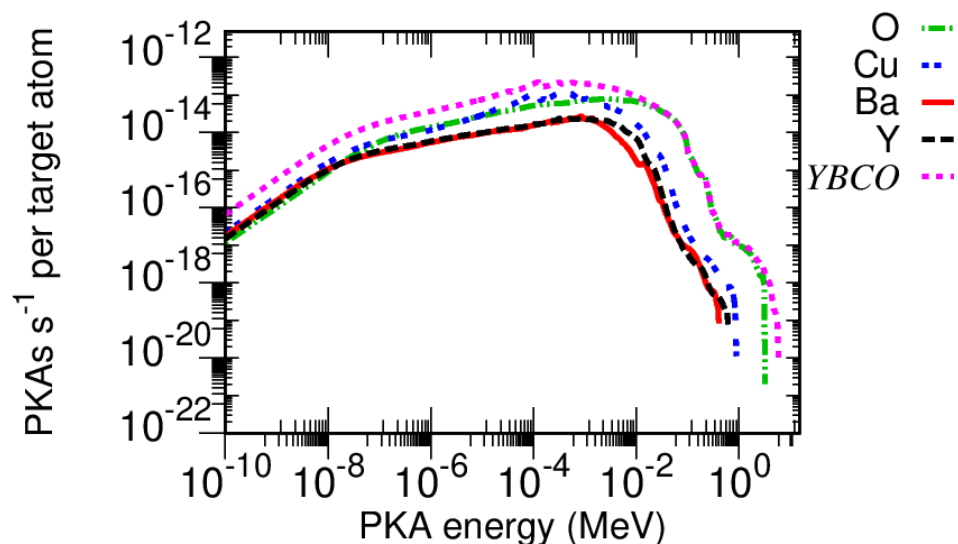


Figure 93: PKA spectra on the most critical HTS region with 51 cm shield

## PKA spectrum on YBCO with VB shield

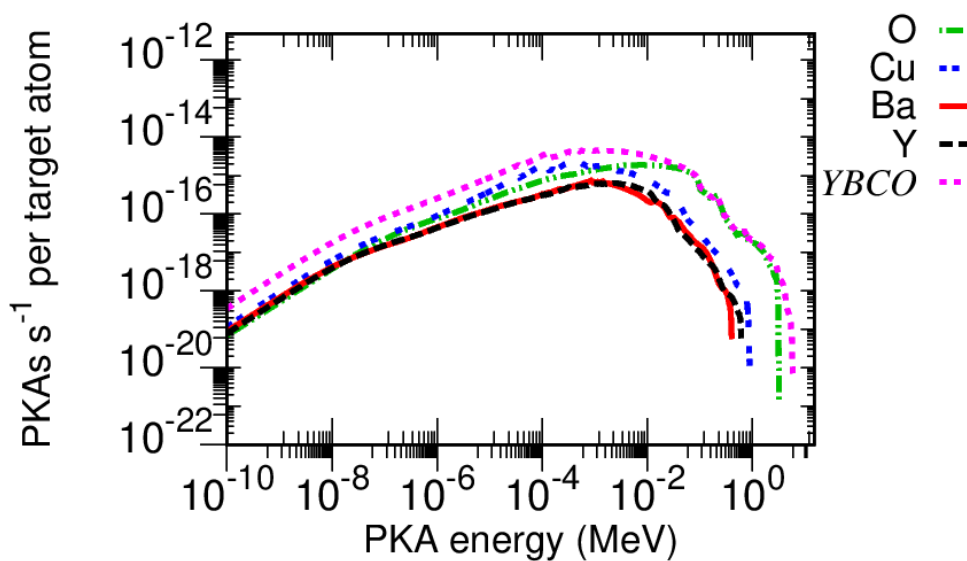


Figure 94: PKA spectra on the most critical HTS region with 51 cm shield

## PKA spectrum on YBCO with $\text{GdH}_3$ shield

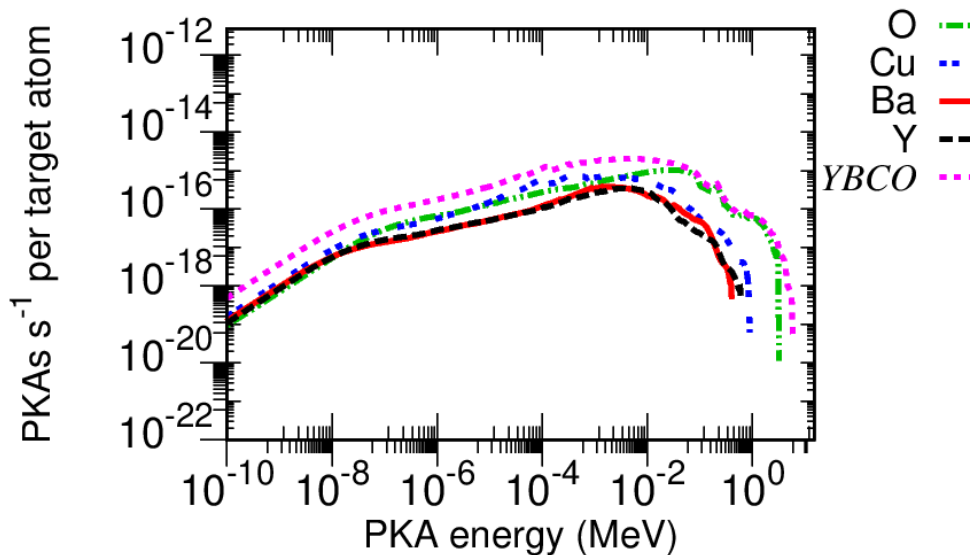


Figure 95: PKA spectra on the most critical HTS region with 51 cm shield

## PKA spectrum on YBCO with $\text{GdH}_2$ shield

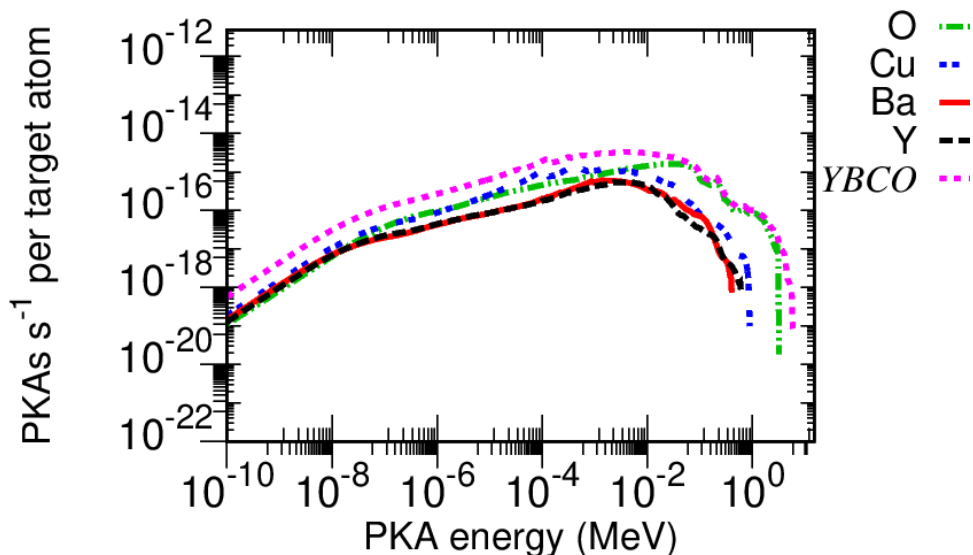


Figure 96: PKA spectra on the most critical HTS region with 51 cm shield

## PKA spectrum on YBCO with $B_4C$ shield

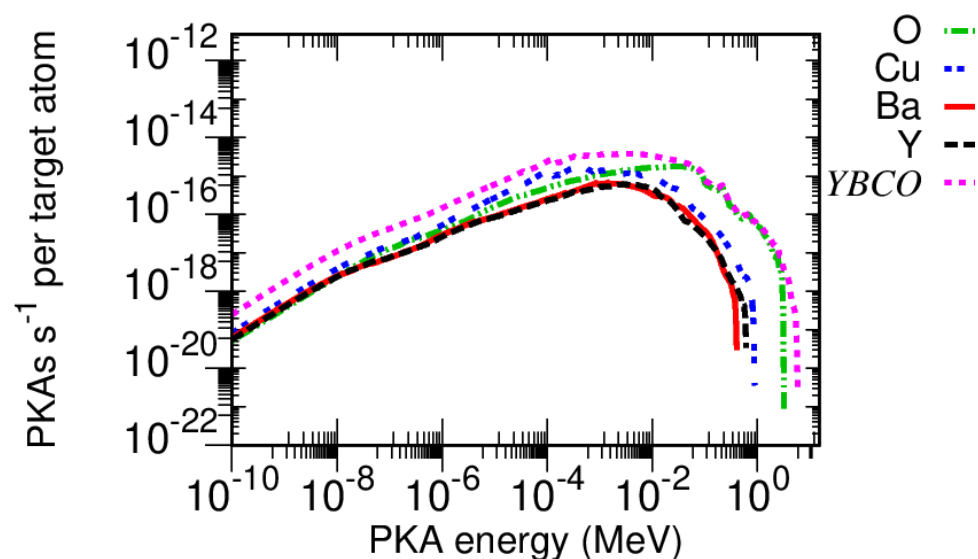


Figure 97: PKA spectra on the most critical HTS region with 51 cm shield